Department of Precision and Microsystems Engineering

Direct or Indirect? Unraveling the bandgap nature of metal halide perovskites

M.M. Ackermans

Report no : MNE 2020.029
Coach : Dr. B. Ehrler, Dr. E.M. Hutter, Prof.Dr. U. Staufer
Professor : Prof.dr. U. Staufer
Specialisation : Micro & Nano Engineering
Type of report : MSc Thesis
Date : 28 August 2020

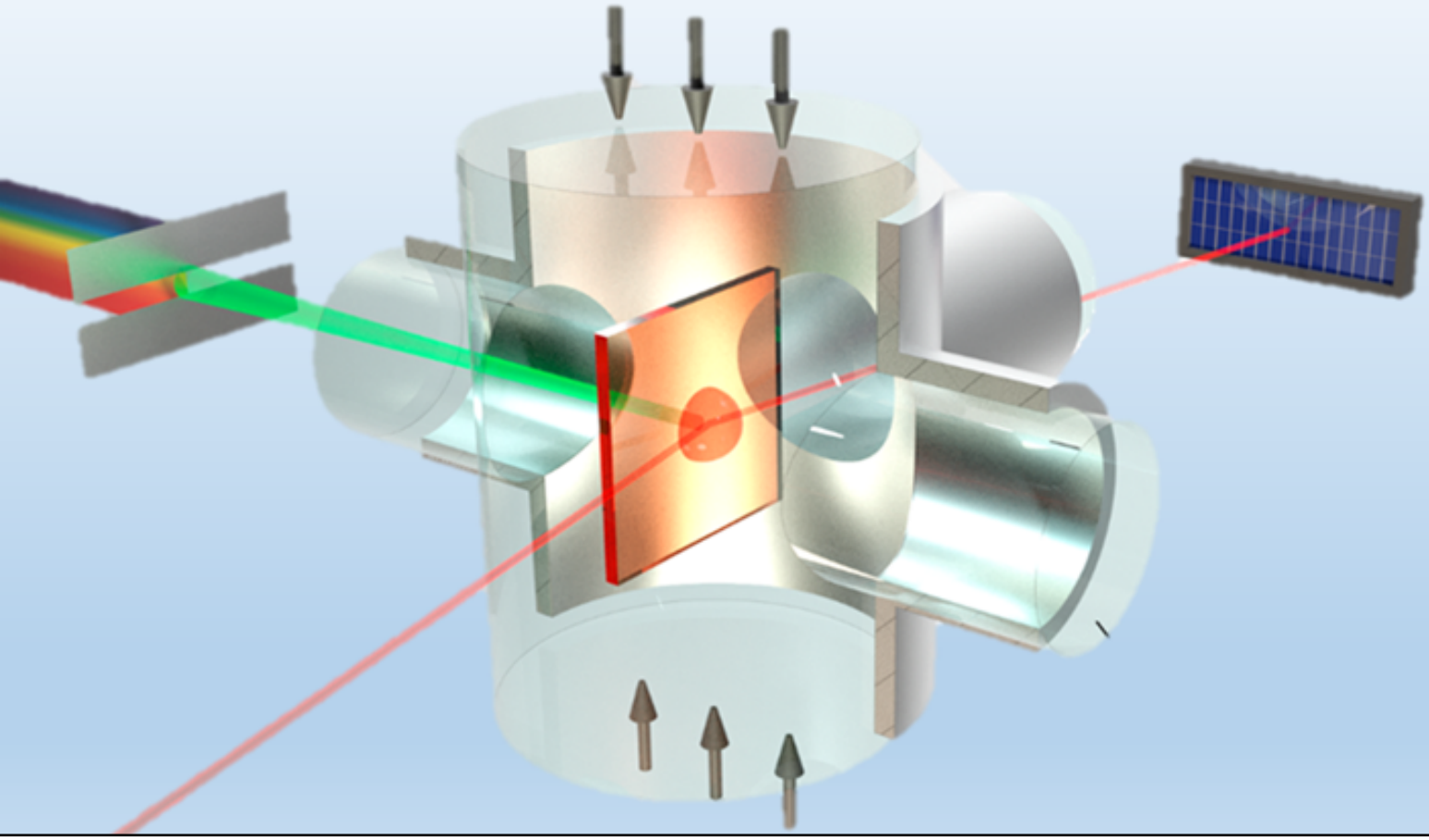

Direct or Indirect?

Unraveling the bandgap nature of metal halide perovskites

by

M.M. Ackermans

to obtain the degree of Master of Science
at the Delft University of Technology,
to be defended publicly on Friday August 28, 2020 at 11:00 AM.

Student number:	4239490	
Project duration:	September 1, 2019 – July 31, 2020	
Thesis committee:	Prof. dr. U. Staufer,	TU Delft, Mentor
	Prof. dr. P.G. Steeneken,	TU Delft
	Dr. ir. T.J. Savenije,	TU Delft
	Dr. B. Ehrler,	AMOLF, Supervisor
	Dr. E.M. Hutter,	AMOLF, Supervisor

This thesis is confidential and cannot be made public until August 31, 2021.

An electronic version of this thesis is available at `http://repository.tudelft.nl/`.

TU Delft

Preface

The thesis that lies before you is the outcome of a year's work. Although I aimed to accurately describe my scientific journey at AMOLF, including all ups and downs, there are probably parts of the project that are underexposed in this thesis. It is inherent to exploring new fields that you get stuck once in a while, without knowing what the next step should be. Nevertheless, I never regretted the adventure that I started in september 2019 at AMOLF. The activities and research I conducted are the perfect hybridisation of my fascination for our world at the nanoscale and interest in the advancement of new and sustainable technologies.

There are a few people who I would like to thank. First of all, my supervisors Bruno and Eline, for giving me the project and the opportunity to work at AMOLF, for helping me with the design, for their knowledge and critical input, tips for thesis writing and regular weekly meetings. Also, I thank my supervising professor Urs for managing the scope of the project and helping me to focus on the bigger picture. Furthermore, I show my gratitude to Marc, who helped from the start of the project with building the setup in the lab from scratch, making several components at the workshop, and showing me how the handle the pressure cell and pump. My group members Benjamin and Loreta deserve a special thank you, for giving me useful input on my setup, helping me in the the lab and making the $MAPbI_3$ samples that were used for this thesis. Also, I thank the other members of the Hybrid Solar Cells group, Christian, Emil, Lucie, Gianluca, Isabel, Moritz, Silvia, Imme, for always being open for discussions and questions, but above all, for the way too long coffee breaks, interesting talks and for giving me motivation to come to AMOLF every day, even when my setup did not work as desired. In my personal life, there are a few people who have supported me throughout the year. I would like to thank my parents Mike and Carola for always welcoming me when I needed a place to work, especially when Covid-19 limited everyone's office time, and even on their holidays. Last but not least, I thank my roommate Max, who has always showed interest in my work, gave me support when I needed it and made me the best dinners after a long day in the lab.

To the reader, I can only hope that reading this thesis sparks the same interest as I had when I started looking into perovskites exactly one year ago. Perovskite was a word I had never heard of before I started at AMOLF, but once I did, the internet seemed to be overflowing with publications on the amazing opportunities of perovskites.

M.M. Ackermans
Amsterdam, August 2020

Contents

List of Figures

List of Tables

1

Introduction

"The world is not on track to meet the energy-related components of the Sustainable Development Goals (SDGs)", the International Energy Agency (IEA) stated in their last report 'World Energy Outlook 2019' [1]. According to stated policies, global energy demand rises by 1% per year to 2040, while greenhouse gas (GHG) emissions should be decreased to stay below a temperature increase of 2^{o}C above pre-industrial levels, compliant with the Paris Climate Agreement of 2015. Countries are therefore urged to replace conventional energy generation methods with renewable sources, such as wind and solar power. These technologies have the potential to supply electricity against very low or zero GHG emissions. As predicted in multiple reports [2, 3], the capacity additions of power generation in the next 20 years will be dominated by solar photovoltaic cells (solar PV). However, the question remains if PV technology can be efficient, cost-effective, and reliable enough to meet these expectations.

The adoption rate of solar cell technology is heavily dependent on the costs of the power that it generates. Current levelized cost of energy (LCOE) estimations of PV systems are already below LCOEs for conventional sources. Where photovoltaic systems on a utility scale can produce energy at $32/MWh, the fossil source with the lowest LCOE is a gas combined cycle, which can, in an optimistic scenario, deliver at $38/MWh [4, 5]. Besides cost, there are other aspects of solar energy that play an important role when the application of PV cells is being considered, such as the mismatch between supply and demand of energy and seasonal dependence of solar irradiance[2]. Cost competitiveness is influenced by the climate of a region, but a lower overall cost of generated electricity could improve the business case of solar panels enough that it outperforms conventional sources in almost every country [4].

There are multiple ways to decrease the costs of PV energy. A breakdown analysis of the costs of energy would show the most important factors that contribute to the price. This can reveal what individual components of

a photovoltaic setup should be targeted to decrease the price, which could be the raw material costs, installation costs, price of the inverters, permits and so on. Analyses (e.g. by NREL [6]) over the last decade show that the overall price decrease of PV systems is starting to saturate, and that the price reduction options are limited. A still effective approach, however, is to improve at the efficiency of the the panels. A higher efficiency will lead to the same panel producing more energy over its lifetime. This lowers the overall costs per kWh without having to reduce the price of every single component. Looking for innovations to improve the efficiency of solar cells is therefore a popular topic in the current academic society.

Looking purely at the efficiency of solar cells, it can be concluded that photovoltaic technologies are on the rise [7]. Commercial photovoltaics nowadays are primarily made of crystalline silicon as the functioning material. Silicon is earth abundant, widely used in the semiconductor industry and its properties are relatively fit for photovoltaic applications. Silicon solar panels can reach efficiencies of up to 23% [8]. While more efficient cells are already developed in lab environments, there is a clear limit to what efficiency solar cells can reach. In 1961, Shockley and Queisser [9] calculated that single junction cells can reach an efficiency of about 33% (SQ-limit).

Researchers are developing multiple technologies that are slowly approaching the Shockley-Queisser limit. Different materials with photovoltaic properties are examined which gradually enhance efficiencies. Moreover, other designs allow a more complete collection of the full solar spectrum, in such a way that the SQ-limit can be surpassed. By placing two layers (tandem) with different bandgaps on top of each other, the efficiency limit is increased to 42%, three layers results in 49% and adding up layers would lead to a theoretical limit of 69% [10]. The working mechanism of photovoltaics and the importance of the bandgap is more thoroughly discussed in **chapter 2**. Efficient multi-junction solar cells have already proven to be successful, but usually require expensive materials and production processes, making them less attractive for commercial applications[11].

As can be seen in figure 1.1, the efficiency of top performing solar cell technologies have been increasing for decades. Emerging photovoltaic technologies have come up in the last 10 years that are already competing with conventional silicon solar cells. Where the rise of crystalline silicon cells has stagnated, perovskite solar cells (PSC) show an interesting development since the first perovskite cell was made in 2009. Since then, the efficiency of perovskite cells has risen from 3.8% to more than 25% in 2019 [12]. Configurations with purely perovskites in single-junction cells, as well as tandem arrangements with other perovskites or silicon layers are among the possibilities. It is one of the reasons why perovskites are frequently referred to as "the future of solar cells" [13].

However, the prospects of perovskite solar cells also have a less sunny side. Although the production process can be cheap, there are other properties that currently prevent PSCs from entering the commercial market [14]. One of the main issues with current cells is the instability that causes a quick loss of energy generation capacity, and may in some cases lead to a useless device in just a matter of days. Harsh environmental weather conditions can cause the cells to degrade, but the problem may even lie in the intrinsic (in)stability of the crystal structure. The structural properties of perovskites are further explained in section 2.1.1.

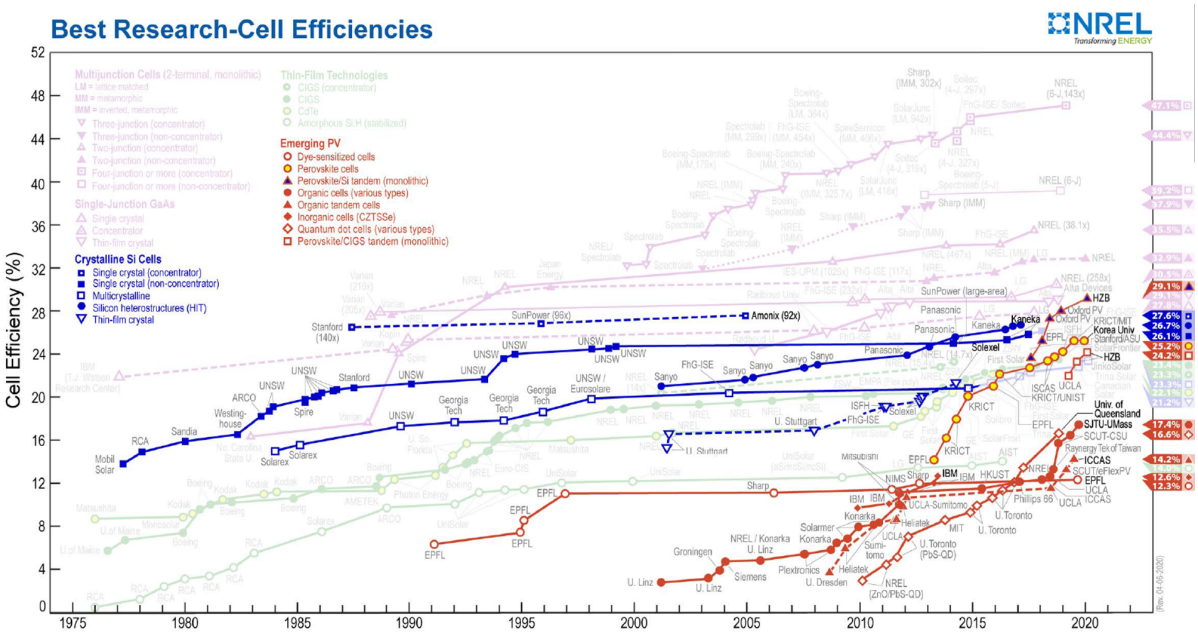

Figure 1.1: The yearly development of best-research photovoltaic cell efficiencies. Crystalline single-junction silicon cells are shown in blue. The rapid efficiency increase of emerging technologies is shown in red, lead by perovskite single junction and tandem cells since 2013. Reproduced from [7]

The number of studies into perovskites has increased exponentially over the last decade, but there are still unsolved questions. As reported in my literature review [15], there is an ongoing discussion on the either direct or indirect bandgap of methylammonium lead halide perovskite. The difference between these two characteristics is explained in section 2.2.3. Indirect and direct bandgap semiconductors have different properties that are useful in specific applications. Besides photovoltaics, perovskites are also promising in light emitting applications. They can be used for making lasers and LEDs with a wide range of colors, for which a direct bandgap is favourable. Although a direct bandgap is considered to be positive for PV systems as well, the indirect bandgap nature of PSCs is occasionally related to some of the excellent photovoltaic properties of the material, because it can be beneficial for charge extraction [16, 17]. Understanding the direct-indirect nature of perovskites is therefore crucial for designing optical applications with this material [18]. This thesis aims to contribute to the direct-indirect discussion by showing new experimental evidence on the matter. The particular perovskite used is methylammonium lead iodide ($MAPbI_3$).

For the collection of the data, an unprecedented setup was designed, build and used for measurements. The technique of the setup is based on Photothermal Deflection Spectroscopy (PDS), which can measure the optical absorption of a material with a very high sensitivity. The technique was originally described by Jackson et al.[19] in 1981. For this research, the design has been altered in such a way that the samples that are measured can be placed under a hydraulic pressure of up to 400 MPa. The design choices and explanation of the individual elements in the setup are discussed in **chapter 3**.

Furthermore, the methods used to carry out experiments, gather and analyse data are explained in the Experimental Methods **chapter 4**. What follows is a paper on the experiments and new data that was found using the PDS setup in **chapter 5**. A full overview of the results is presented in **chapter 6**, where the perfor-

mance of the build setup is shown along with the new data that is produced with the setup. This thesis ends with a conclusion in **chapter 7** and a discussion on the gained results, as well as a reflection on the project in **chapter8**.

Hopefully, the presented results in this thesis can help other researchers in their pursuit of finding the right perovskite for solar cells and other optical applications. It is evident that there are still years of research necessary to find the solutions that will boost the next generation of photovoltaics. It may be unclear if perovskites are going to be part of the next wave, but its interesting properties are indisputably very promising. Predicting what the world's future energy landscape will look like may be nearly impossible. Solar PV will certainly play an important role. What specific technology and material will come out on top is unsure, but it can be safely assumed that many applications of metal halide perovskites are yet to come.

2

Background

This chapter covers a background description on the bandgap effect that is examined in this work. The principles of solid-state physics are discussed that explain how a photovoltaic cell works. Spin-orbit coupling and the Rashba effect are also covered, which are important to understand the direct-indirect nature of the bandgap of $MAPbI_3$. Currently, there is an ongoing debate in the academic society on the direct-indirect bandgap of $MAPbI_3$. This debate is shortly summarized by reporting two contradicting examples of publications on the topic in section 2.7. Also, it is explained how applying pressure on $MAPbI_3$ can help in finding new evidence that can contribute to the debate, leading to the research question of this work. A more extensive covering of the academic discussion is done in the author's literature review[15], that preceded this thesis. Section 2.1 & 2.2, which explain the physical principles that are important to understand what the difference between a direct and an indirect bandgap is, are a direct adaption from the literature review which was part of the project[15].

2.1. Perovskite Solar cells

Since the commercialization of solar cells, crystalline silicon has been the predominant material used as semiconductor for the production for solar cells [20]. Silicon is an earth-abundant element which is widely used in the semiconductor industry, and currently the most cost-efficient technology for solar cells. However, new materials have been emerging, of which metal halide perovskites have shown very promising development over the past 10 years. Some of the merits of perovskite solar cells (PSCs) are a strong optical absorption, good charge-carrier mobilities, a tunable bandgap, and the possibility to process the cell from a solution [21]. These benefits result in a wide variety of manufacturing options for the production of perovskite solar cells[22]. Since the field of perovskite solar cells is relatively young, there is still a lot unknown about the

physics of these types of cells. Currently, one of the major problems with perovskites is the instability of the material under the exposure of light [23]. Another debate is the exact shape of the electronic band structure of metal-halide perovskite, which is discussed in section 2.7.

2.1.1. Crystal structure

Perovskite is not the name of the molecule that is used in the discussed solar cells, but of the crystal structure that certain materials have. Perovskite is described as a crystal with an ABX_3 structure, where A and B are cations, and X is an anion. The most commonly-used perovskite in solar cells is methylammonium (MA, CH_3NH_3) lead trihalide, where iodide, bromide, chloride (or a combination) could be the halide. Based on the particular halide, this material is generally referred to as $MAPbI_3$ for iodide or $MAPbBr_3$ for bromide. Because of the combination of organic and inorganic compounds in the structure, these are sometimes grouped as hybrid organic-inorganic perovskites. Some other options for the cations are formamidinium (FA, H_2NCHNH_2) or caesium on the A-site and tin (Sn) on the B site. An example of a methylammonium lead trihalide crystal structure is given in figure 2.1a.

The benefit of choosing the halide is that the optical bandgap can be tuned in order to achieve optimal efficiency. This makes perovskite solar cells also very interesting for tandem photovoltaics, where multiple materials are sensitive for a different wavelength in the sunlight spectrum. In light emitting applications (such as LEDs), this would mean that the color of the emitted light can be chosen based on the bandgap.

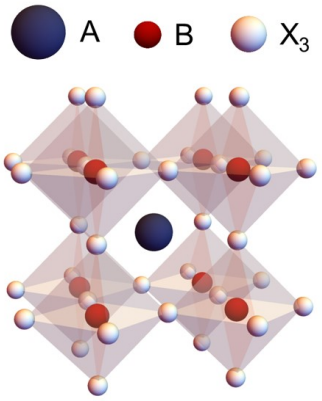

(a)

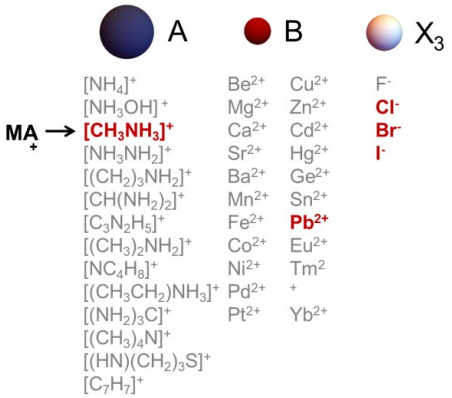

(b)

Figure 2.1: The structure of a $CH_3NH_3PbX_3$. The methylammonium cation in the middle is surrounded by corner-sharing PbX_6 octahedra [24] in figure (a). Figure (b) shows a list of possible organic-inorganic combinations to make a perovskite. This list excludes the A-site to organic ions. Without this exclusion, the number of possible combinations would be far greater, possibly exceeding 90,000 [25]. Methylammonium lead halides (bromide, chloride, iodide) have gained enormous interest of the scientific community because of their high power conversion efficiencies in solar cells. Figure adapted from [26]

Perovskite solar cells can be manufactured with relatively simple methods, which make them interesting for commercial applications. Hybrid (organic-inorganic) perovskite solar cells have been created with several deposition techniques: spin-coating, inkjet printing, vapor deposition and more [27]. In a sensitized architecture, perovskite is coated on top of a layer of transparent TiO_2, which acts as an electron transport layer. In a thin-film architecture, the perovskite is both the light-absorber and charge-conductor. Perovskite is sand-

wiched between p-type and n-type material to connect to the contacts [28]. When light is absorbed, charges are generated in the perovskite material, after which the free electrons and holes can travel to the anode and cathode contacts to generate a photocurrent [29].

The crystal structure of certain perovskites is still a highly debated topic. It is generally known that $MAPbI_3$ is made out of corner-sharing octahedra that enclose a MA-ion. The dimensions of the octahedra and the distance between MA-ions define more exactly what crystal system it belongs to. Furthermore, $MAPbI_3$ can occupy different phases, depending on the temperature or pressure [30, 31]. The three phases and corresponding crystal structures are cubic, tetragonal and orthorhombic. Under ambient conditions, $MAPbI_3$ is typically described as tetragonal. When its temperature is increased to 333 K, it undergoes a phase change into a cubic system. Below 165 K, the phase changes from tetragonal to orthorhombic.

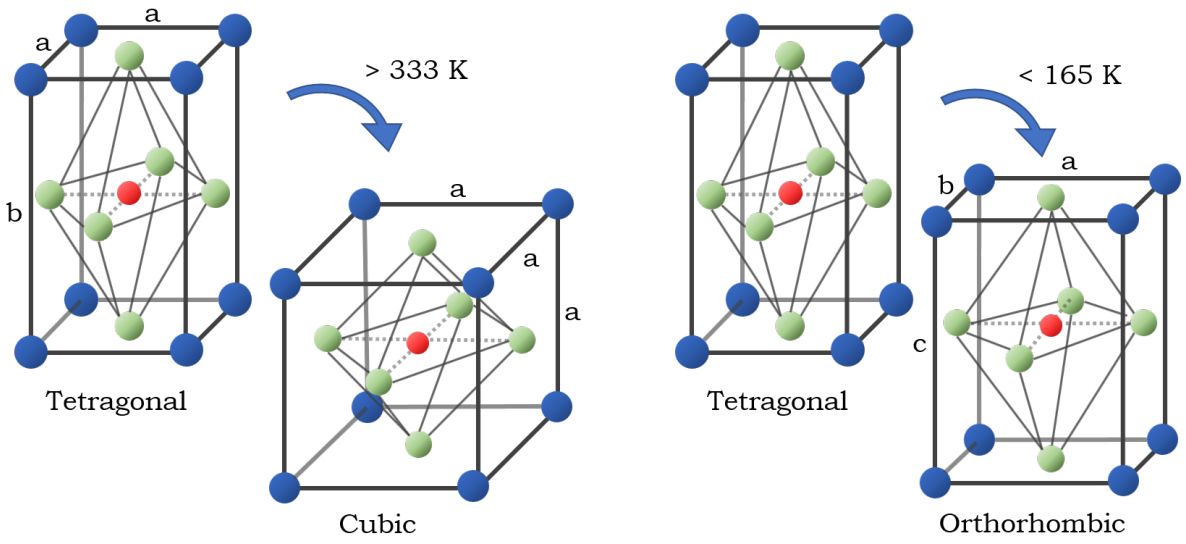

Figure 2.2: schematic overview of the tetragonal, cubic and the orthorhombic structure, including the relative dimensions. $MAPbI_3$ is assumed to have a phase change at 333 K and 165 K from tetragonal to cubic and orthorhombic respectively. In this figure, the blue dots represent MA-ions, the red dots represent lead ions and green dots the iodide ions.

The disagreement on the crystal structure lies in the space group of the tetragonal phase. As can be seen in table 2.1, there are different space groups reported in literature for the the tetragonal phase of $MAPbI_3$ (and $MAPbBr_3$). The consequence of this discussion is a lack of consensus on the inversion symmetry of the crystal structure. The tetragonal phase of $MAPbI_3$ is centrosymmetric for the *I4/mcm* space group, but non-centrosymmetric for the other reported groups. As will be explained in section 2.2.5, inversion symmetry is a necessary property for Rashba-splitting to occur. Since Rashba-splitting can lead to an indirect bandgap, tetragonal *I4/mcm* in $MAPbI_3$ can result in a direct gap, while tetragonal *I4cm* results in an indirect bandgap. Both terms (direct and indirect bandgap) will also be explained in the next section.

Table 2.1: Space groups of methylammonium lead halide perovskites

Material	Temperature (K)	Crystal system	Space group	Centrosymmetric	Reference
$MAPbCL_3$	> 179	Cubic	$Pm\bar{3}m$	yes	[32, 33]
	173 - 179	Tetragonal	*P4/mmm*	yes	[32, 33]
	< 173	Orthorhombic	$P222_1$	no	[32, 33]
$MAPbBr_3$	> 240	Cubic	$Pm\bar{3}m$	yes	[34]
	155 - 240	Tetragonal	*I4/mcm*	yes	[35]
	150 - 155	Tetragonal	*P4/mmm*	yes	[35]
	< 145	Orthorhombic	$Pna2_1$	no	[34]
$MAPbI_3$	> 333	Cubic	$Pm\bar{3}m$	yes	[30, 36]
		Tetragonal	$P4mm$	no	[37]
	165 - 333	Tetragonal	*I4/mcm*	yes	[30, 38]
		Tetragonal	*I4cm*	no	[38]
	< 165	Orthorhombic	$Pnma$	yes	[30, 36]

2.2. Principles of Semiconductors

In order to understand the photovoltaic properties of perovskites (and other semiconductors), the physical principles of semiconductors will be explained in this section. Firstly, the electronic band structure is covered. The crystal lattice, explained in the previous section, is important for understanding the formation of the band structure of a material. The electronic bands are a direct result of the atomic bonds and the crystal lattice and define the classification of semiconductors: The width of the later-discussed bandgap determines whether a material is an insulator, conductor or semiconductor. The modification of a semiconductor can be used to make components such as a pn-junction. This introduces the working principle of solar cells. To understand the effect that is investigated in this thesis, spin-orbit coupling, the Rashba effect, the direct/indirect bandgap and the Urbach tail are briefly covered.

2.2.1. Bandgap

When atoms are bound together, they may form a stable crystal structure by arrangement of the atoms resulting in the lowest overall potential energy. An electron orbiting a single, isolated nucleus would only have discrete energy levels. When atoms are brought close together, the orbitals will overlap and change the energy levels. According to Pauli's exclusion principle, no two electrons in one orbital can have the same energy and spin, and therefore the electrons will occupy different energy states [39].

In a crystal lattice with a large number of atoms, the exclusion principle will result in many different energy levels, which are spaced so close to each other that they can be considered a continuum. This is called an energy band. The highest range of energy levels in which electrons are normally present is called the valence band. The lowest range of vacant energy levels is called the conduction band. These bands do not necessarily overlap. This means that a gap between the energy bands can exists, where no occupation of this energy

level is possible. This is called the bandgap. When the bands do overlap or when a band is not completely filled, electrons can readily jump to higher, vacant energy levels, which makes them essentially "free" in the lattice. This is what defines a conductor. In insulators and semiconductors, the bandgap between the occupied valence band and unoccupied conduction band prevents the electrons from moving to a higher energy level. Typically, the bandgap in a semiconductor is smaller than 5 eV. With a wider bandgap, the material is considered an insulator.

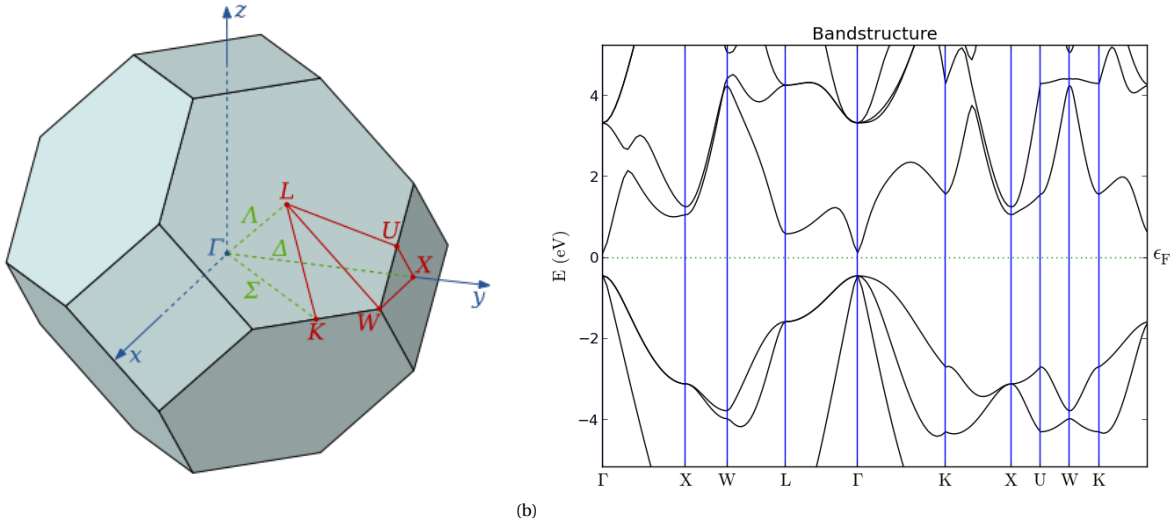

(a) (b)

Figure 2.3: A representation of a face-centered cubic lattice (a) and a band structure of the semiconductor gallium arsenide (GaAs), generated using DFT-software (QuantumATK)[40] (b). Energy level 0 is denoted as the Fermi level, which is the energy level in between the highest occupied and lowest unoccupied bandgap where the probability of finding an electron is exactly 1/2

In a 3-dimensional crystal structure of a solid, a reciprocal space can be defined, as seen in figure 2.3a. The set of all points in reciprocal space that are closer to the origin of the reciprocal lattice than to any other reciprocal lattice points, is called the first Brillouin zone [41]. Letters such as X, W and Γ denote special symmetry points. Because of the reciprocality, the behaviour of electrons within the crystal can be described using only this zone. It is generally done as a function of wave vectors (k-vectors), which denote the direction and momentum that electrons can have. From this, the possible energy levels can be calculated and plotted to form a band structure of a certain material. In figure 2.3b a typical band structure (of GaAs) is shown. The energy level of an electron is plotted on the y-axis versus the wave vector on the x-axis.

2.2.2. Photovoltaic effect

The photovoltaic effect is the underlying principle which solar cells exploit to convert light into electric current. In a semiconducting material which is at a ground state, the electrons fill up the the valence band and are bound to their orbitals. This means that they cannot freely move around in the material. When a photon is absorbed by the material, it may transfer its energy to an electron. When this energy is high enough (larger than the bandgap), it can excite the electron from the ground state to an excited state. The electron is now in the conduction band and is free to move. It leaves behind a hole in the valence band. In a later stage, excited electrons can recombine with holes and emit a photon in the process. Radiative recombination is effectively

the reverse process of radiative excitation.

Photovoltaic cells use the process of electron excitation by photons to move electrons and create an electric current. The key is to place the active material between a slightly positive and slightly negative layer to create a so-called pn-junction. In conventional silicon solar cells this is done by doping different layers of silicon with boron and phosphorus ions. The pn-junction creates a small internal potential difference. This potential drives the separated electrons and holes to the sides of the cell, where they are collected by a cathode and anode. Connecting a load between the anode and cathode then leads to an electric current.

The previously explained bandstructure and band transitions introduced the basics working principles of semiconductors. Different types of semiconductors have been extensively researched in the field of photovoltaics, but the working principles of all types are similar. As mentioned before, the most commonly used photovoltaic material is crystalline silicon. This report, however, will focus on metal halide perovskites as semiconducting material for solar cells. It has a more complicated atomic structure than silicon solar cells, which was explained in section 2.1.1. The next paragraphs will explain certain phenomena that influence the bandstructure of certain perovskites, specifically at the bandgap.

2.2.3. Direct & indirect transitions

The transitions of electrons between the valence band and the conduction band is what makes semiconductors applicable for photovoltaic purposes, as is previously described in this section. The transition between the band can happen in two directions: either excitation when an electron moves from the valence band to the conduction band, or recombination the other way around. While excitation can happen because a photon is absorbed, for recombination a photon may be emitted. This close relationship between electronic bands and optics makes it ideal to use light for exploring bandgap properties.

The transitions of electrons between the bands can have a direct or indirect nature [42]. Direct transitions happen when the valence band maximum (VBM) and conduction band minimum (CBM) are exactly aligned in momentum(k)-space. When an electron is excited or recombined, it does not change its momentum. However, when the transition is indirect, the electron needs to change its momentum to move between the VBM and CBM. This momentum change requires a phonon, which is a quasiparticle representing vibrational motion in which a lattice of atoms oscillates [43]. Higher temperature of a material would mean more elementary vibrations, and thus more phonons to assist indirect transitions. The difference between direct and indirect bandgaps is visualized in figure 2.4.

Generally, direct bandgap transitions are more probable to occur than indirect transitions, because a phonon is required to shift the momentum with indirect transitions. As a result, electrons in indirect bandgap materials stay longer in the excited state before they recombine. This can be a favourable effect in photovoltaics, because excited electrons are free to move, meaning that there is more time for charge-carrier transportation and the collection of energy for a designed purpose of a device, such as in a solar cell. However, excitation is also less probable to occur when a phonon is required for an indirect transition. Overall, a solar cell is most

efficient when all recombination events are radiative. In that case, re-emitted photons can be absorbed again and energy is preserved. Radiative recombination is more likely to occur in direct-bandgap semiconductors, and thus for efficient solar cells, a direct bandgap is always preferred [44, 45].

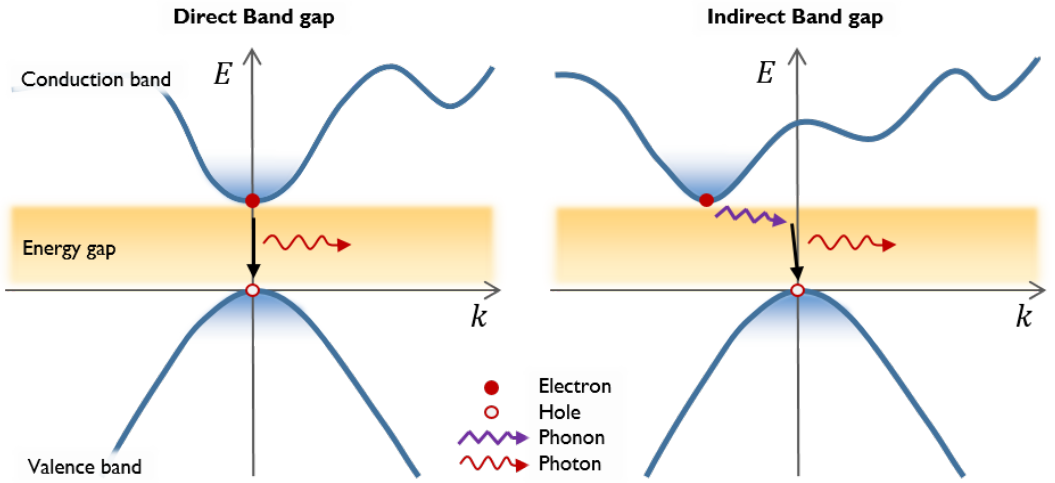

Figure 2.4: The difference between a direct (left) and indirect (right) bandgap during recombination events. In the latter case, a (thermal induced) phonon is required for the recombination to happen

2.2.4. Spin-orbit coupling

An important effect that should be discussed to better understand the formation of the bandgap of semiconductors is spin-orbit coupling. As the name suggests, there can be an influence of the intrinsic spin of an electron on the orbital path it follows around nuclei, which was first described by Dresselhaus in ref. [46] for Zinc-Blende structures. An electron is either in a spin-up or spin-down configuration (denoted by the spin quantum number) which describes its intrinsic form of angular momentum. This intrinsic spin can be coupled to the orbital angular momentum via spin-orbit coupling. This is a relativistic effect (inversely proportional to c^2, where c is speed of light) which scales with the atomic number squared of the atom the electron is orbiting [47, 48]. Consequently, the spin-orbit coupling is more significant in semi-conductors with heavy elements such as Pb. [41].

(a) (b)

Figure 2.5: Electron orbital within the frame of a proton (p) (a). The same situation as seen from the frame of an electron (e), where the proton has a (relative) motion with respect to the electron. **L** denotes the angular momentum of the electron orbiting the proton with speed **v**. **B** is the magnetic field acting on the electron as a result of the relative motion of the proton and the electron. Reproduced from [39]

Spin-orbit coupling can qualitatively be understood with the aid of figure 2.5. An electron is moving with speed **v** circularly around a proton, and the angular momentum **L** is pointing upwards. As seen from the reference frame of the electron, the proton is moving in a circle around the electron, creating a magnetic field **B**. As explained above, an electron has an intrinsic spin, resulting in a magnetic moment. The governing equation for the potential energy U of a magnetic moment inside a magnetic field is given by

$$U = -\boldsymbol{\mu} \cdot \mathbf{B} \tag{2.1}$$

with $\boldsymbol{\mu}$ being the intrinsic spin moment and **B** the magnetic field due to the electron's orbit. When the spin is parallel to the magnetic field **B** (and thus parallel to **L**), the combination of the magnetic moment of the electron and the magnetic field **B** results in a slightly different potential energy than when the spin is anti-parallel to the magnetic field. The potential energy contribution of the spin-orbit interaction is highest when **B** and $\boldsymbol{\mu}$ are anti-parallel, and lowest when they are parallel. The energy levels are visualised in figure 2.6.

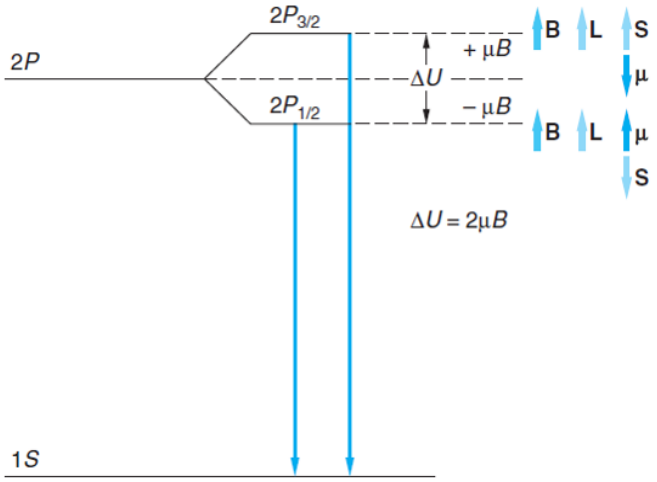

Figure 2.6: A visual representation of the energy effect of spin-orbit coupling. Due to the spin being aligned or anti-aligned ($+\boldsymbol{\mu}$ or $-\boldsymbol{\mu}$) with the magnetic field **B**, the total potential energy of the orbit can be slightly different (ΔU) [39]

2.2.5. Rashba effect

The combination of spin-orbit interaction and a certain atomic structure can have an interesting effect on the bandgap diagram of a material[49]. When the structure is centrosymmetric, i.e. for every point in the unit cell of a crystal lattice there is an indistinguishable point, there is symmetry in the potential and so it does not favour a direction of the electron's spin-moment. However, when there is asymmetry in the potential, a spin orientation can result in a different potential energy for the same momentum. This results in a splitting of the energy bands into spin aligned and a spin anti-aligned (sub)band. As a consequence, around the high symmetry point of the bandgap, two smaller bandgaps are formed which may be misaligned in k-space with respect to the valence band maximum.

A necessary condition for Rashba splitting to generate an indirect transition as the lowest-energy transition is

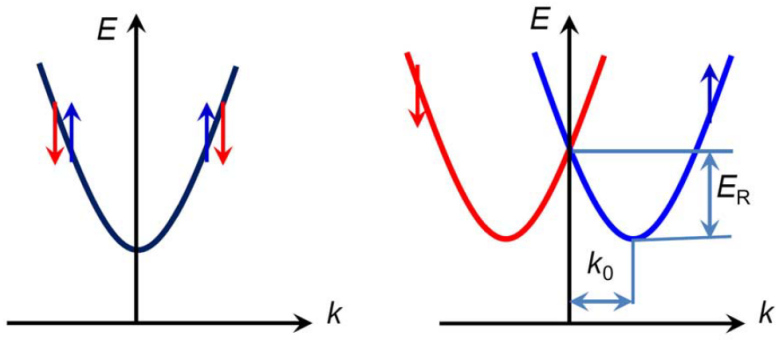

Figure 2.7: Rashba splitting of the conduction band. The conduction band minimum (CBM) is split into two different minima on both sides of the former minimum. The colors red and blue correspond to a spin down or spin up. k_0 denotes the shift in momentum space, E_R is the energy difference of the bandgap due to the splitting. Reproduced from [50]

that the valence band does not split with the same magnitude as the conduction band. Rashba splitting only happens when the atom that the electron is orbiting has a high mass resulting in large spin-orbit coupling. When the conduction band is formed around atoms that are heavier than those around which the valence band is formed, then the valence band does not split with the same magnitude and therefore the extrema (VBM and CBM) are shifted in k-space relative to each other. It has been reported that this is an occurring effect in metal halide perovskites [50–52]

The Rashba effect is known to be either a static or dynamic effect. In the static case, the crystal lattice itself lacks inversion symmetry resulting in a spin-dependent orbit. A dynamic Rashba effect may arise when the mobility of ions in the structure breaks inversion symmetry, even when the bulk structure is centrosymmetric. Fluctuating ions can therefore locally induce a dynamic Rashba effect. This is proposed as an explanation for a Rashba effect happening in metal halide perovskites even when there is inversion symmetry in the bulk structure [52, 53]

2.2.6. Urbach tail

In an ideal situation, there would be no possibility of excitation when a photon carries less energy than the bandgap of the material it encounters. However, in reality, a tail is observed in the absorption verses photon energy measurements, which indicates that there is some excitation happening at below-bandgap energy levels. This effect is called the Urbach tail. It can originate from disorder in the crystal lattice, which may be the result of doping, defects or lattice vibrations. [43]. An example of an Urbach tail (of GaAs) is given in figure 2.8a. The steepness of the tail can be described by the Urbach parameter or Urbach energy(E_0). The absorption is dependent on this parameter according to

$$\alpha(E) = \alpha_g \cdot exp(\frac{E - E_g}{E_0}) \tag{2.2}$$

which means a smaller Urbach energy leads to a larger exponential power and thus a steeper tail. In figure 2.8b, the effect of temperature on the Urbach Energy of GaAs is shown. When a semiconductor has a lower temperature, the Urbach tail becomes steeper. This does not influence the direct or indirect property of the

bandgap, but it does help to characterize the complete absorption spectrum below the bandgap. In a later stage (section 6.7), a parallel is drawn between the effect of temperature and pressure on the Urbach energy.

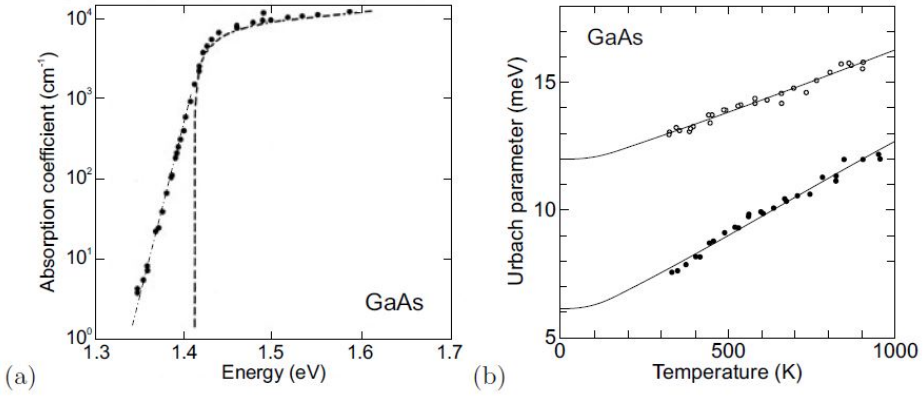

Figure 2.8: The Urbach tail for gallium arsenide is shown in (a). The dashed line represents the absorption spectrum for a direct transition, without an Urbach tail. Figure (b) shows the temperature dependence of the Urbach Energy(E_0) in two GaAs samples. Reproduced from [43].

2.3. Photothermal Deflection Spectroscopy

Photothermal Deflection Spectroscopy (PDS) is a technique developed in 1981 [19, 54] to measure the optical absorption of a material with very high sensitivity. It is based on the principle that incident light will locally heat a sample and its surroundings. The effect is similar to what is known as the "mirage effect". This optical phenomenon can be regularly observed on hot sunny days when driving on a long, straight road. When the tarmac is heated up by the sunlight, it may look as if the road is in a liquid state or as if a layer of water lies on top of it. The explanation of this effect lies in the fact that the heated air just above the asphalt has a different refractive index than colder air further away from the asphalt. Light that is traveling through the heated area will be slightly refracted because of the change in refractive index. The refracted light can be observed from a distance as a displaced image.

PDS uses the mirage effect to measure the temperature change at a surface, which is then related to the absorption of the light that heats the surface. An incident monochromatic light beam (pump beam), perpendicular to a sample surface, locally heats a sample. This creates a temperature distribution in the sample, but also in the medium surrounding the heated spot. The medium, generally an inert non-absorptive liquid (CCl_4 or FC-72), is chosen in such a way that a temperature change results in a large change of refractive index: a high $\delta n/\delta T$. A second beam (probe beam), is directed parallel to the sample surface through the heated area. The probe beam, usually a laser, will deflect with angle ϕ in the heated area because of the change in refractive index. The deflection is picked up by a position sensor after the sample. This process is repeated for a range of wavelengths to create a full spectrum. The principle is shown in figure 2.9a in 3D, and a side view in figure 2.9b. This version of PDS is called Transverse-PDS, because the pump and probe beam are perpendicular to each other.

in short, the process consists of the following principles:

1. A monochromatic pump beam hits a sample
2. The monochromatic light gets absorbed and heats the sample
3. The heat creates thermal gradient in the medium around the sample. This results in a refractive index gradient in the same area
4. A laser probe beam is directed perpendicular to the sample through the gradient area
5. The laser gets deflected because of the refractive index gradient

The amount of absorption is thus proportional to the angle of deflection. More absorption creates a larger temperature gradient, therefore a larger refractive index gradient and thus a larger deflection angle (ϕ).

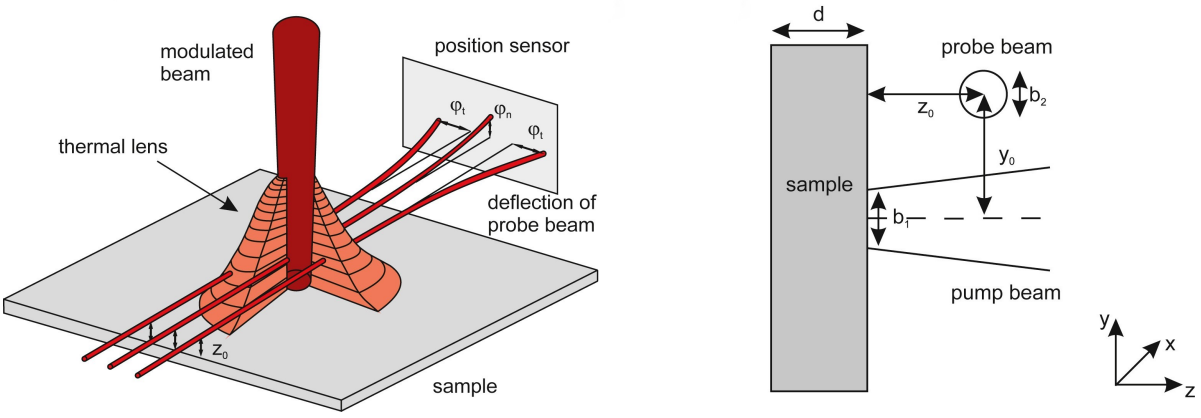

(a) (b)

Figure 2.9: The working principle of a PDS. A pump beam of monochromatic modulated light irradiates perpendicular to the surface (z-direction). By absorption, this creates a thermal gradient in the medium surrounding it. A probe beam is placed parallel to the surface (x-direction) and through the heated area. The temperature gradient leads to a refractive index gradient which bends the light. The deflection can then be related to the absorption. A 3D view is shown in (a), a side view of the yz-plane is shown in (b). Reproduced from [55]

To improve the signal-to-noise ratio of the measurements, the pump beam is modulated (mechanically by an optical chopper, or electronically) at a certain frequency. The effect is that the temperature distribution of the heated area, the so called thermal wave, is modulated with the same frequency. Consequently, the deflection of the probe beam alternates because of the periodic heating and cooling of the medium. When more light is absorbed, the temperature will increase faster during heating and cool down faster when the pump beam is blocked. The ideal amplitude of the alternating deflection is thus proportional to the absorption.

An important property of PDS is that the measurements provide only relative results. This means that the shape of an absorption spectrum can be calculated, but not the absolute value. To obtain the absolute values, an extra measurement using another method is necessary to scale the results of PDS. This is usually done with a UV/Vis transmission measurement. With this technique, it is possible to measure absolute absorption at wavelengths above the bandgap very well. However, below the bandgap UV/Vis is not very accurate. The result is a relatively high noise floor. Especially further below the bandgap, where the absorption is a few orders of magnitude lower than above the bandgap, UV/Vis measurements do not give accurate results. The

trick is to scale the PDS results to the UV/Vis data that is above bandgap. The above bandgap part will in that case overlap, the below bandgap part of the PDS data is scaled accordingly and provides highly sensitive and accurate data.

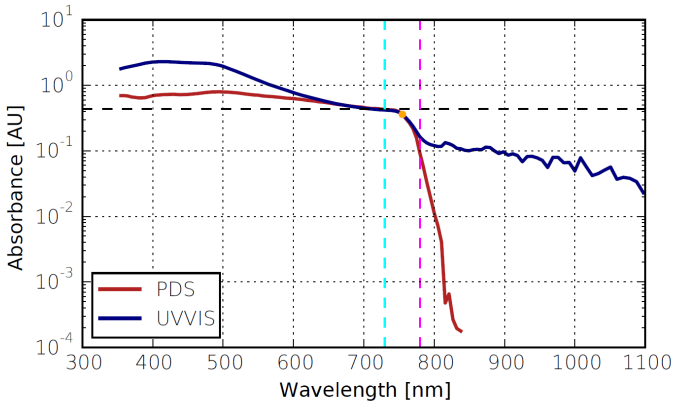

Figure 2.10: A PDS and UV/Vis measurement of the same sample by Becker-Koch for his master thesis at the university of Heidelberg. The colored dashed lines show the part where the PDS data is fitted onto the UV/Vis data. It can be clearly seen that the PDS measurement is multiple orders of magnitude more sensitive. Reproduced from [56]

When Jackson et al. published about PDS in 1981, they accompanied the description of the method with a series of sensitivity studies on different parameters in the setup. These parameters are important to take into account when designing a well-performing PDS device. A proper alignment of the two beams with each other and the sample is crucial, but also the size of the pump beam spot can greatly improve the signal. A smaller spot results in a more concentrated light beam, which leads to a higher temperature gradient. Other parameters are the distance z_0 between the sample and the probe beam, the modulation frequency f_{ref} of the pump beam, the sample width and the distance after the sample until the position sensor. In chapter 3 is explained how these parameters are incorporated in the design choices that are made.

2.4. Absorption, absorbance and absorptance

Having a clear definition of the quantity that is measured with PDS is crucial to avoid mistakes during analysis. UV/Vis and PDS are different techniques to quantify the same property of a material, but the quantities are not directly comparable. To prevent confusion, definitions of the terms and quantities are explained in this section. They are also related to the corresponding measurement methods.

2.4.1. Absorption

Optical absorption is the phenomenon of light that is being absorbed by a material. The term refers to the physical process of light being absorbed when it travels through a material. When a beam of light hits a surface, three effects can happen to the incident beam: absorption, reflection and transmission. Before relating the effects to material properties, it can be concluded that the reflected, transmitted and absorbed fractions

must add up to the incident light intensity (I_0), that is:

$$F_A + F_R + F_T = 1 \tag{2.3}$$

F_A is the absorbed fraction, F_R the reflected fraction and F_T the transmitted fraction of the incident light. There are multiple approaches to quantify absorption. Three examples are given below: absorptance, absorbance and absorption coefficient. These are important for analysing data from PDS and UV/Vis spectroscopy measurements.

2.4.2. Absorptance

The fractions as described in equation 2.3 can be defined as the ratio of the absorbed, reflected or transmitted power to the incident radiant power. The expressions used are in that case absorptance, transmittance and reflectance. In this thesis, absorptance is denoted with F_a, such that

$$F_A = \frac{\Phi_a}{\Phi_i} \tag{2.4}$$

where Φ_a is the absorbed radiant flux and Φ_i is the incident radiant flux. Absorptance is the quantity that is measured with PDS, although it is a relative measurement. The initial data of PDS should therefore be scaled with the help of absolute absorptance data, measured with UV/Vis spectroscopy.

2.4.3. Absorbance

Using UV/Vis spectroscopy methods to measure absorption means that an indirect measurement is used to calculate how light is absorbed. The principle of UV/Vis is that a detector is used behind sample that collects the light that goes through the sample. For non-reflecting samples, this would be sufficient to determine the absorptance, since

$$F_A = 1 - (F_R + F_T) = 1 - F_T \tag{2.5}$$

By doing a reference measurement, the incident light I_0 on a sample is determined and used to calculate F_T

$$F_T = \frac{I_T}{I_0} \tag{2.6}$$

Absorbance A is usually the output of a UV/Vis spectroscopy device, and is defined as

$$F_A = 1 - 10^{-A} \tag{2.7}$$

For non reflecting samples, this means that $F_T = 10^{-A}$, and for reflecting samples the relation is

$$F_R + F_T = 10^{-A} \tag{2.8}$$

The UV/Vis spectroscopy setup at AMOLF contains an integrating sphere where the samples can be placed in during measurements. In an integrating sphere, light in every direction is reflected by the inside walls of the sphere until it is collected by the detector. Effectively, not only the transmitted light is detected, but also the reflected light by the sample. In that way, absorbance can be calculated of reflective samples according to equation 2.8, which implies:

$$A = -log_{10}(F_T + F_R) = -log_{10}(\frac{I_R + I_T}{I_0}) \tag{2.9}$$

2.4.4. Absorption coefficient

According to the Beer-Lambert Law, the previously described absorption quantities can be related to material properties. The amount of intensity attenuation when light passes through a material is described by the absorption coefficient α. With a high absorption coefficient, light can only travel a short path before it is absorbed. With a low coefficient, light travels further and therefore a thin slice of a material may seem transparent. The absorption coefficient is dependent on wavelength λ and can be calculated from absorbance according to

$$\alpha(\lambda) = \frac{A}{d} \times ln(10) \tag{2.10}$$

where d is the thickness of a measured sample. The absorption coefficient is often used for finding relations between the absorption spectrum and indirect or direct transitions using Tauc plots, which will be explained later in this thesis (section 2.6).

2.5. Photoluminescence Quantum Yield

PDS relies on the assumption that the absorbed radiant energy is transferred into heat, so it can be sensed by a probe laser. This is generally a just assumption for most materials. However, $MAPbI_3$ and other perovskites are, besides excellent light absorbers, known to be good optical emitters as well. The Photoluminescence Quantum Yield (PLQY) is the effect of photons being re-emitted after a material is excited by light. When light is absorbed by a semiconductor, it may excite an electron to the conduction band. After some time, the excited electron falls back to the valence band (recombination). This can happen radiatively (the energy is transferred to photon) or non-radiatively (the energy is lost as heat). In the latter case, a PDS setup measures the thermal energy and relates it to the absorption. However, when the energy of an absorbed photon is emitted as a photon, there is less heat generated because the absorbed energy is partly transferred to radiant energy and hence it is not sensed by the PDS setup. These emitted photons are a consequence of absorbed photons, and should be part of the absorption measurement. The PLQY setup can measure what percentage of absorbed photons (N_{absorbed}) is emitted (N_{emitted}).

$$\eta_{\text{PLQY}} = \frac{N_{\text{emitted}}}{N_{\text{absorbed}}} \tag{2.11}$$

The effect that the PLQY has on a PDS measured spectrum becomes clear when we evaluate two cases: an absorbed photon at the bandgap energy and an absorbed photon at an energy higher than the bandgap. When a photon is absorbed at the bandgap ($E_{abs} = E_{BG}$), there is a probability of η that it recombines radiatively. Effectively, $(1-\eta)E_{abs}$ is sensed by the PDS setup, and ηE_{abs} is not. At twice the bandgap energy ($E_{abs} = 2 \cdot E_{BG}$), the energy above the bandgap is fully thermalised, and only at the bandgap energy the exciton has a chance of being re-emitted as a photon. The absorbed energy that is not transferred into heat due to PLQY is thus $\eta \cdot E_{BG} = \frac{\eta}{2} E_{abs}$. This is a smaller fraction than the absorption at the bandgap energy, and therefore it will influence the shape of the measured absorption spectrum.

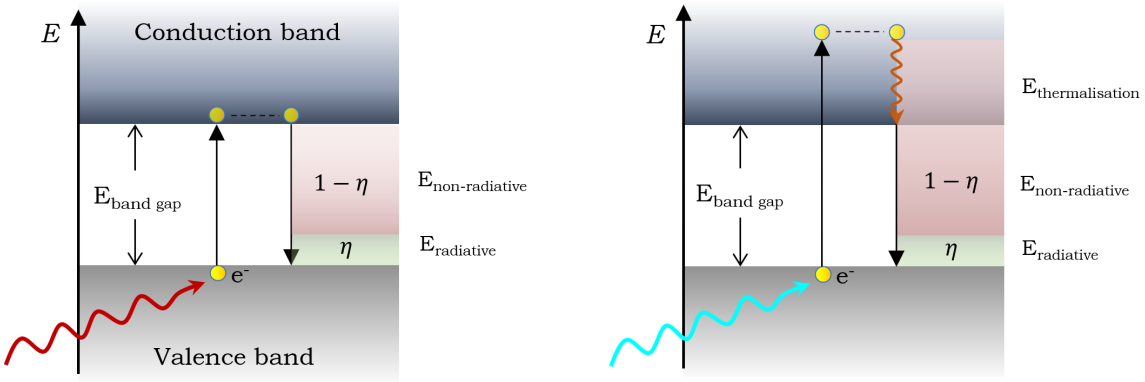

Figure 2.11: Excitation at two different wavelengths. An electron is excited by a light a certain energy. In the left situation, this energy is just enough to excite the electron to the conduction band. In the right situation, the light carries excess energy. The pink parts represent the energy that is converted to heat and thus picked up by a PDS measurement. The green part is missed by a PDS measurement. The green part's contribution to the total absorbed (excitation) energy is relatively smaller in the right situation.

2.6. Tauc plots

A Tauc plot is a way of plotting absorption data to characterize the direct-indirect nature of the optical bandgap [57]. Usually, the absorption coefficient α is used to show $(\alpha h\nu)^{\frac{1}{r}}$ as a function of the photon energy $h\nu$, where $\nu = \frac{c}{\lambda}$ (photon frequency). The exponent r denotes the nature of the transition, such that

- r = 1/2 for direct allowed transitions
- r = 3/2 for direct forbidden transitions.
- r = 2 for indirect allowed transitions
- r = 3 for indirect forbidden transitions

The resulting plot will show a linear regime at the onset of the different transitions. This regime can be fitted with a linear function and extrapolated to find the bandgap where the functions crosses the x-axis:

$$\alpha h\nu = A_r (h\nu - E_{BG})^r \tag{2.12}$$

A_r denotes the proportionality factor for the (fitted) function, dependent on the r that is chosen. α is the absorption coefficient which can be derived from the measured absorptance using the relations in section 2.4. For this, the thickness d of the absorbing layer on the sample is necessary, which will scale the plot (and thus affects only A_r). It does not change E_{BG} or the shape of the plot. Therefore, d is omitted in the analysis in this work.

To successfully characterise an absorption spectrum with the Tauc function (2.12), sensitive absorption data is necessary. Whereas UV/Vis absorption data shows the onset of the bandgap and the regime above the bandgap, it is not sensitive enough to measure far below-bandgap absorption, where the difference between direct and indirect transitions is unveiled.

2.7. Discussion on the bandgap of $MAPbI_3$

In order to fully understand the electronic and optical properties of perovskite solar cells, it is crucial to sort out the mysteries concerning the crystal structure and the bandgap of the materials it is made of. Over the last 5 to 10 years, multiple studies have been conducted with the aim to investigate the direct-indirect behaviour of the bandgap of metal halide perovskites. methylammonium lead halide ($MaPbX_3$), a few of which shown in section 2.1, is intensively reviewed and debated, but still no consensus is reached on the nature of the bandgap. The importance of understanding this property lies in the fact that some of the beneficial properties of PSCs have been related to the nature of the bandgap. In solar cells, the efficiency is partly affected by the time it takes for an excited electron to recombine. When an electron is excited in a solar cell, it will travel to an electrode where its energy can be collected by an electrical circuit (battery, the grid, electrical appliances, etc.). However, before it reaches the electrode, the electron can recombine inside the photovoltaic material and lose the energy as heat (non-radiative recombination) or as an emitted photon (radiative recombination), which can then be re-absorbed by the perovskite. For efficient solar cells, the radiative recombination has to be as fast as possible, while the non-radiative recombination should be zero. Some researchers assume that the long charge carrier lifetimes in metal halide perovskites are a result of an indirect bandgap as a result of Rashba splitting [53, 58, 59]. In the search for finding other (perovksite) solar cell materials that do not have the disadvantages such as instability and poor lifetime, it is essential to understand where the advantageous properties in the material come from.

In my literature study "A direct or Indirect bandgap?"[15], the current academic discussion on the direct-indirect behaviour of metal halide perovksites is comprehensively outlined. This will not be repeated as profound in this thesis, but a few examples of papers that propose conflicting conclusions on the nature of the bandgap are given below.

Richter et al [60] demonstrate in their work that the photoluminescence (PL) at decreasing temperature of metal halide perovskites corresponds with a direct bandgap model. In indirect bandgap materials, radiative recombination is more likely to happen when the temperature is higher. The reason for this is that an indirect combination requires a shift in k-space (momentum space), provided by a phonon. Phonons are generated by the temperature of the lattice. Consequently, for indirect bandgaps, recombination is less likely to happen

when the temperature decreases. This research shows, however, that radiative recombination after excitation is increasing during cooling, which is in agreement with a direct bandgap model (fig 2.12a).

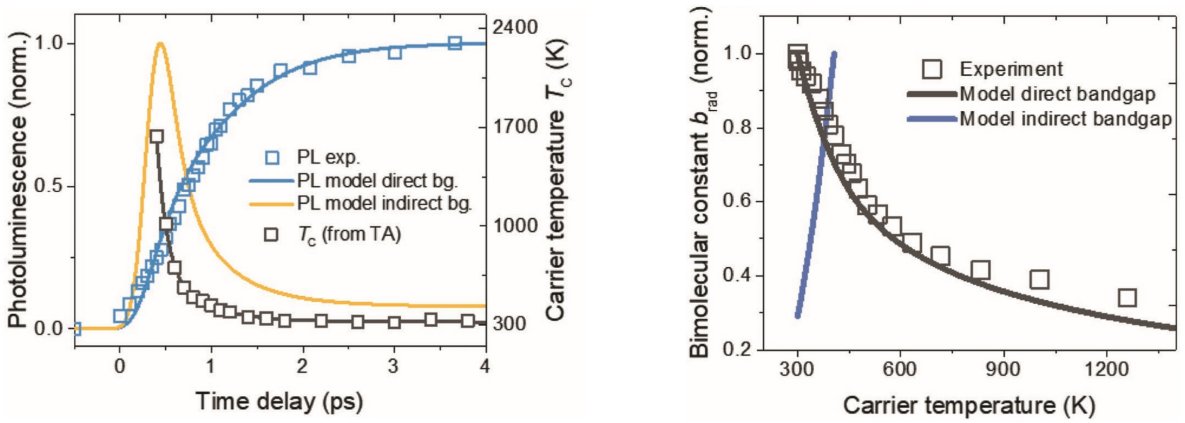

(a) (b)

Figure 2.12: Photoluminesce(PL) during carrier cooling in $CH_3NH_3PbI_3$ according to Richter et al. in figure (a), and the bimolecular constant as a function of carrier temperature, compared to models in (b). Reproduced from [60]

Another study, by Hutter et al. [59], also looks into the effect of different temperatures on photoluminescence of $CH_3NH_3PbI_3$. They find that PL is actually less efficient at lower temperatures, contrary to what is described in the above-mentioned study by Richter et al.. The results are related to an indirect bandgap of the material. They also report that they do not observe the effects when $MAPbI_3$ is in the orthorhombic phase, which is at lower temperatures. This could indicate that the phase change from tetragonal to orthorhombic in $MAPbI_3$ removes the indirect behaviour of the bandgap.

2.7.1. Under pressure

While the influence of temperature on the crystal structure and the bandgap behaviour has been examined intensively, not many studies have looked at the effect of pressure. Wang et al. [31] report an interesting effect on both photoluminescence and absorption when the pressure is increased. Up till a pressure of 325 MPa, both the absorption edge and the PL peak shift towards a lower energy level. Above 325 MPa, there is a sudden shift to a higher energy. In the paper, this effect is explained by a phase change from tetragonal to orthorhombic at 325 MPa, similar to what happens in $MAPbI_3$ when the temperature is decreased below 165 K. The sudden shift above 325 MPa to higher energies (shorter wavelengths) is related to a reduced Rashba effect due to an increase of inversion symmetry. Correspondingly, the bandgap would in that case change from indirect to a more direct nature. In figure 2.13c, data from photothermal deflection spectroscopy (PDS) measurements is used to fit indirect and direct bandgap models of $MAPbI_3$. It shows that the absorption spectrum shows traits of both indirect and direct properties. However, the absorption spectra under different pressures have only been measured with UV/Vis absorption techniques. This opens up a new approach to examine the bandgap behaviour, since PDS is multiple orders of magnitude more sensitive than UV/Vis absorption measurements. The PDS data was taken from literature, and these measurements have not been done in combination with higher pressures.

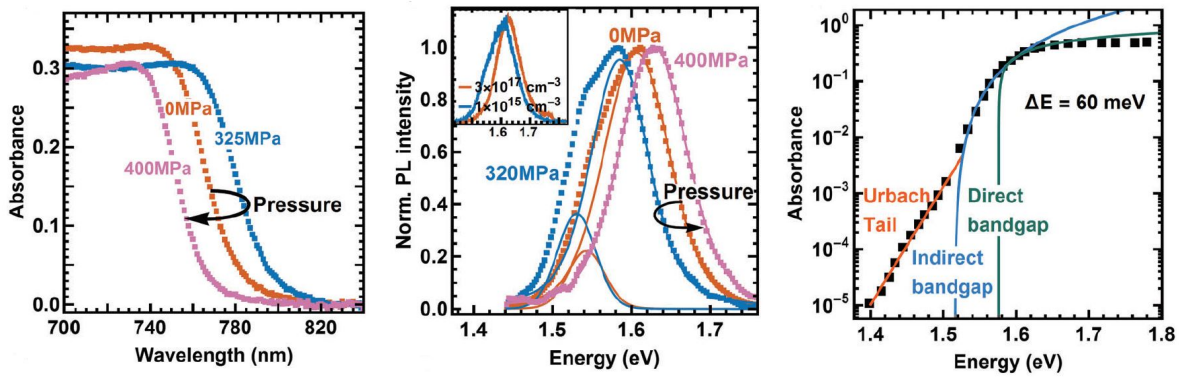

(a) (b) (c)

Figure 2.13: Both (a) and (b) show a shift of the bandgap energy to higher wavelengths (lower photon energy) when the pressure increases. However, after 325 MPa the bandgap suddenly shifts to a higher energy. Figure (c) shows PDS data from literature fitted with an Urbach tail, indirect bandgap and direct bandgap model, indicating a contribution at ambient pressure from both a direct and indirect bandgap to the absorbance spectrum. Figure from [31]

With PDS measurements performed on $MAPbI_3$ at different pressures, the direct-indirect discussion can be provided with new information. Absorption spectra at ambient pressure do not exclude direct or indirect properties, but other research has indicated that the properties might change at different crystal phases. If the material indeed shifts from a non-centrosymmetric tetragonal phase to a centrosymmetric orthorhombic phase, indirect bandgap effects in the absorption spectrum might disappear and direct features may become more prevalent. This would then be visible as a steeper slope of the absorption curve below the bandgap. For these measurements, it is necessary to have a sensitive absorption measurement technique, that can do measurements while keeping a sample under high pressure. According to figure 2.13c, a sensitivity of 10^{-4} with respect to above bandgap absorption is required. As of today, the existence of such a device has not been reported in academic literature.

2.8. Research question

After the literature survey was done before the start of the project, it became clear that there was still a lack of knowledge regarding the direct-indirect nature of the bandgap of certain perovskites. Based on the research that has been conducted previously and the knowledge that is missing on the discussed topics, the following research question was formulated:

*What is the nature of the bandgap of $MAPbI_3$ (direct or indirect) under pressures ranging from atmospheric (*0 MPa*) to* 400 MPa *and room temperature (300 K)*

For successfully answering this question, it is sensible to split up the question in smaller portions that can individually be validated. This leads to the following sub-questions:

1. *Is it possible to design and build a setup that can effectively measure absorption with a sensitivity magnitude in the range of* 10^{-4} *with respect to the above bandgap absorption of $MAPbI_3$, with an adjustable pressure ranging from* 0 MPa *(ambient)* - 400 MPa

2. *What does the absorption spectrum of $MAPbI_3$ look like below the bandgap, down to a sensitivity with a magnitude in the range of* 10^{-4} *with respect to the above bandgap absorption of $MAPbI_3$?*

3. *What is the difference in the shape of the absorption curve below the bandgap of $MAPbI_3$ between different pressures in the* 0 MPa *(ambient)* - 400 MPa *range, and can it be related to a direct or indirect nature of the bandgap?*

As a logical consequence of these three sub-questions, the project was split up in three different phases after the literature survey was finished. Since the first sub-question concerns the feasibility of the design, it can be concluded that this question is successfully answered when a design is build and tested that meets the requirements, or when it is proven that a certain set up is not possible within the resources and limits of the project. This corresponds to a Design phase. Once a working set up is operational, measurements can be conducted during the Measurement phase, which will lead to absorption graphs of $MAPbI_3$ at different pressures. When enough data is collected, analysis will be performed in order to relate the data to bandgap characteristics. The three phases corresponding to the subquestions are thus:

1. *Design phase*
2. *Measurement phase*
3. *Analysis phase*

In reality, the Measurement phase and Analysis phase will be partially overlapping. When the first results are analyzed, it can lead to new insights on how the measurements should be performed, or what parameters should be changed. The overlapping part of the two phases can therefore be seen as an iterative process. Once enough data is collected to make absorption spectra at the full range of pressures, the Measurement phase can be considered finished. A more detailed plan of the project, including a timeline and milestones, is described in appendix A.

2.8.1. Hypothesis

Based on other research that has been performed, the most probable outcome of this research is that $MAPbI_3$ has a slightly indirect bandgap at atmospheric conditions and a direct bandgap at higher pressures (above 325 MPa). This should be visible in the absorption spectrum by using Tauc plots to characterise the transition, and to quantify the bandgap. According to what is published in other studies, the bandgap is expected to decrease in energy when while the pressure is increased; the absorption slope at the bandgap will shift to a lower energy. Above a pressure of 325 MPa, the absorption slope is expected the jump to a higher energy, counteracting the trend below this pressure. The shift from a "direct" to "indirect" slope is harder to quantify, so a more profound data analyses may be necessary to clarify the direct-indirect nature of the bandgap. A clear difference between the spectra can be that Tauc plots of the ambient pressure spectrum can only be fitted with an indirect transition model, whereas Tauc plots of above 325 MPa spectra can only be fitted with a direct transition model.

3

Design

As was stated in the Research question, section 2.8, the project can be split up in three different phases: design, measurement, and analysis. In reality, the three phases are not strictly separated but have an overlapping time span. Proof of concepts, measurements and even analyses of data can lead to new insights that induce alterations to the setup. A widely used framework for a system development project is the V-model [61, 62], as shown in figure 3.1. Following this model, the project can be split up in a specification/design stream, implementation, and a testing/verification stream. The idea is that every requirement of the setup is incorporated in the functional design and that the designed elements can be traced back to the requirements. After implementation, the individual elements will be tested on their required specifications. Iterations can be done after the test results to improve the design elements. When the individual parts satisfy the conditions, the process will be repeated on a higher, integrated level until the setup complies with the initial requirements.

The starting point of the process was the set of initial requirements, which followed directly from the research question. The goal is to produce absorption spectra of $MAPbI_3$ at different pressures. The data needs to be sensitive enough distinguish between traits of indirect absorption and direct absorption. As presented in section 2.7.1, the setup needs to have the following requirements:

I. The setup can measure absorption with a sensitivity magnitude of 10^{-4} with respect to the above band gap absorption

II. The pressure applied on the sample can be increased to 400 MPa, and needs to stay constant during the measurement

Another condition essential to distinguish between two different curves is a high wavelength resolution.

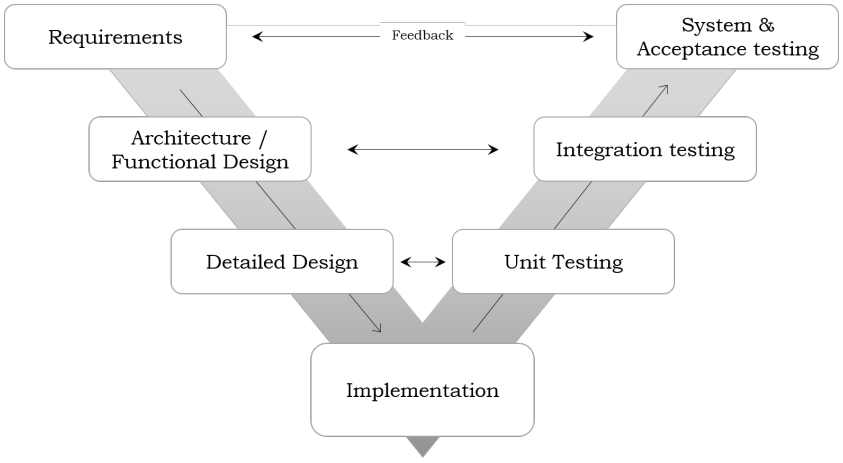

Figure 3.1: The V-model, a framework for the design process that makes sure that every requirement is incorporated in the design and validated.

Quantifying this is not trivial, because the final absorption spectra from direct and indirect phases is yet unknown. However, from simulations in literature data and PDS measurements at ambient pressure, it is possible to make an estimate of a sufficient wavelength resolution. As can be seen in graph 2.13c[31] and in other PDS data of $MAPbI_3$ [63–66], the absorbance of $MAPbI_3$ decreases by four orders of magnitude in the energy range from 1.45 eV - 1.6 eV. This corresponds to a wavelength range of about 80 nm (775 nm - 855 nm). With at least 10 different data points in this range, resolving a curve should be possible. This would results in a resolution requirement of 8 nm. Looking at simulations for the direct and indirect contribution to the absorption curve [31] (figure 2.13c), it can be seen that an energy difference of 60 meV - 100 meV is predicted between a purely direct and purely indirect absorption slope. In the case of 60 meV (1.52 eV - 1.58 eV), the wavelength difference is roughly 30 nm. Having 5 data points in between seems enough to properly distinguish between the two curves. This results in a resolution of 6 nm. Because the excitation (pump beam) source usually has a Gaussian spectral profile, it is common practice to take the Full Width Half Maximum for the resolution. In this way, there is only a small spectral overlap between data points. This consideration leads to the third requirement:

III. The setup is able to measure independent data points with a wavelength resolution of 6 nm

From an extensive literature study on perovskite solar cell materials, it was already known that an effective and widely-used absorption measurement technique is PDS. It has already proven to be able to measure $MAPbI_3$ with the required sensitivity (I) and resolution(III). The second requirement, doing the measurement under higher pressure, is not yet demonstrated. The first step in the design process was therefore to propose a preliminary design that is able to comply with the basic requirements: Doing sensitive absorption measurements, making the measurement wavelength specific and having the ability to increase the pressure on the sample. A standard design of a PDS setup is shown in figure 3.2. The standard design in its simplest form is only adapted by including a pressure cell. The sample is inside the cell, so pressure can be applied on the sample. The cell must have windows to let both the pump beam (shown in green) and the probe beam (red) into the cell. The probe beam can travel out through a window on the opposite side.

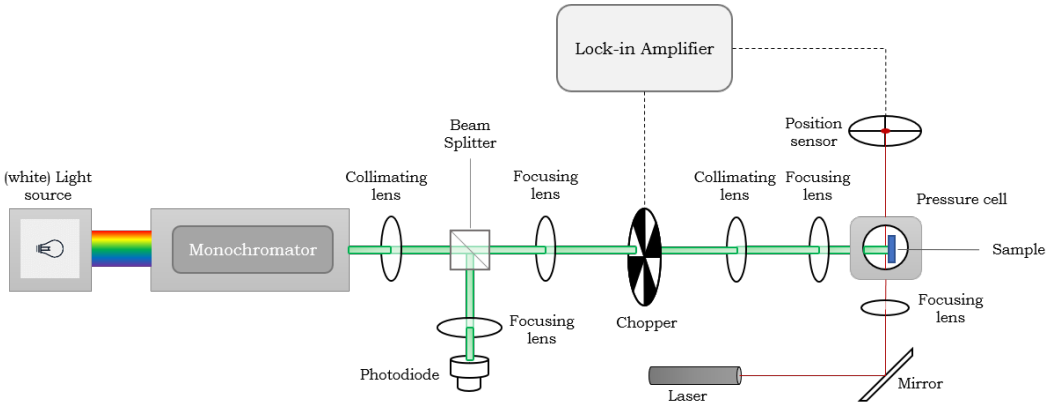

Figure 3.2: The preliminary design of the setup: a conventional PDS setup with a pressure cell added to apply pressure on the sample

To satisfy the specific requirements, including the quantified sensitivity, resolution and pressure, every single element of the setup is evaluated to find the necessary improvements. The basis for finding these improvements lies in the paper by Jackson et al.[19], where the relation between the performance and the setup parameters are presented. The key to high sensitivity measurements is improving the signal-to-noise ratio S/N. When S/N is low, a noise floor is quickly reached when measurements are done in a low absorption regime. With a high S/N, even in low absorption regimes the signal is significantly higher than the noise. This is a necessary property for the ability to measure in these regimes. The signal is proportional to the deflection of the laser. A higher signal is thus reached by increasing the deflection. One way to do this is by making sure there is a large temperature gradient, because the gradient is the driver behind the deflection. A high temperature gradient can be obtained by focusing as much light as possible (from the pump beam) on a small area on the sample. Other elements that improve the signal are the lock-in amplifier in combination with the chopper, and the probe laser/position detector properties. These elements are described in the section below.

Figure 3.3 shows a sketch with the coordinate system in the pressure cell. This coordinate system is later used in drawings representing the inside of the pressure cell. Other parts in the setup (such as the quadrant/position sensor) have their own coordinate system that does not necessarily overlap with the coordinate system of the pressure cell.

3.1. Requirement I: Improving the sensitivity

In this section, the setup elements are elaborated that affect the S/N ratio of the measurement, leading to a high sensitivity. The methods described improve the signal by increasing the deflection, by optimizing the probe laser parameters and by signal processing with a lock-in amplifier. The latter is described first.

3.1.1. Lock-in amplifier and chopper

A lock-in amplifier, in combination with a chopper, is a device that is able to vastly improve a signal from a noisy environment. It is possible to extract a signal that is much smaller than the noise component. This is

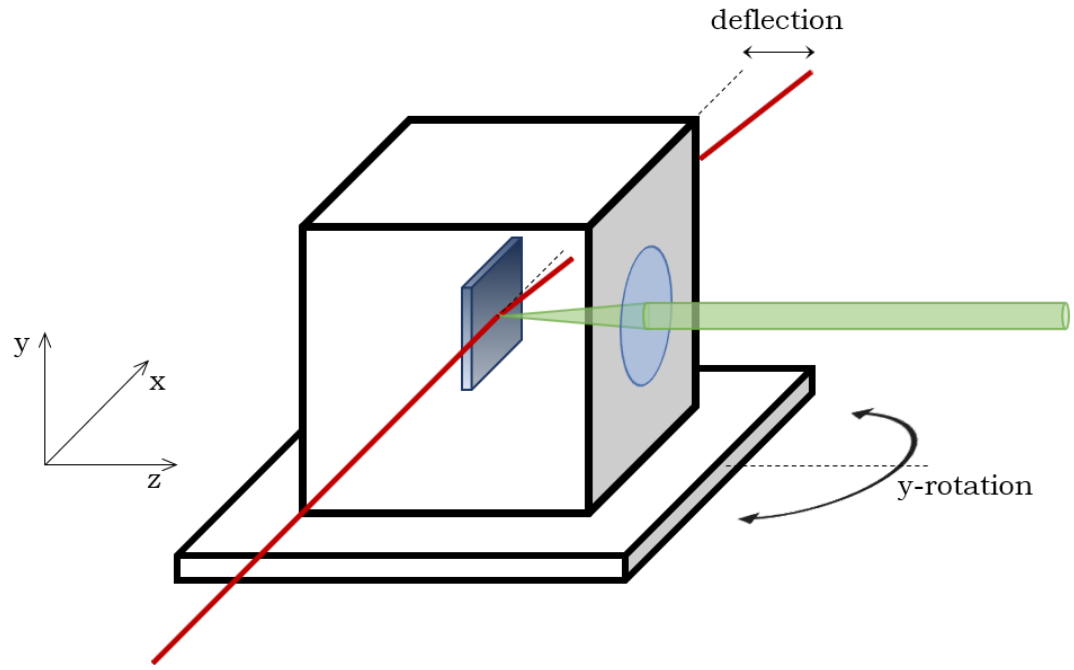

Figure 3.3: Sketch showing the direction of the coordinates at the pressure cell. Important to notice is that this coordinate system is not the same as the coordinate system at the quadrant sensor, which has its own x and y coordinate system.

done by modulating the input source of the signal with a certain reference frequency (f_{ref}). As a result, the measured signal will be modulated with the same frequency. The lock-in amplifier is then able to filter out other frequencies and amplify only the reference frequency. In this way, only the signal with the frequency that is induced by the input source is extracted from the measured signal. In a PDS setup, the input source is the pump beam, which is modulated by a chopper. A chopper is nothing more than a rotating disk with periodic slits, modulating the pump beam with a constant frequency, proportional to its circular velocity, by blocking and unblocking the light. The probe beam is deflected due to the heat of the pump beam. This deflection will therefore modulate with the same frequency as the input source (pump beam).

The working principle of a lock-in amplifier is based on a simple mathematical principle. The following explanation is adapted from the manufacturer's website of the lock-in amplifier that was used [67]. When two sine waves with different frequencies (ω_1 and ω_2) are multiplied (without the DC component), a new sine wave is created that has a different period. An important property of the new wave is that it oscillates symmetrically around zero, just as the former waves. In fact, the new wave is a superposition of two waves, one at the difference frequency ($\omega_1 - \omega_2$) and the other at the sum frequency ($\omega_1 + \omega_2$). Writing it in equation form, with ω being the frequency, θ their phase and A the product of their amplitudes $A_1 \cdot A_2$:

$$A\sin\left(\omega_1 t + \theta_1\right) \cdot \sin\left(\omega_2 t + \theta_2\right) = \frac{A}{2}\cos\left([\omega_1 - \omega_2]t + [\theta_1 - \theta_2]\right) - \frac{A}{2}\cos\left([\omega_1 + \omega_2]t + [\theta_1 + \theta_2]\right) \tag{3.1}$$

Interestingly, when two sinusoids of the same frequency are multiplied, the difference component ($\omega_1 - \omega_2$) becomes zero, leaving behind a constant value. In signal processing, the constant value or DC signal can be extracted from AC signals by using a low-pass filter. When the two input signals have a different frequency, the

low-pass filter will fully block the output because it consists of only AC signals. When the input signals have the same frequency, the output contains a DC signal which will not be blocked by the filter. In this way, out of a signal consisting many frequency components, the component with the same frequency as a reference frequency can be extracted. In case of an ideal low-pass filter, the output signal V_{out} will be:

$$V_{\text{out}}(t) = \frac{1}{2} V_{\text{ref}} V_{\text{sig}} \cos(\theta_{\text{sig}} - \theta_{\text{ref}}) \tag{3.2}$$

where V_{ref} the amplitude of the reference frequency and V_{sig} is the amplitude of the measured signal, proportional to the deflection amplitude of the probe laser in the setup. This means that the output signal V_{out} is proportional to $V_{\text{sig}} \cos\theta$, where $\theta = \theta_{\text{sig}} - \theta_{\text{ref}}$. $\cos\theta$ can vary between 0 and 1, depending on the phase difference. It is possible to manually adjust the phase of the reference signal such that $\theta = 0$, but most lock-in amplifiers calculate the same signal with a 90^{o} phase shift. In this way, the output has a X and Y component, after which the magnitude R is calculated to remove the phase dependency:

$$X = V_{\text{sig}} \cos\theta \tag{3.3}$$

$$Y = V_{\text{sig}} \sin\theta \tag{3.4}$$

$$R = \sqrt{X^2 + Y^2} = V_{\text{sig}} \tag{3.5}$$

$$\theta = \arctan(Y / X) \tag{3.6}$$

In reality, the low pass filter is not ideal and a tradeoff has to be made between signal accuracy and the time it takes to suppress the signals. Suppressing signals with a frequency close to the reference frequency requires a longer time, because the difference frequency $(\omega_1 - \omega_2)$ is close to zero, but still nonzero. This tradeoff can be made using the time-constant and roll-off setting on the lock-in amplifier, as is described in section 4.5.

The chopper is the mechanical device that modulates the pump beam signal. It is of great importance that the vibrations within the chopper, which rotates at the reference frequency, do not propagate to other elements in any way. Especially the probe beam, the sample or the position detector should not be influenced by the chopper. The chopper is therefore not attached to the same optical table as the other elements, like the laser, light source, sample stage and all the lenses. Instead, the chopper is hanged from a construction above the table, that is fixed on the ceiling of the room. The pump beam is focused before the chopper and collimated afterwards, to make sure that the diameter is small enough to fit through any slit size of the chopper, as shown in figure 3.4

3.1.2. Light source and photodetector

The light source for the pump beam is part of a combination device build by Sciencetech (TLS-55-X300). It is a tunable light source, which means that the wavelength can be automatically adjusted using a monochromator and filter wheel. This will be discussed later in section 3.3. To achieve a good signal, it is key to make sure that enough light can be focused on the sample. A simple way to improve the intensity is by starting with a powerful light source. Light intensity will be lost at every element, but starting with a higher intensity will

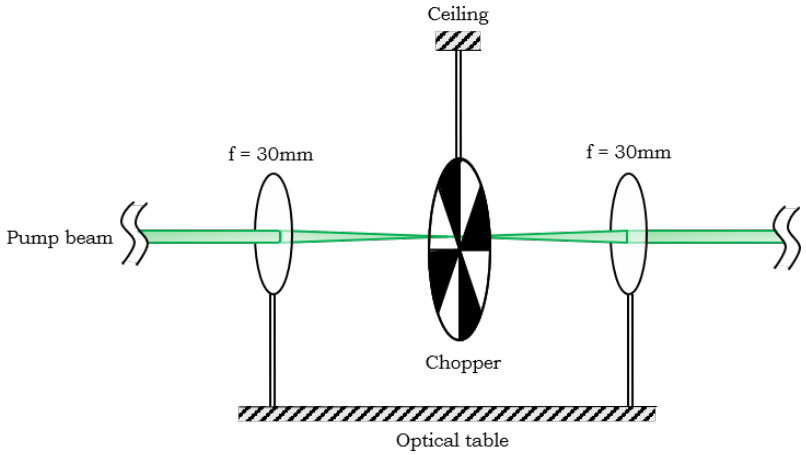

Figure 3.4: The chopper is connected to the ceiling, whereas the other elements are all installed on an optical table. This prevents vibrations from the chopper to be transmitted to the other elements.

result in a higher intensity at the end of the beam path. The light source used for the pump beam is a xenon lamp of 300 W. It is one of the most powerful light sources available on the market, but it is not a perfect point source. As a consequence, it is not possible to perfectly collimate the light beam or (near) perfectly focus it, which would be possible with a laser beam.

Another aspect of a Xenon lamp is that the white light is not homogeneous in intensity over all wavelengths. The monochromator filters out all wavelengths except a desired one, but is does not normalize the intensity. More intense wavelengths will therefore result in a higher deflection amplitude, and therefore a higher measured signal. When this effect is not taken into account, it will look like there is more absorption at wavelengths with high pump intensity. To compensate for this effect, the intensity of the pump beam is measured with a photodetector. The photodetector is placed just after the monochromator, where the beam is split by a beamsplitter. To make sure that only a small amount of intensity is lost due to this measurement, the beamsplitter splits the light with a ratio of 90:10, where 10% is sent to the photodetector. Before or after a sample is measured, the photodetector is placed at the sample position, where the pump beam intensity over the complete spectrum is measured. The ratio of intensity between the light that hits the sample, and the light that hits the photodetector at its regular position after the beamsplitter is now known. During a measurement, the intensity of the pump beam is measured and afterwards related to what the intensity at the sample was.

3.1.3. Photodetector working principles

The working principle of the detector is based on the simple silicon photodiode, that converts light into an electric current. A Thorlabs SM1PD1A photodiode was used in combination with a Thorlabs PBM42 bias module. This is a device that puts a certain bias voltage on the photodiode. A reverse bias voltage increases the responsivity and linearity of the photodiode. The saturation limit and sensitivity of the photodiode can be tweaked by choosing the right bias voltage and load resistance, over which the signal is measured. The signal is collected by an auxilirary input of the lock-in amplifier, which can accept a maximum voltage of 10 V. The lock in amplifier only collects the signal and sends it to a computer where it is stored.

The effect of choosing different parameters for the voltage bias and the load resistance can be seen in figure 3.5a and 3.5b. A higher voltage bias leads to a higher saturation limit. Because of the maximum voltage of 10 V of the aux input of the lock in amplifier, the bias voltage is chosen to be 9 V. Then, the load resistance is taken such that the wavelength with the highest intensity does not lead to a saturated signal (< 8.5 V was sufficiently safe). This was done before every measurement cycle. The wavelength with the highest intensity for $MAPbI_3$, where the measurement range is roughly 650 nm - 850 nm, turned out to be 830 nm. To fully utilize the linear regime, the most powerful wavelength (830 nm) should result in a signal that is as high as possible, without being saturated. The load resistance was chosen accordingly. With this method, the photodiode operates as sensitively as possible.

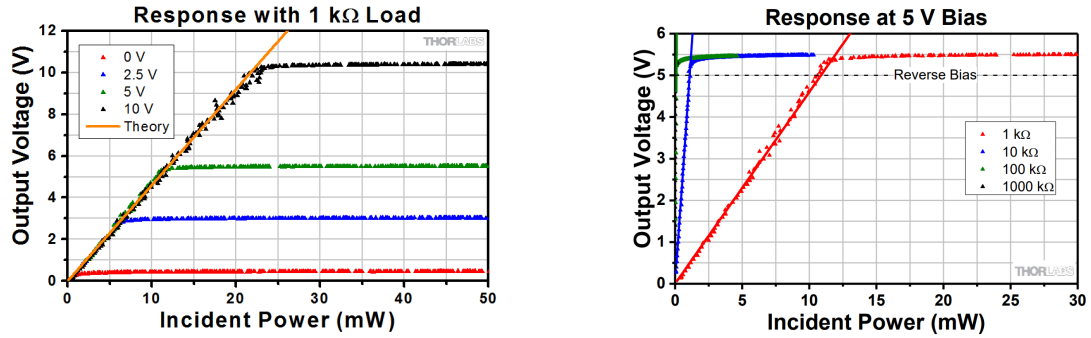

(a) (b)

Figure 3.5: The effect of choosing different parameters for the voltage bias (figure (a)) and load resistance (figure (b)) on the output signal. The bias voltage is chosen such that it does not exceed the lock-in amplifier limit, and the load resistance such that the most powerful wavelength falls within the linear regime. Data from Thorlabs photodiode lab [68]

Furthermore, it is important to notice that the photodiode has a certain responsivity to different wavelengths. This is an effect of thermalisation losses above the bandgap of silicon. As a result, the same intensity at a different wavelength leads to a different output voltage. This responsivity is measured by Thorlabs itself and is used to calibrate the intensity measurements of the photodiode. The correct relation between the output signal (V_{out}) and the actual intensity of the incoming light (P) is:

$$V_{\text{out}}(t) = P(\lambda) \cdot \Re(\lambda) \cdot R_{\text{load}} \tag{3.7}$$

where P is the light power, $\Re$ is the responsivity of the photodiode and R_{load} is the load resistance. Because PDS is a relative absorption measurement, it will be scaled according the the shape of a UV/Vis measurement. The actual value of the load resistance is not necessary for the correction, because it does not change for different wavelengths. It only needs to be correctly chosen, such that the photodiode operates in its linear regime and does not reach the saturation limit.

3.1.4. Pump beam focusing on the sample

From the paper by Jackson et al. [19] describing the sensitivities of important parameters in a PDS setup, it is clear that a tight focus of the pump beam is key to achieving a high signal. A tighter focus leads to a smaller spot size, resulting in a higher power on a smaller area. The consequence is a larger temperature gradient

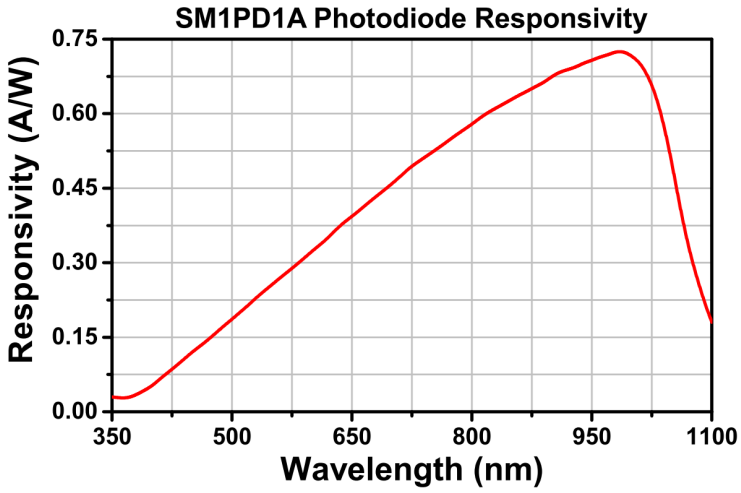

Figure 3.6: The responsivity of the used photodiode. The same intensity light at different wavelengths will result in a different photocurrent, causing the signal to vary depending on the incident wavelength of the light. Data from the Thorlabs photodiode webpage [69]

and more deflection of the probe beam. To estimate the ideal spot size, a straightforward thermodynamic relation is used [70, 71]. The thermal penetration depth δ is defined as the distance a heat wave will travel in a certain time. At the penetration depth distance, the temperature difference is roughly 1/e compared to the heat source location (sample surface) and the temperature gradient is close to 0. The penetration depth depends on the thermal diffusivity a of the material, defined as the conductivity κ, divided by the specific heat c_p and the density ρ. The thermal diffusivity measures the rate of heat transfer through a material from a hot to cold side. The time that a material is heated is related to the frequency of the chopper, which controls the frequency of the pump beam. $\omega_0 = 2\pi f$, such that

$$\delta = \sqrt{\frac{2\kappa}{\omega_0 c_p \rho}} = \sqrt{\frac{a}{\pi f}} \qquad \text{where } a = \frac{\kappa}{c_p \rho} \tag{3.8}$$

The thermal penetration depth gives an indication of the length scales that the photothermal effect operates on. It is later used to calculate the desired probe beam size. For the pump beam, it can be concluded that a desired spot size is within the range of the penetration depth in the sample. The penetration depth in the liquid is important for the laser probe beam dimensions. Penetration depths inside $MAPbI_3$ and the medium are calculated for different frequencies and shown in table 3.1

Table 3.1: The thermal penetration depths in both a $MAPbI_3$ sample and the liquid used as medium (FC-72)

	20 Hz	40 Hz	80 Hz
$MAPbI_3$	59.2 µm	41.8 µm	29.6 µm
FC-72 (liquid)	22.9 µm	16.2 µm	11.5 µm

To achieve spot sizes in this order of magnitude, the collimated pump beam should be focused with a lens or

an objective with a large Numerical Aperture (NA). The pump beam does not originate from a perfect point source, therefore the spot on the sample is always an image of the source with a certain (de)magnification. The NA is approximated by $\frac{D}{2f}$, where D is the diameter of the beam entering the lens/objective, and f is the focal distance. A larger magnification, and thus a smaller spot, requires a higher NA and therefore a shorter focal distance or a larger beam diameter. This is where the setup is limited by the pressure cell (see also section 3.2). Due to the dimensions of the pressure cell, the distance between the last optical element and the sample is limited to roughly 50 mm. The diameter is in that case also limited be the entrance aperture of the pressure cell: roughly 25 mm. The exact NA is actually defined by the conical shape of the entrance shaft in the pressure cell. Since there are no objectives available on the market with a working distance as large as 50 mm, an achromatic lens is the best option. To come as close to the sample as possible, a Thorlabs achromatic lens with a focal length of 50 mm was adapted by slightly reducing the diameter, such that it could fit perfectly in the entrance shaft of the pressure cell. I was placed inside a Thorlabs CMV10 adjustable extension tube, that could be screwed in and out of the shaft to focus the lens.

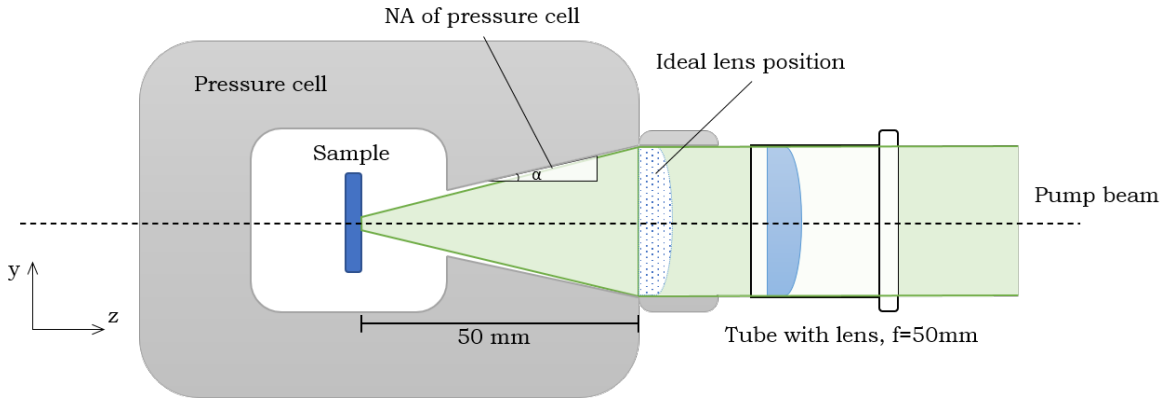

Figure 3.7: The limitations induced by the pressure cell. A shorter working distance between the lens and the sample is preferable to achieve a smaller spot size, but the cell limits this to 50 mm

3.1.5. Laser probe beam

The probe beam is directed perpendicular to the pump beam through the pressure cell, parallel to the sample and grazing the surface of the sample. The laser used in the PDS setup is a Thorlabs LDM635. It is a compact laser diode module that outputs a 635 nm (red) laser beam of 4 mW. The shape of the beam is elliptical, 3 mm by 5 mm in size. As was explained above, the penetration depth of the thermal wave in the liquid is very narrow, in the range of 20 µm, depending on the chopping frequency. For achieving a strong signal, it is preferable that the probe laser fully deflects. Therefore, the laser needs to be focused on the region in the liquid where there is a temperature gradient. Another option would be to reduce the diameter of a collimated laser instead of focusing it. However, the laser would need to be a 1000 times smaller in diameter, which is not practical to do without losing a lot of intensity. This would make a deflection almost undetectable and very noisy.

Other studies have already looked into analytical and numerical methods to optimize the laser beam param-

eters for the purpose of PDS [72–74]. Finding the optimal parameters for the probe beam can be done based on the restrictions induced by the pressure cell and the sample width. Figure 3.8a shows a schematic overview of the probe beam near the sample surface. The beam is modelled as a focused gaussian beam. The diameter of the beam (D_{probe}) before the focusing lens and the focal distance of the lens (f_{probe}) determine the divergence Θ and the waist w_0 of the beam. The depth of focus, DOF, is the range around the waist where the diameter of the beam is max $\sqrt{2}w_0$. It is also known as twice the Rayleigh length. From a simulation study by Foley [74], it was concluded that with PDS the highest signal (V_{max}) is obtained when the center of the beam is at a distance of $\sqrt{2}w_0$ from the sample (see figure 3.8b). This case is depicted in figure a, where the sample is at this distance from the beam center, without blocking the beam. The relations describing the dimensions

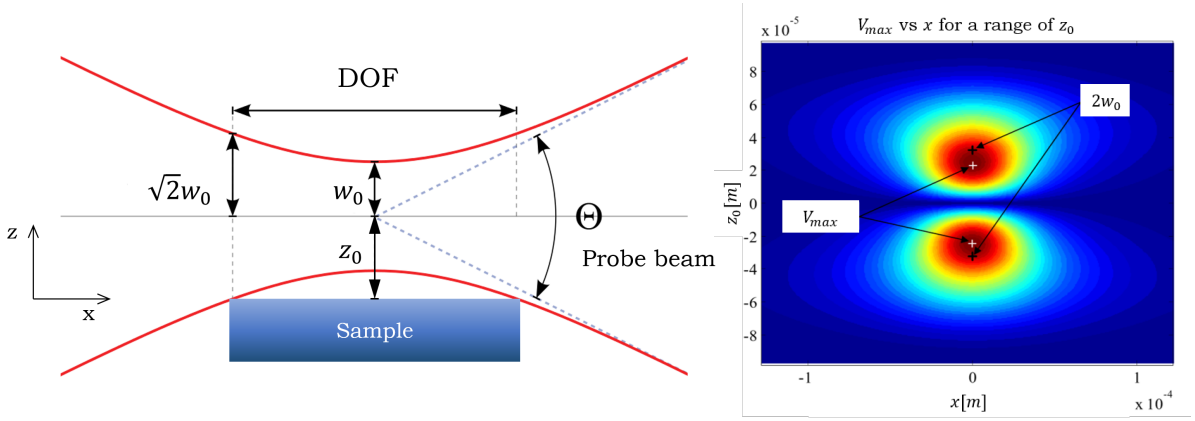

(a) (b)

Figure 3.8: The beam parameters close to the sample are shown in (a). The situation shown is for a certain lens and beam diameter such that the sample width is equal to the depth of focus (DOF). In (b), it can be seen that the signal for PDS is highest when the beam center is $\sqrt{2}w_0$ away from the sample. This is the case for the situation in (a). Figure (b) is adapted from [74]

of the probe beam (which is a gaussian beam) as shown in figure 3.8a are [75]:

$$w_0 = \left(\frac{2\lambda}{\pi}\right)\left(\frac{f_{\text{probe}}}{D_{\text{probe}}}\right) \tag{3.9}$$

$$DOF = \left(\frac{8\lambda}{\pi}\right)\left(\frac{f_{\text{probe}}}{D_{\text{probe}}}\right)^2 \tag{3.10}$$

With this information, it can be concluded that the desirable DOF should equal the sample width. Using the relations described in equations 3.9 and 3.10, the diameter and focal length can be calculated. One restriction is that the probe lens should be outside the pressure cell, to allow for alignment corrections (the pressure cell, including the sample should be able to move with respect to the probe beam, such that the probe beam can be aligned in z-direction). The focal length needs to be larger than 50 mm. Therefore, a 75 mm lens is chosen. With this lens and a standard sample width of 11 mm, the resulting diameter of the probe beam $D_{\text{probe}} = 0.95$ mm. The waist of the beam is in this case 33 µm. The calculations are done with a Python script, which can be seen in Appendix C.1

The diameter of the probe beam can be adjusted with an iris before the lens. It should be noted that choosing a larger focal length of the lens results in a larger diameter of the probe beam needed to achieve the same waist and DOF. Another way to adjust the beam diameter is by reducing the beam size with 2 lenses (beam

expander/reducer). With this method, the smaller beam diameter is obtained with losing only little intensity with respect to using an iris. A high probe laser intensity is preferable for the performance of the quadrant sensor, as explained below. For this reason, a set of lenses was used to reduce the beam diameter, instead of an iris. The ideal probe beam diameter D_{probe} of 0.95 mm is desired. The laser dimensions at the aperture of the laser is 3 mm by 5 mm. The beam reducer is made by placing two lenses with focal lengths of 100 mm and 30 mm at 130 mm from each other (sum of the focal lengths). The beam diameter is reduced with a factor $\frac{3}{10}$, roughly approaching the desired diameter of 0.95 mm.

3.1.6. Quadrant Sensor

To effectively measure a small deflection, a very sensitive detector is necessary. Jackson et al. [19] have evaluated two types of position sensors: a lateral detector and a quadrant detector. They find a similar sensitivity for both detectors when used in a PDS setup. For this setup, a Thorlabs PDQ80A quadrant sensor is used. To translate the sensor data into a position value, a Thorlabs K-Cube Position Sensing Detector is connected to the position sensor. The Thorlabs K-Cuve also digitizes the position data to make it available for a graphical user interface on a computer.

A quadrant sensor consist of four independent photodiodes, positioned as four quadrants of a circle. They are seperated by a ~0.1 mm wide gap. A position of a laser beam can be calculated by measuring the intensity on all four sensors. If a laser beam is aligned at the center of the four photodiodes, the same photocurrent will be induced on all four sensors. When a beam moves away from the center, some sensors will receive more intensity whereas others receive less intensity of the laser beam. The difference in two directions (x and y) can be calculated by subtracting the intensities on one side by the intensities on the other side. This results in a X_{diff} and Y_{diff} value. Also, the sum of all four intensities is collected for normalization purposes.

$$X_{\text{diff}} = (Q2 + Q3) - (Q1 + Q4) \tag{3.11}$$

$$Y_{\text{diff}} = (Q1 + Q2) - (Q3 + Q4) \tag{3.12}$$

$$\text{SUM} = Q1 + Q2 + Q3 + Q4 \tag{3.13}$$

To improve the signal, one might think that it is helpful to move the quadrant sensor further away from the sample. Because the deflection is basically an angle between the original laser path and the deflected laser path, the absolute distance that the center of the laser beam has moved (Δx) is larger when the detector is further away from the sample. However, this does not lead to a higher X_{diff}. As can be seen in figure 3.9, the beam diameter is also larger when the detector is moved further away from the sample. The beam is divergent after the sample, because it is focused on the point where it crosses the pump beam. Moving the detector twice as far away from the sample, results in twice the Δx, but also twice the diameter of the beam. Proportionally, the total intensity of the beam is divided exactly the same over the four quadrants in the two situations.

Increasing the intensity of the laser does help to improve the signal. Let's assume that the beam has moved slightly to the right (as in figure 3.9). The total intensity on the quadrants is as follows: $Q1 = Q4 = 1$, $Q2 =$

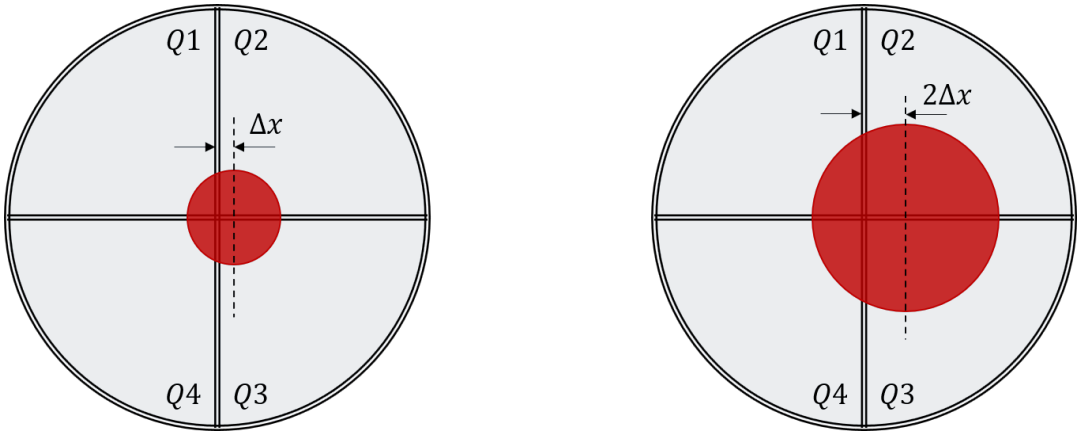

Figure 3.9: Two examples of a divergent beam on a quadrant sensor. When the quadrant sensor is twice as far away from the sample (right figure), the beam diameter is also twice as large. Although the center of the beam has moved twice the distance (Δx), the X_{diff} value is the same for both left and right situations

$Q3 = 2$, such that the total intensity SUM = 6. In this case, $X_{\text{diff}} = (2+2) - (1+1) = 2$. When the intensity is doubled, $Q1 = Q4 = 2$, $Q2 = Q3 = 4$, and SUM = 12. Now, $X_{\text{diff}} = (4+4) - (2+2) = 4$. The signal for X_{diff} has also doubled. For this reason, it is chosen to achieve the right beam diameter before the focusing lens (D_{probe}) by reducing the beam via lenses, instead of an iris that reduces the beam by blocking the outer part of it. The focal lengths of the lenses used for reducing the beam diameter were calculated in the previous section.

At last, a bandpass filter is added to the path just before the beam hits the quadrant position detector. The bandpass filter is a Thorlabs FLH635-10, which only allows the probe beam light with a wavelength of 635 nm to pass. This is done to reduce noisiness induced by other light sources. Especially the pump beam light, that might be scattered or reflected from other directions, should not reach the quadrant sensor, since it is modulated at the reference frequency. Otherwise, this would lead to a high signal being picked up by the lock-in amplifier. A schematic overview of the complete probe beam path is visualized in figure 3.10.

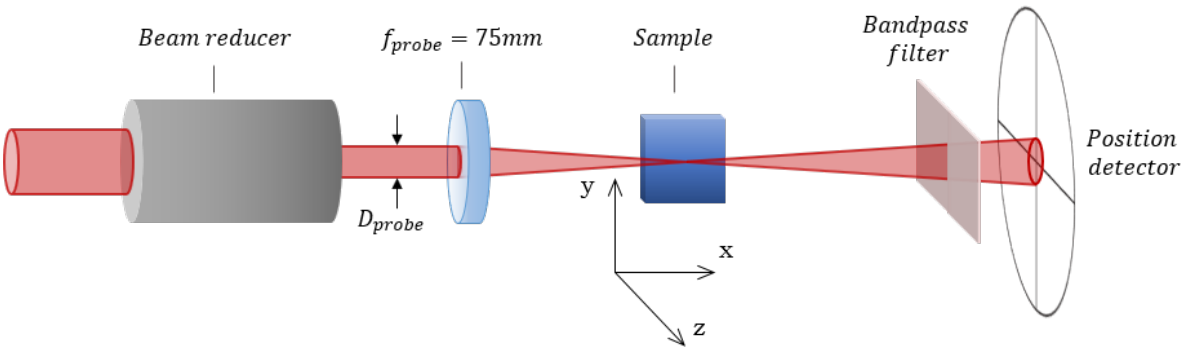

Figure 3.10: A schematic overview of the probe beam path, from the source to the quadrant sensor. The coordinate system shown represent the system at the sample, inside the pressure cell. The coordinate system of the quadrant sensor is not shown

3.2. Requirement II: Applying pressure

For this research, it was important that the pressure on the sample could be increased up to 400 MPa. For this, a high-pressure cell system manufactured by ISS inc. was used. The cell is basically a stainless steel cube that is roughly 100 mm wide, long and tall. It has four sapphire windows, one on each side at an angle of 90^o from each other. The cell can withstand pressures up to 400 MPa.

The entrance shafts of the windows are conical, and thus define a maximum NA to the center of the pressure cell, where the sample is located. This NA is 0.18, as stated on the website of ISS inc. [76]. When a lens is used with a NA that is higher than or close to 0.18, the lens is not the limiting factor anymore for creating a small focus spot. Whereas the focusing lens for the probe beam was chosen to be 75 mm, for the pump beam, a lens with a focal length of 50 mm is chosen. The aperture diameter is 25 mm, and therefore the NA of the lens is 0.25. With a 75 mm focal length, the NA would be 0.167, which is lower than the maximum NA that the pressure cell allows.

The liquid inside the pressure cell is FC-72 (perfluorohexane, C_6F_{14}), or Fluorinert^{TM}, produced by 3M. FC-72 is highly inert, thermally and chemically very stable, and has a constant low absorption of the wavelengths used in this work. The liquid has a high change in refractive index over temperature, $\delta n/\delta T = 4 \times 10^{-4}\,\mathrm{K}^{-1}$. This is about 400 times higher than the change in refractive index over temperature of air, and 5 times higher than water [77]. The FC-72 was purified by purging it with nitrogen using a Schlenk line, to remove any traces of oxygen or other gasses from the liquid.

Applying pressure was done manually by pressure generator compatible with the ISS pressure cell. The liquid FC-72 was added to a reservoir and pressurized with a hydrostatic pump. Flexible steel tubing was used to connect the reservoir with the compartment inside the pressure cell. A pressure gauge on the pump system indicated the pressure that was applied.

3.3. Requirement III: Resolution

To resolve an accurate absorption spectrum, the setup needs to be able to measure per wavelength with a good resolution. When the sampling interval is set to be around 6 nm, the FWHM should be roughly the same. If the FWHM is much wider, there will be too much overlap to consider the datapoints independent. A FWHM that is too narrow is not a big problem, but information between datapoints is lost since these wavelengths are not used in the measurement, and the intensity will be much lower compared to a wider FWHM. The device that filters out the wavelengths and can be tuned to control the FWHM and the intensity, is the monochromator. The monochromator used in the setup is a Sciencetech 9055 monochromator, as part of the Tunable Light Source configuration.

A monochromator is a device that can split white light, consisting a wide spectrum of wavelengths, such that every wavelength goes into a slightly different direction. The incoming light is reflected by a grating, that diffracts the wavelengths at specific angles. The grating can be rotated in order to direct the desired

wavelength to an output slit. A narrow slit results in a better spectral resolution, but also compromises the intensity. A side effect of a grating is that higher harmonics of a specific wavelength are also reflected in the

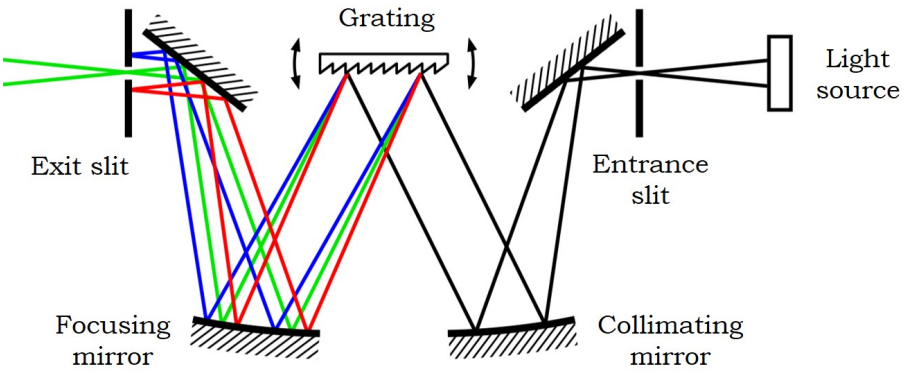

Figure 3.11: The working principle of a monochromator. Light is split in different directions for every wavelength

same direction as the 0th order, although with lower intensities. The harmonic wavelengths are unwanted, and should thus be filtered out. This can be done using a long pass filter, that blocks all wavelengths shorter than a certain cut-off wavelength. The long-pass filters are integrated in the Tunable Light Source before the monochromator. Unfortunately, the long exposure times and high power light source in the PDS measurement can result in burning of the filters (see appendix B). For safety, the automatic filter wheel is removed and a suitable filter is manually installed after the monochromator, where the light has lost already a great amount of intensity.

Choosing a suitable filter depends on the range of wavelengths that is scanned during a measurement. Because PDS is a relative measurement, it is preferable not the alter the setup during a measurement: A slightly worse alignment will result in a shift in the signal, distorting the measured spectrum. Luckily, the spectrum that is interesting for $MAPbI_3$ is quite narrow. The scanned spectrum will be from 650 nm to a maximum of 900 nm, which covers a regime well below and above the band gap. The longest wavelength in the scan, 900 nm, has its first harmonic at 450 nm. This is far lower than 650 nm, the shortest wavelength in the spectrum. A long pass filter between these two wavelengths is therefore sufficient to cancel all the harmonics during a scan. Table 3.2 shows the first three harmonics of the lower and upper bound of the wavelength range used for $MAPbI_3$. It can be seen that a longpass filter between 450 nm and 650 nm will suppress all harmonics. The filter used here is a 610 nm hard coated longpass filter.

Table 3.2: The desired wavelengths of a full scan and their harmonics. When the scan is within a small range (the longest wavelength is less than twice the shortest wavelength), the scan can be done without a filter change

Harmonic	Start wavelength	-	Stop wavelength
0	650 nm	-	900 nm
1st	325 nm	-	450 nm
2nd	216.7 nm	-	300 nm
3rd	162.5 nm	-	225 nm

After the filter, a Thorlabs CCS100 spectrometer is installed to check whether the harmonics are rejected

and only the desired wavelength is left. The spectrometer is also used the check the FWHM and intensity of the pump beam. The input and output slit of the monochromator are both adjustable in width. They are manually adjusted to obtain an output beam with a FWHM of roughly 7 nm, with the maximum intensity obtainable for that FWHM.

in figure 3.12, a complete overview of the setup is shown, including all components that have been discussed in this chapter. Both the photodetector(photodiode) and the quadrant sensor(position sensor) are connected to the lock-in amplifier, but the photodetector data is directly send through to the PC without signal processing. Only on the quadrant sensor signal, the frequency lock-in process is performed.

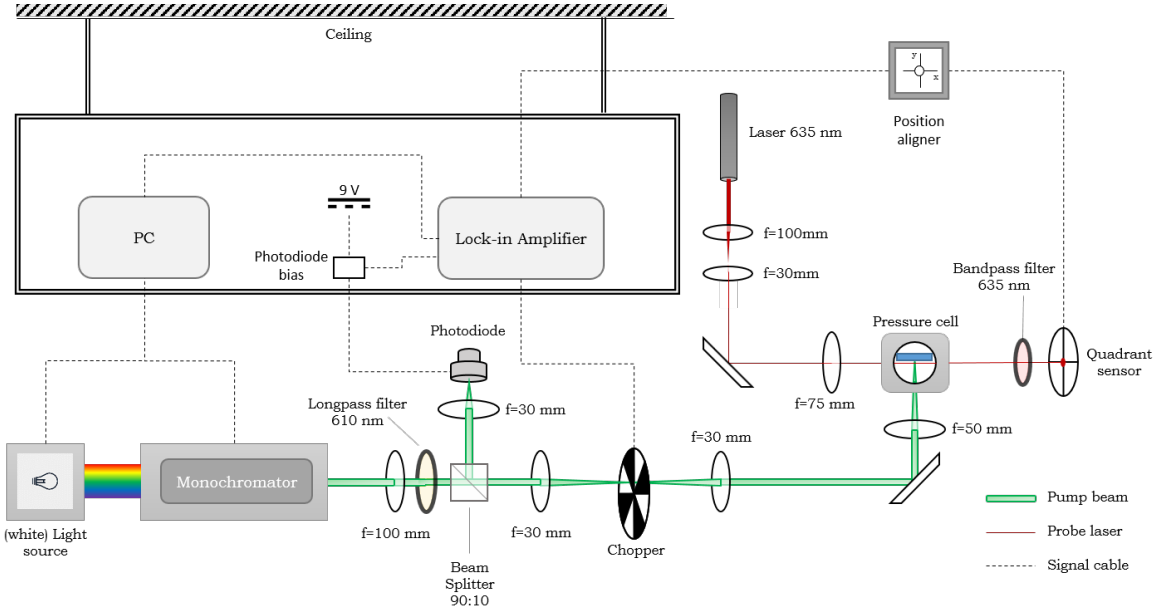

Figure 3.12: A schematic overview of the full setup, including all signal processing devices

4

Experimental Methods

4.1. Sample preparation

The fabrication of the samples was done by Eline M. Hutter and Loreta A. Muscarella. They describe their method in the Supplementary Information of their paper "Thermodynamic Stabilization of Mixed-Halide Perovskites Against Phase Segregation" [78]:

> *Quartz substrates were sonicated with deionized water, acetone, and isopropanol sequentially for 15 minutes, followed by an oxygen plasma treatment for 20 minutes at 100 W. The solvents N,N-dimethylformamide (DMF, Sigma Aldrich anhydrous, ≥ 99%) and dimethylsulfoxide (DMSO, Sigma Aldrich anhydrous, ≥ 99.9%) were mixed in a 4:1 (DMF:DMSO) volume ratio. The solvent mixtures were used to prepare stock solutions of lead iodide (TCI, 99.99%, trace metals basis), CH_3NH_3I (MAI, TCI, >99%), lead bromide (Sigma Aldrich, trace metals basis) and CH3NH3Br (MABr, TCI, >98%) by dissolving these precursors at 1.1 M. $MAPbI_3$ and $MAPbBr_3$ solutions were prepared by mixing the MAI with PbI_2 and MABr with $PbBr_2$ stock solutions at 1:1 molar stoichiometric ratios (i.e. 1:1 v:v). The $MAPb(I_{1-x}Br_x)_3$ precursor solutions were prepared by mixing x parts $MAPbBr_3$ stock solution with (1 - x) parts $MAPbI_3$ stock solution, resulting in 1.1 M $MAPb(I_{1-x}Br_x)_3$ solutions. The films were prepared by spin-coating the precursor solutions on quartz substrates at 9,000 rpm for 30 s and anti-solvent of Chlorobenzene (Sigma Aldrich, anhydrous, ≥ 99%) was dropped 15 s after the start of spin-coating, followed by thermal annealing at 100 ^{o}C for 1 hour. Both the preparation and spin-coating of solutions were done in a nitrogen-filled glovebox.*

4.2. UV/Vis absorption

Since a PDS setup can only perform relative measurements (a value per wavelength relative to other wavelengths), a UV/Vis measurement is used to find the absolute absorbance. This measurement is not as sensitive as PDS, but is accurate near and above the bandgap. The PDS measured spectrum can then be scaled to the correct absolute value. A LAMBDA 750 UV/Vis/NIR spectrophotometer (Perkin Elmer) was used to measure an absorption spectrum. It does not measure absorption directly, but only the light that is not absorbed by a sample. For this, a sample was placed inside an integrating sphere, which is a device that reflects all the light that entered the sphere until it is absorbed by the sample, or absorbed and detected by a photodetector. The reflected and transmitted light is thus collected and measured. Using the relations in section 2.4, the absorbance can be calculated. These relations also describe the difference between PDS absorptance and UV/Vis absorbance, necessary to scale the PDS spectrum such that it overlaps with the UV/Vis spectrum.

A $MAPbI_3$ sample was placed inside an integrating sphere to measure the absorbance. This was done under ambient pressure. Measuring the absorbance under other pressures is not possible in combination with an integrating sphere. Instead, the pressure cell could be placed inside the spectrophotometer sample chamber. However, without the integrating sphere only the light that is directly transmitted can be measured in this configuration. The reflected light is not detected. The calculated absorbance spectrum is therefore significantly less accurate, since it calculates the absorbance by measuring transmitted light and neglecting the light that is reflected (and scattered, diffracted) by the sample.

4.3. Degassing

Pressurizing the liquid FC-72 leads to a "milky-like" effect, causing the liquid to scatter more light. This highly compromises the performance of the setup, since both the pump beam and the probe beam are partly scattered before they reach the sample. To reduce this effect, the liquid should be purified using a Schlenk line. The liquid is poured into a flask and connected to the Schlenk line. Using liquid nitrogen, the FC-72 is cooled until it is completely frozen and then placed under vacuum. Due to the freezing, only the gasses inside the liquid escape. The Schlenk line sucks the gasses out of the flask and then it is refilled with nitrogen (gas). To process of freezing and clearing the gasses is repeated 3 times. The flask is closed off air tight during the complete process and afterwards placed in a nitrogen-filled glove box.

4.4. Pressurizing the sample

To increase the pressure on the liquid in the cell, a manual pressure generator (hydrostatic pump) by ISS Inc. is used. The degassed liquid and a sample are placed into the cell inside a nitrogen-filled glovebox, making sure that the pressure cell is completely filled with liquid. The pump has a reservoir that is filled with the same liquid. The pump is used flush the pressure chamber, tubing and pressure gauge which removes remaining air and completely fill it with FC-72. At the PDS setup, the pressure cell is connected to the pump with the

flexible tubing. The pump can now be used to pressurize the cell. This is done in steps of 50 MPa, with a minute rest in between to let the pressure equalize over the cell which prevents overstressing the windows of the cell.

The pressure gauge is connected to the tubing and used to read out the pressure inside the cell. If measurements are done over a longer period of time (e.g. several hours), the pressure may slightly decrease during the measurement. It might be necessary to pump extra liquid into the cell to keep the pressure at the same level during the measurement. To prevent a bias induced by adjusting the pressure, extra pumping is done every time the monochromator switches to a new wavelength. This is further explained in the PDS methodology.

4.5. Photothermal Deflection Spectroscopy

Once the sample is placed inside the pressure cell, the liquid has been degassed and a UV/Vis and PLQY measurement have been done, the PDS setup can be used. The first step is determine the slit width of the monochromator. The monochromator has an input and output slit that can be adjusted to optimize the wavelength resolution of the pump beam. A trade-off has to be made between resolution and intensity of the pump light. For the measurement of $MAPbI_3$, a sampling interval of 5 nm was chosen. The FWHM of the pump light was set to 7 nm. This results in a small overlap between wavelength set points. The measurement is therefore slightly oversampled, but no information is lost due to undersampling [79]. Using the beam splitter, that is installed to lead a part of the beam to the photodetector, a beam is directed into a Thorlabs CCS100 Spectrometer. The spectrometer is also used to check if there are no harmonic wavelengths present in the pump light, which is a side effect of a monochromator. For $MAPbI_3$, the measured spectrum is 650 nm - 850 nm. A long pass filter with a cut-on wavelength of 610 nm is placed after the monochromator to remove the harmonics.

Next, the signal of the photodiode is checked. As was explained in section 3.1, a 9 V bias voltage of the photodiode is applied with a stable voltage supply, and the right load resistor was chosen such that the signal does not saturate. A wavelength scan over the full spectrum is done and the intensity data is stored in a computer. The photodetector is then placed at the sample position, where later the pressure cell is placed. Also for this position a wavelength scan is done and the intensity data is stored. These two measurements are used to find the relation between the intensity measured at the beam splitter path and at the sample position. During a regular PDS measurement, for every wavelength the intensity is measured by the photodetector. Using the reference measurement, it can be calculated what the intensity of the pump light on the sample is.

Once the pump beam is ready, the pump and probe beam are aligned such that the focus points (beam waists) exactly overlap. This is done using mock-up pressure cell with a mock-up sample. The mock-up sample has a small pinhole in its center that is used to align the beams. The mock-up cell has exactly the same dimensions as the real pressure cell. It is placed at the position where the pressure cell is going to be. The pinhole sample is rotated 45 degrees. In this way, both the pump and probe beam (which are 90 degrees shifted with respect to each other) can be focused on the pinhole. Adjustable mirrors in the beam path are used to steer the beam paths, and the focusing lenses of the beams can be shifted to place the focus on the pinhole. The

intensity after the pinhole is measured of both beams. When the intensity is at a maximum level, the beams are considered to be focused on the pinhole and perfectly aligned. After this, the mock-up cell is replaced with the actual pressure cell containing the sample. The mock-up cell itself is also filled with the liquid (FC-72) to resemble the actual situation with the pressure cell as good as possible. It can even be used for performing measurements under ambient pressure. However, applying pressure on the liquid is not possible with the mock-up cell. This will slightly change the refractive index of the liquid when the actual pressure cell is used. Aligning the sample with the mock-up cell can only be done at ambient pressure, which is sufficient as a rough starting alignment when the mock-up cell is replaced by the pressure cell. Once pressure is applied, alignment should be redone, but the optimal parameters will be close to the initial alignment parameters already obtained with the mock-up cell.

With the actual sample, the setup is aligned by optimizing the signal. The pump beam is set to 650 nm (an above-bandgap, highly absorbed wavelength), and the chopper is set to 23 Hz. A higher frequency can be used, which would lead to less noise but also a lower signal amplitude. 50 Hz should be avoided to prevent interference with the electric grid frequency. The quadrant position sensor is positioned such that the probe beam is at the center of the four quadrants. It is connected to the A input of the lock-in amplifier. A low time constant (Tc) (1 second) on the lock-in amplifier is used for alignment, because it results in quick signal changes when a lens or stage is adjusted. The stage with the pressure cell is then aligned in z-direction and in y-rotation, maximizing the signal. This leads to a minimal z_0 distance between the probe beam and the sample. The setup is re-aligned before every measurement, which is important when a new pressure is applied.

With an aligned setup, the measurement can be started. A computer with dedicated software for the setup, developed at AMOLF, was used to control the devices and store the data in one .txt file. A long Tc on the lock-in amplifier is key to probe the absorption at wavelengths far below the bandgap, where the signal is very low. Depending on the time available for a measurement, the Tc can be chosen. A Tc of 100 seconds was a default setting that results in a reasonable absorption spectrum. It is important to keep in mind the chosen roll-off of the filter setting on the lock-in amplifier results in different times for the lock-in amplifier to find a stable signal (See table 4.1).

Table 4.1: The waiting time necessary for the signal to stabilize depends on the chosen roll-off parameter of the filter and the chosen Tc

Roll-off filter	Minimal waiting time
6 dB/octave	3 · Tc
12 dB/octave	5 · Tc
18 dB/octave	7 · Tc
24 dB/octave	9 · Tc

During a measurement, 10 · Tc seconds per wavelength was chosen to store the data with a roll-off filter of 18cB/Octave. The extra time was taken to ensure that enough data is stored, since the signal is still noisy in the low absorption region. A measurement of 650 nm - 850 nm, with an interval of 5 nm and a Tc of 100

seconds, takes a total time of:

$$\#\text{intervals} \cdot \text{Tc} \cdot \text{Tc}_{\text{multiplier}} = 41 \cdot 100\,\text{s} \cdot 10 = 41\,000\,\text{s} = 11.4\,\text{h} \tag{4.1}$$

After all settings are applied, a measurement can be started. If it was necessary to adjust the pressure during the measurement (because of liquid leakage), this was done every time at the start of a new wavelength setpoint.

4.6. PLQY measurement

The PLQY of a material affects the outcome of the measured PDS spectrum, as described in section 2.5. We can account for this effect by measuring the PLQY of $MAPbI_3$. For this, a sample is placed inside an integrating sphere with a photodetector. The sample is excited by a laser with a wavelength of 532 nm. A fraction will be absorbed, and a fraction of the absorbed energy will be re-emitted at a wavelength corresponding to the bandgap (~750 nm). The PLQY is defined as the ratio of the number of photons re-emitted by the material (N_{em}), to the number of photons absorbed by the material (N_{abs}). Using a long pass and a short pass filter before the photodetector, the excitation and emission wavelengths can be measured for their photon flux. By measuring the intensity of both wavelength when the laser hits the sample, and doing reference measurements when the sample is removed from the integrating sphere, one can derive the photon flux that gets absorbed and the flux that gets re-emitted, as described in equation 4.2 [80]. For a better S/N, an optical chopper is placed in the excitation path and the photodetector is connected to a lock-in amplifier.

$$\eta_{\text{PLQY}} = \frac{N_{\text{em}}}{N_{\text{abs}}} = \frac{E_B - E_A}{S_A - S_B} \tag{4.2}$$

E_A is the reference photon flux at the emission wavelength, E_B is the measured emitted photon flux, S_A is the reference excitation photon flux and S_B is the scattered (not-absorbed) photon flux of the excitation laser. E_A and E_B are measured with the long pass filter that allows the emission wavelength to hit the photodetector, S_A and S_B are measured with the short pass filter that transmits the excitation wavelength. Subscript A denotes reference measurements when there is no sample in the excitation beam path, and subscript B denotes measurements when the excitation beam hits a sample. In the next section, it is explained how the measured PLQY is used in the analysis of the PDS measured data.

4.7. PDS Analysis

The PDS measurement data is stored in a .txt file, which contains the lock-in amplifier settings and the necessary signals (X, Y, R, θ (phase) and intensity). The data is copied to a .csv file, which is then analysed with a Python script. When all the data loaded, the first step is to correct the absolute signal R for the intensity. R is the signal that is directly proportional to the deflection of the probe beam. Before it can be related to absorption, it should be corrected for the intensity of the pump beam at every wavelength.

Since the intensity that hits the sample is not directly measured, it is derived from the intensity signal measured after the beam splitter (I_{bs}). The two reference measurements at the sample position ($I_{ref.sample}$) and at the beam splitter path ($I_{ref.bs}$) are used to correlate the measured intensity to the intensity at the sample. Also, because the photodetector has a different sensitivity for different wavelengths (Responsivity $\Re$), the intensity measurement needs to be corrected for that. All intensity signals are directly measured without filtering or other signal processing, so the mean of the intensity signals is taken as intensity value.

$$I_{corrected}(\lambda) = I_{bs}(\lambda) \cdot \frac{I_{ref.sample}(\lambda)}{I_{ref.bs}(\lambda)} \cdot \frac{1}{\Re(\lambda)} \tag{4.3}$$

It is important to notice that all I signals as described in the equation above do not denote the actual radiant power of the beam (in Watt). Instead, they represent signals (in V) proportional to the power of the light beam. To obtain the power in Watt, the signals would need to be corrected for the used load resistor according to Ohm's law and the responsivity $\Re$ (see equation 3.7). Since the unit of $\Re$ is AW^{-1}, the unit of $I_{corrected}$ is $VA^{-1}W$, which can be converted to W by dividing the total by the load resistance (in Ω). However, at a later stage, the spectrum is going to be scaled according to the UV/Vis spectrum. Therefore, scaling it with a resistance which is constant over the spectrum will not make a difference.

The lock-in amplifier needs some time to find a stable signal. This time is related to the settings chosen, as described in table 4.1. Only the stable signal is representative for the actual absorption, so the rise of this signal needs to be trimmed off. Therefore, the signal at a certain wavelength is plotted to determine how much needs to be trimmed. As a default, the values in table 4.1 can be taken. When the data is trimmed to

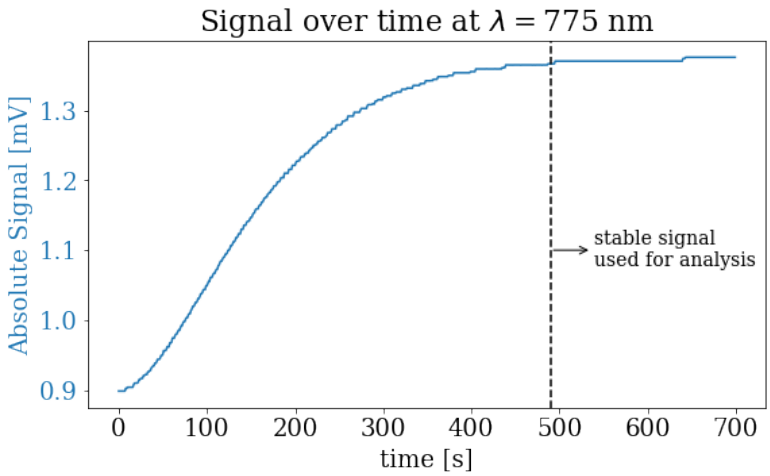

Figure 4.1: The absolute signal R over time at a wavelength of 775 nm is shown. The used settings are: a filter roll-off of 12 dB/octave and a Tc of 100 seconds. According to the rule of thumb, the first 500 seconds need to be trimmed off since that is the stabilizing time of the lock-in amplifier. The exact cutting position can be chosen manually

contain only the stable part of the signal, the mean and standard deviation of the absolute signal R are taken, which will be used to calculate the absorptance and the statistical error. Also the standard deviation of the phase θ is taken for the stable period, since this gives an indication of how well the lock-in amplifier is able to extract the signal from the noise. The unscaled absorption ($F_{a.unscaled}$) is then calculated by taking the mean

of the signal R in the stable region and dividing it by the intensity signal.

$$F_{\text{a.unscaled}}(\lambda) = \frac{\overline{R}_{\text{trimmed}}}{I_{\text{corrected}}} \tag{4.4}$$

To find the actual absorptance F_a, the unscaled absorption $F_{\text{a.unscaled}}$ needs to be scaled according to the UV/Vis absorption spectrum. The UV/Vis spectrometer measures absorbance A. To convert this to absorptance, the relation 2.7 in section 2.4 is used. With the correct UV/Vis absorptance data, the PDS absorptance data can be scaled to the right absolute value. For this, a wavelength that is just above the bandgap (750 nm) is chosen where the UV/Vis absorptance is accurate. The PDS absorptance is scaled to overlap at this point with the UV/Vis.

$$F_{\text{a.PDS}}(\lambda) = F_{\text{a.unscaled}}(\lambda) \cdot \frac{F_{\text{a.uv/vis}}(\lambda = 750\,\text{nm})}{F_{\text{a.unscaled}}(\lambda = 750\,\text{nm})} \tag{4.5}$$

At last, a correction for the PLQY effect is described in section 2.5 is added. For this, two assumptions have to be made, based on other measurements. The PLQY was measured with the setup, but for the correction also an emission wavelength has to be assumed. This emission wavelength for $MAPbI_3$ has been measured at different pressures by Wang et al. [31]. The emission wavelength at ambient pressure is 770 nm, corresponding to a bandgap $E_{\text{BG}} = 1.61$ eV. The spectrum wavelength axis is converted to energy, using Planck's relation $E = hc/\lambda$. The correction for the PLQY is

$$F_{\text{a.PDS.corrected}}(E) = F_{\text{a.PDS}}(E) \cdot \frac{E}{E - E_{\text{BG}} \cdot \eta_{\text{PLQY}}} \tag{4.6}$$

Where E is the photon energy, corresponding to a certain wavelength, E_{BG} is the bandgaps energy, η_{PLQY} is the PLQY and $F_{\text{a.PDS}}$ is the PDS absorptance, uncorrected for the PLQY effect. To obtain the absorption coefficient, which is used for the Tauc fitting described in the next section, the relations from section 2.4 are used. The script that fully analyses the PDS data and plots absorptance spectra is presented in appendix C.2.

4.8. Tauc fitting

For the fitting of the data, the Python package statsmodels.api is applied, performing a linear regression model using ordinary least squares. First, the measured PDS data is converted into a Tauc plot with the following x and y axes:

$$y = (\alpha h\nu)^{1/r}$$

$$x = h\nu$$

Then, the data is fitted with a linear fit, where the axis intercept is the bandgap E_{BG}. This is done for both direct ($r = 1/2$) and indirect ($r = 2$) separately, but also for a combination of the two, since $MAPbI_3$ is expected to have both a direct and indirect contribution to the bandgap. The model describing the combination of an indirect and direct bandgap to the absorption spectrum is adapted from Kirchartz et al. This is shown in the

equation below, where subscript i denotes indirect and subscript d denotes direct. [81]

$$\alpha h\nu = \begin{cases} A_{\mathrm{r,i}}(h\nu - E_{\mathrm{BG,i}})^2 & \text{for } E_{\mathrm{BG,i}} < h\nu < E_{\mathrm{BG,d}} \\ A_{\mathrm{r,i}}(E_{\mathrm{BG,d}} - E_{\mathrm{BG,i}})^2 + A_{\mathrm{r,d}}(h\nu - E_{\mathrm{BG,d}})^{1/2} & \text{for } h\nu > E_{\mathrm{BG,d}} \end{cases} \tag{4.7}$$

The indirect model is fitted first to find the linear regression and the indirect bandgap by extrapolating. Then, using a loop, a range of direct bandgaps is tested to find the best transition value between the direct and indirect model. The direct bandgap $E_{\mathrm{BG,d}}$ represents the transition point, where the indirect absorption is set constant and the direct contribution is added, such that $\alpha_{\mathrm{eff}} = \alpha_i + \alpha_d$. The final transition energy between direct and indirect is chosen based on the highest R^2 value the the combination of the fits has.

At last, the exponential tail is fitted using the relation describing the Urbach tail as presented in section 2.2.6. This exponential regime, representing the very low photon energies ($< E_{\mathrm{BG,i}}$), is not fitted by either the indirect or direct model. The Urbach fit is added to the total model, and the transition point between the Urbach fit and the indirect model is where both models overlap. The Python script that does the tauc plotting and fitting can be seen in appendix C.3.

5

Scientific Paper

In this chapter, starting on the next page, the results of the project are presented in the style of a scientific paper. Contrary to the rest of this thesis, the focus in this paper lies more on the obtained data, analysis and conclusions on the MAPI bandgap and lacks a proper explanation of the newly-designed PDS setup. This paper is therefore intended to be published in a journal that generally contains papers on the chemistry and fundamentals of perovskites, rather than a journal that focuses on scientific instrumentation.

Sensitive absorption measurements under pressure suggest an indirect-to-direct bandgap transition of $CH_3NH_3PbI_3$ Perovskite

Marnix M. Ackermans [1,3], Eline M. Hutter[1,2], Bruno Ehrler[1]

[1] *Center for Nanophotonics, FOM Institute AMOLF, Science Park 104, 1098 XG Amsterdam, The Netherlands*

[2] *Department of Chemistry, Utrecht University, Princetonlaan 8, 3584 CB, Utrecht, the Netherlands*

[3] *Department of Precision and Microsystems Engineering, Faculty of Mechanical Engineering, Delft University of Technology, Mekelweg 2, 2628 CD Delft, the Netherlands*

Email: B.ehrler@amolf.nl

The rapid rise in power conversion efficiency of perovskite solar cells and consequent exponential growth of research interest has led to an increased understanding of its physical and chemical properties. $CH_3NH_3PbI_3$ (MAPI) is generally considered to be a direct bandgap semiconductor, but some evidence suggests a spin-orbit induced Rashba splitting of the conduction band due to a lack of inversion symmetry around the Pb site, inducing a slightly indirect bandgap. Here, we present new empirical evidence using photothermal deflection spectroscopy under hydrostatic pressure, showing a transition from a primarily indirect bandgap at ambient pressure to a more direct bandgap at 375 MPa. By fitting absorption data using Tauc plots, we show that in a combined direct-indirect transition model the bandgaps move closer together above 325 MPa, indicating a less distinct indirect bandgap as a result of the phase change that MAPI undergoes at 325 MPa. The resulting models show that the absorption data is well explained by an indirect transition model for lower pressures, but both a direct and an indirect model required to explain the behaviour at 375 MPa.

Introduction

Over the last decade, metal halide perovskites (ABX_3, where A is a cation, B is a metal and X a halide) have gained increased attention in the scientific community because of their excellent photoelectric properties and potentially cheap manufacturing possibilities [14, 22]. Especially in photovoltaic applications, Perovskite Solar Cells (PSCs) have drawn great attention with the increase in power conversion efficiency of 3.8% in 2009 to over 25% as of today [12, 82, 83]. Although the physical explanation of many of the beneficial properties of metal halide perovskites is not clear yet, some of them are related to the bandgap of the material. This letter specifically focuses on the direct-indirect nature of the bandgap of $CH_3NH_3PbI_3$ (MAPI). It has been previously proposed [16, 17, 59] that an indirect bandgap in PSCs can be the origin of long charge carrier lifetimes, resulting in a higher probability of excitons being collected before they recombine, even though for very-high efficiency solar cells the indirect bandgap can actually be harmful for the efficiency [81].

Other potential applications for metal halide perovskites are (X-ray) photodetectors and, LEDs and lasers [18, 84]. For light-emitting devices, it is important that the charge carriers can efficiently recombine radiatively, without the need of assisting phonons [85]. A direct bandgap is therefore preferable. A proper understanding of the electronic band structure is thus cru-

cial for engineering metal halide perovskites for specific opto-electronic applications.

The exact description of the bandgap structure of metal halide perovskites is currently under debate. For example, methylammonium lead iodide (MAPI) was commonly believed to be a direct bandgap semiconductor at ambient conditions[60, 86, 87], but multiple publications contradict this theory by showing evidence of an indirect bandgap [17, 31, 59, 88, 89]. The underlying explanation for the indirect bandgap is generally thought to be the Rashba effect, a result of spin-orbit coupling in a non-centrosymmetric crystal structure. The Rashba effect splits the conduction band at the bandgap, causing a shift in momentum for the conduction band minimum (CBM) dependent on the spin of the electron. The indirect bandgap is distinguished from the direct variant by both a shift in momentum and a slightly different bandgap energy [31].

The asymmetry in the crystal causing the Rashba effect can be the result of either the bulk structure or of dynamic movements and rotations of the ions. There is no definite consensus on the bulk structure of MAPI, since some report a tetragonal crystal system with a non-centrosymmetric space group *I4cm* [37, 38, 90] and others report a centrosymmetric *I4/mcm* space group in the ambient phase [30, 38], naturally leading to a discussion if Rashba splitting is possible. When cooled down to a temperature of 165K, MAPI is known to undergo a phase change to a centrosymmetric orthorhombic *Pnma* structure, and to a cubic centrosymmetric $Pm\bar{3}m$ structure above 333K. These phases would rule out the static Rashba effect. Several publications therefore report evidence based on photoluminescence (PL), absorption or computational modeling while temperature is changed [17, 60, 86, 88]. Even without the phase change, a varying temperature can be relevant since the phonon-assisted indirect transition is temperature dependent. Recently, MAPI was analysed from a different perspective by applying hydrostatic pressure on samples while doing PL and UV/Vis absorption measurements [31]. At 325 MPa, a similar phase change from tetragonal to orthorhombic, accompanied with a change from an indirect to a direct bandgap, was concluded.

Here, we present new empirical evidence on the matter by performing sensitive absorption measurements using Photothermal Deflection Spectroscopy (PDS) under various pressures. PDS can measure the absorption of MAPI for photon energies far below the bandgap. This allows us to analyse the obtained absorption spectra with Tauc plots. The Tauc plots were fitted with a models for both a direct and an indirect transition, indicating the nature of the bandgap at different pressures. We find that at ambient conditions, the absorption spectrum of MAPI can be explained by a combined model for an indirect and direct bandgap, with a strong component from the indirect model. However, contradicting to what was reported previously [31], we do not see a complete disappearance of the indirect bandgap above 325 MPa, although the model for the direct bandgap is able to explain the spectrum better at high pressure with respect to ambient pressure.

Methods

The PDS setup was designed at AMOLF and controlled by software developed in-house. MAPI samples were placed inside a pressure cell by ISS inc. and submerged in a FC-72 liquid from 3M. A combination of a 300W Xenon lamp with a monochromator (produced by Sciencetech) created a monochromatic pump beam that was focused to the sample. The pump light creates a temperature gradient in the liquid around the exitation spot and a resulting refractive index gradient in the liquid. The gradient was probed with a laser probe beam of 635 nm, parallel to the sample. The deflection caused by the refractive index gradient is then proportionally linked to the absorption. A mechanical chopper was used to attenuate the pump beam, and the deflection of the probe beam was analysed by a quadrant detector (Thorlabs PDQ80A) and a SR830 lock-in amplifier.

The measurement was repeated for different pressures inside the liquid, ranging from ambient to 375 MPa. A more detailed description of the setup, experimental methods and sample preparation can be found in the supporting information (SI).

Results and discussion

The PDS setup is able to measure absorption spectra down to a magnitude of 10^{-4} with respect to the absorption on and above the bandgap. The PDS spectrum at different pressures is shown in Figure 6.6a. The bandgap shows a shift towards lower energies when the external pressure is increased from 0 to 300 MPa, which is still below the phase transition pressure. The trend is similar to what is reported before on MAPI samples when temperature was decreased [80, 91, 92], and consistent with linear UV/Vis measurements under pressure[31]. This trend remains untill 375 MPa, where the bandgap slightly blue-shifts with respect to the 300 MPa data (figure 5.1b). The red-shift from 0 to 300 MPa corresponds to the data found by Wang et al., but the blue-shift above 325 MPa is less extreme in the data we present here. Although it cannot be excluded that this is an effect of the different measurement method used (PDS in this work versus UV/Vis absorption by Wang et al.), it may be an indication that the phase change was only partially reached.

To analyse the nature of the bandgap, the absorption data was processed such that it can be visualised with a Tauc plot. The absorbance data in figure 5.1a is converted to an absorption coefficient according to

$$\alpha(\lambda) = \frac{A}{d} \ln 10 \tag{5.1}$$

with A being the absorbance and d the thickness of the MAPI layer. However, the thickness has been omitted in this work since it only scales the absorption spectrum and does not influence the overall shape. For distinguishing between a direct and indirect transition, the absolute absorption coefficient is not relevant. The linear regime in a Tauc plot can be used to identify either direct or indirect transitions, when $(\alpha h\nu)^{1/r}$ is plotted against $h\nu$, which is the photon energy. In this case r=1/2 for direct allowed transitions and r=2 for indirect allowed transitions, such that the linear regime can be fitted with the function

$$\alpha h\nu = A_r (h\nu - E_{\mathrm{BG}})^r \tag{5.2}$$

The fitting procedure was adapted from Kirchartz et al. [81]. The absorption spectrum can best be fitted with a model combining the indirect and direct transition. This is implemented by defining a photon energy (the direct bandgap, $E_{\mathrm{BG,d}}$) above which the direct transition dominates the absorption. Below the direct bandgap, the indirect transition model is used to fit the absorption data. At the energy level where the indirect model reaches direct bandgap, the absorption of the indirect model is kept constant and the direct transition model is added to this constant value:

$$\alpha h\nu = \begin{cases} A_{\mathrm{r,i}} (h\nu - E_{\mathrm{BG,i}})^2 & \text{for } E_{\mathrm{BG,i}} < h\nu < E_{\mathrm{BG,d}} \\ A_{\mathrm{r,i}} (E_{\mathrm{BG,d}} - E_{\mathrm{BG,i}})^2 & \\ + A_{\mathrm{r,d}} (h\nu - E_{\mathrm{BG,d}})^{1/2} & \text{for } h\nu > E_{\mathrm{BG,d}} \end{cases} \tag{5.3}$$

The indirect bandgap ($E_{\mathrm{BG,i}}$) is defined as the point where the linear model from equation 5.2 with $r = 2$ crosses the x-axis. In this work, we use this model to fit the PDS data over a range similar to the one used by Kirchartz et al.. The upper bound of the fitting domain was based on the data in Wang et al. [31], which shows absorbance data for various pressures accurately at the onset of the bandgap. The lower bound was chosen to be 1.53 eV, since the data in Wang et al. shows that the indirect model can only describe the absorption roughly above this value. The resulting parameters were found by varying the direct bandgap $E_{\mathrm{BG,d}}$, which defines the transition point between the indirect and direct model, and choosing the set of parameters that leads to the best fit, where we use the R^2 value as an in-

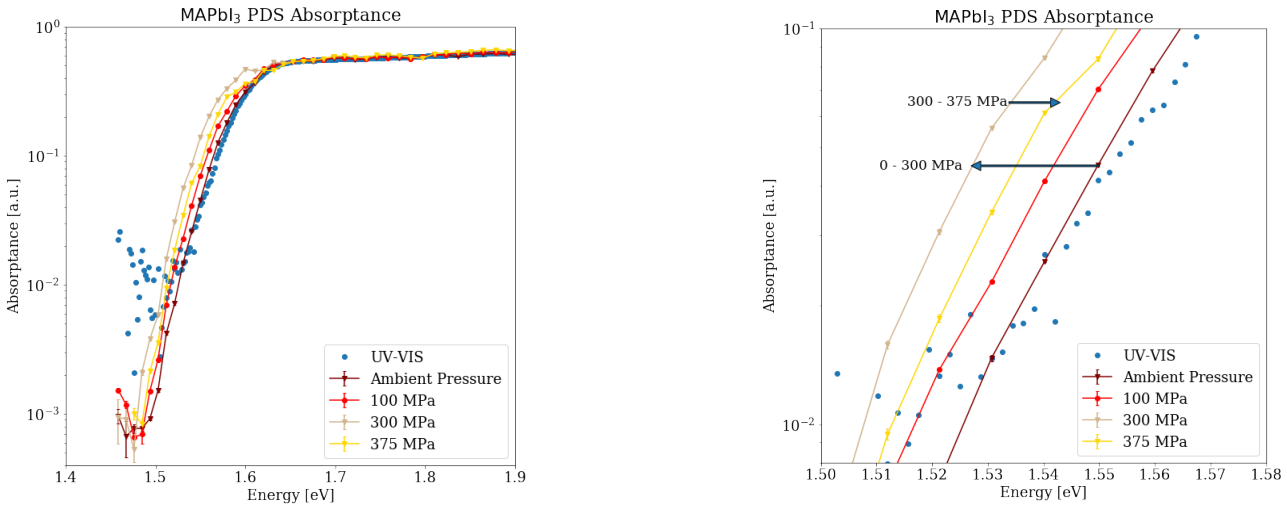

(a) (b)

Figure 5.1: (a) The overall spectrum of MAPI absorption, measured with PDS under various pressures. UV/Vis absorption data of MAPI at ambient pressure is also shown. This UV/Vis absorption data is measured with an integrating sphere, which cannot be combined with a pressure cell. In (b) a red-shift of the absorption data of roughly 30 meV is visible at an increase of 0-300 MPa, and a 10 meV blue-shift between 300 and 375 MPa

dicator for the goodness-of-fit. For the purpose of describing the rest of the absorption spectrum an Urbach tail was fitted in the region below the indirect bandgap down to where the measured data enters the noise region. With LB being the lower bound of the fitting domain and UB the upper bound, the fitting procedure can be summarized as follows:

1. Set $E_{\mathrm{BG,d}}$ such that $LB < E_{\mathrm{BG,d}} < UB$
2. Fit the indirect model in domain $[LB, E_{\mathrm{BG,d}}]$
3. Fit the direct model in domain $[E_{\mathrm{BG,d}}, UB]$
4. Calculate the R^2 of the fit in the full domain
5. Repeat 1-4 with a different $E_{\mathrm{BG,d}}$ in [LB, UB]
6. Choose the parameters with the highest R^2
7. Fit an Urbach tail below LB

The resulting Tauc plots and fitted according to the described procedure can be found in figure 5.2, for two different pressures (ambient and 375 MPa). It can be seen that both datasets are well-described by the combination of an indirect and a direct model, complemented with a model for the Urbach tail. The thick red line covers the spectrum from the onset of the bandgap down to the noise floor of the data. Before comparing quantified indicators such as the indirect bandgap, the direct bandgap and the difference between those (Δbandgap), it is already interesting to note that the direct fit covers a larger region of the data in the 375 MPa case with respect to the ambient case. The direct bandgap, indicated by the vertical part of the dashed green line close to the x-axis, lies at a lower energy level in the 375 MPa data but continues to higher photon energies because of the blue-shifted onset of the bandgap. This hints towards a more direct behaviour of the bandgap at 375 MPa than at ambient pressure. We note that the Tauc model assumes parabolic bands, and is hence only valid for energies close to the bandgap.

Finally, we compare the values of the indirect and direct bandgap that are extracted from the fitted models in the Tauc plots. Shown in figure 5.3 in the top row are the indirect and direct bandgap for various pressures. These bandgaps represent the values where the indirect and direct model equal zero. The Δbandgap shows the difference between the indirect and direct gap. In the bottom row, the R^2 of different models are shown. The indirect and direct fit here represent a standalone model, that means the indirect fit shows the R^2 of a model with only an indirect transition model and an Urbach tail.

No contribution of the direct model is involved.

We clearly notice a trend of the indirect bandgap red-shifting from 0 to 325 MPa. This trend stops at 375 MPa, similar to what is shown in figure 5.1b and described by Wang et al. The trend of the direct bandgap is less clear, but a significant red-shift can be distinguished for 300 and 375 MPa. As a results, the Δbandgap at 375 MPa has decreased by 10-20 meV with respect to the lower pressures. This is a strong indication that the indirect and direct bandgap move closer together due to the phase change at 325 MPa. However, it cannot be concluded that the bandgaps have completely merged and that only a direct bandgap remains. The R^2 values in the

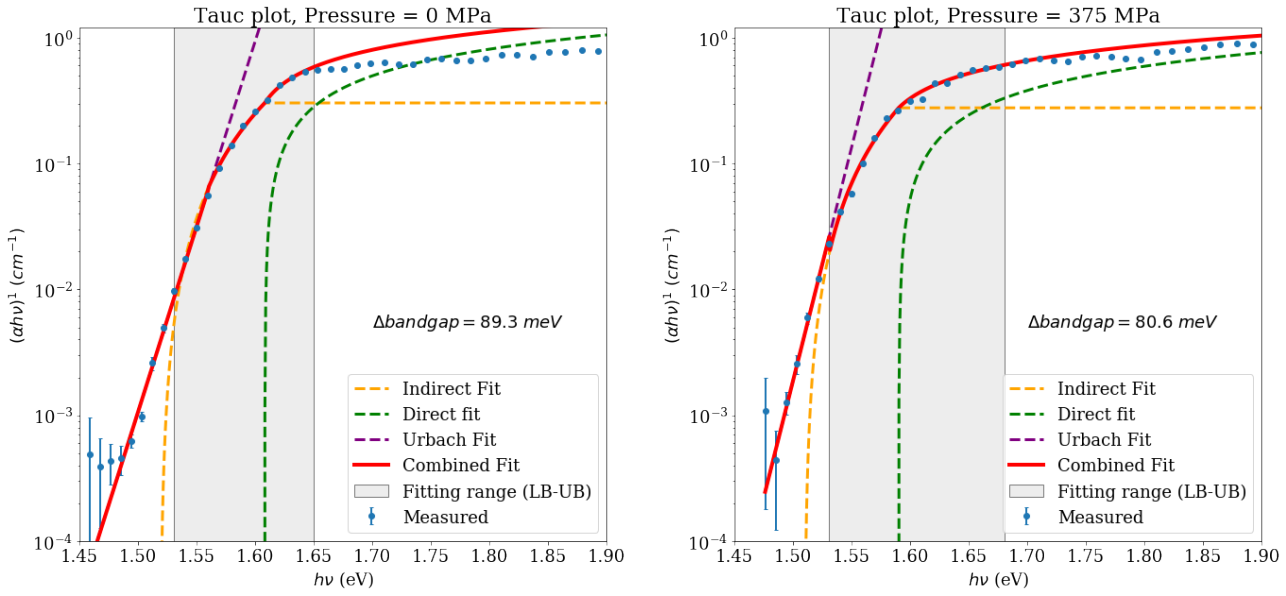

Figure 5.2: Tauc plots including fitted models, showing data extracted from ambient pressure (a) and from 375 MPa pressure (b). The red line shows the combination of direct, indirect and Urbach tail model. Δbandgap denotes the difference between the direct and indirect bandgap. The grey shaded area shows the fitting range of the indirect and direct bandgap model, bounded by LB and UB.

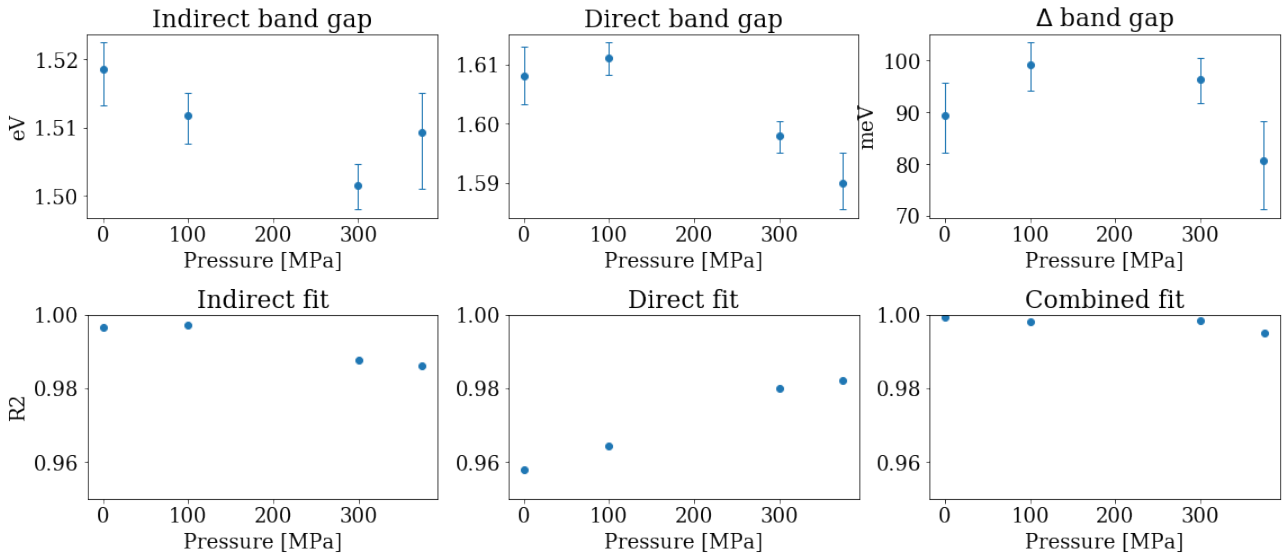

Figure 5.3: Top row: Comparing the indirect bandgap with the direct bandgap. Due to the counter-intuitive trend of the indirect bandgap above 325 MPa, the Δbandgap becomes significantly smaller in this case. Bottom row: Comparing the standalone models for different pressures. The indirect model suits better for the low pressure spectra, but the R^2 decreases for above 300 MPa spectra. The direct model however seems to improve with pressure for explaining the absorption spectra.

bottom row of figure 5.3 show a trend which is in agreement with the indication described above. The standalone indirect fit shows a decreasing ability to fit the data when pressure is increased, although there is no abrupt change visible between 300 and 375 MPa. The direct fit shows an opposite tendency, as it becomes more able to fit the data when pressure is increased. These trends hint toward a stronger contribution of the direct transition for absorption at higher pressures, whereas the indirect transition is more significant at ambient pressure. The combined fit R^2 should in this case not directly be compared to the standalone models, since it has an extra degree of freedom to properly fit the data which is not accounted for in the R^2 goodness of fit measure.

Conclusion

In this work, we have presented new empirical evidence on the direct-indirect behaviour of the bandgap of MAPI. With a PDS setup that is able to measure the below-bandgap absorption under hydrostatic pressure, we have shown a combined indirect-direct behaviour of the bandgap of MAPI. As reported before, when pressure was increased between 300 and 375 MPa, we observe a shift from a strong indirect contribution in the bandgap to a stronger direct contribution. However, the complete transition from an indirect bandgap to a direct bandgap could not be confirmed. Applying this behaviour on the structural dynamics of MAPI, it can be concluded that the indirect nature at ambient pressure is not exclusively the result of a static Rashba effect, as this would completely disappear in the centrosymmetric orthorhombic *Pnma* phase above 325 MPa. Since we do see a significant stronger contribution from the direct transition model at high pressures, it could mean that the indirect bandgap at ambient pressure is a result of combined dynamic and static Rashba splitting, of which only the static part is lost in the orthorhombic phase.

This letter aims to open up a new perspective for examining metal halide perovskites. Since there is still no consensus on the bandgap nature of these interesting materials, new evidence might be very useful to properly understand its exceptional behaviour. We notice that this work can pave the way for further research using sensitive absorption measurement techniques under pressure. Other materials, such as $CH_3NH_3PbBr_3$ (different halide) or replacing $CH_3NH_3^+$ with caesium are known to have different crystallic structures, with or without inversion symmetry, and may therefore show other behaviour when measured with the same protocols as described here. Characterizing these materials will inevitably contribute to the ongoing discussion on the bandgap nature of metal halide perovskites.

Acknowledgements

The writers acknowledge Loreta Muscarella for the fabrication of $CH_3NH_3PbI_3$ samples and Benjamin Daiber for his expertise on the optical setup, as well as other members of the Hybrid Solar Cells group at AMOLF for their valuable input and discussions.

Supplementary information

For supplemental information about the background of this project, experimental methods and extended results, please refer to my master thesis "Direct or Indirect?".

6

Results

The PDS setup was able to measure absorption spectra of $MAPbI_3$ with a high sensitivity. The setup was first proven to work by measuring a pentacene sample. After multiple iterations, the characteristic $MAPbI_3$ absorption spectra could be reproduced. To evaluate the performance of the setup, the absorption spectra under ambient pressure are compared to PDS absorption spectra of $MAPbI_3$ found in literature. Pressure dependent PDS spectra have been plotted against each other to visualize the general effect that pressure has on the absorption spectra. Tauc plots are shown including the regression analyses of the direct-indirect models. Key indicators of the models, the direct and indirect energy gaps, the difference between the gaps and the R^2 indicating the goodness-of-fits, are plotted as a function of pressure. Also, the Urbach energy is extracted from the fitted Urbach tail and plotted for various pressures. This is compared to the Urbach energy as a function of temperature, which is reported in literature.

6.1. Proof of concept: Pentacene

Before samples of $MAPbI_3$ were measured under various pressures, a proof of concept experiment was done to show that the setup was actually measuring absorption spectra. For this, a pentacene sample was used because it shows distinct, well-known absorption features at well-defined frequencies. Pentacene has an absorption spectrum with characteristic peaks, which can be easily recognised. It is shown in the comparison between figure 6.1a and 6.1b that the absorption spectrum measured with the PDS setup shows very similar results compared to a pentacene absorption spectrum found in literature [93]. This result was a good starting point that provided a basic indication of how well the setup was performing, and how much it needs to be improved. After pentacene, $MAPbI_3$ samples were used to generate absorption spectra and the setup was further improved based on these measurements.

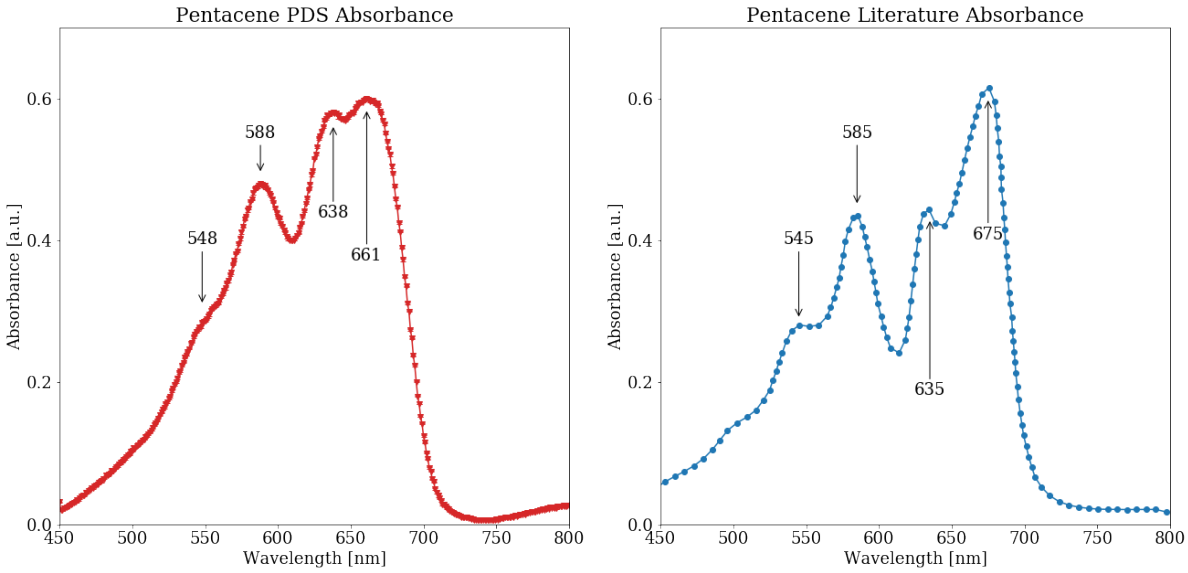

(a) PDS measurement

(b) Literature data

Figure 6.1: The first results of the PDS setup shown in (a): A pentacene absorption spectrum. Compared to figure (b), which contains data found in literature from Yang et al. [93], the shape of the spectrum seems to be similar in terms of absorption peak locations. This indicates that the setup was actually measuring absorption

The major flaws in the PDS data that are directly visible, are the sharpness of the peaks and the valleys of the absorption spectrum, and the fact that the absorption seems to go up above 750 nm whereas it should stay low in this regime according to the literature data. Since this measurement was the first one of the setup, it is not representative of the performance of the setup when $MAPbI_3$ samples were measured, because multiple improvements were implemented after the pentacene measurement was done.

6.2. UV/Vis absorption

The UV/Vis spectrometer was used to measure the absolute absorbance/absorptance of $MAPbI_3$ at (and above) the bandgap. The output of the spectrometer is absorbance data (A), which is different from what is measured with PDS. The data is therefore converted into absorptance (F_A), according to the relations in section 2.4. It can be seen in figure 6.2 that both the absorbance and the absorptance are of the same order of magnitude. A mistake is therefore easily overlooked. The data is not as sensitive as PDS data, which will be shown in the next section. However, this is not evident if UV/Vis data is plotted on a linear y-scale. When plotted in the same graph as PDS data, the y-scale is logarithmic and the improvement in sensitivity of the PDS measurement becomes clear.

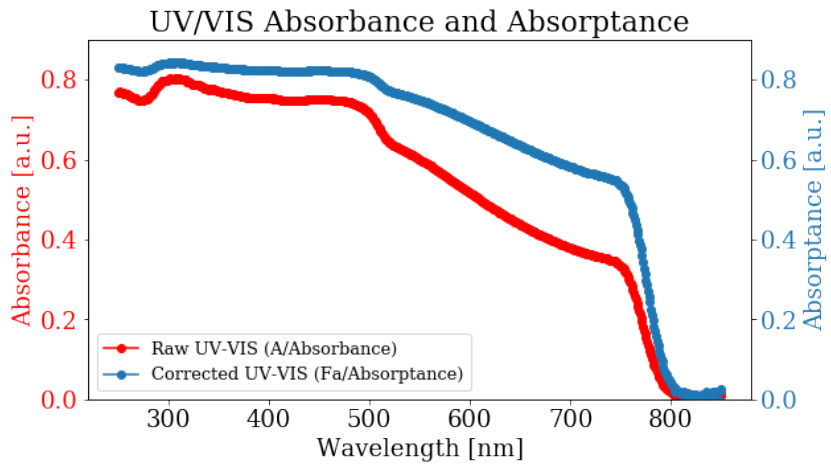

Figure 6.2: Both absorbance and absorptance of a single UV/Vis absorption spectrum are shown. They are in the same order of magnitude and therefore easily overlooked when the incorrect one is used for scaling

6.3. Performance compared to literature

As a way to quantify the performance of the PDS setup, the absorbance spectrum of $MAPbI_3$ under ambient pressure is plotted in the same graph as multiple datasets found in literature that have also used PDS to measure the absorbance of $MAPbI_3$. It can be seen in figure 6.3a that the setup from this work has a similar sensitivity to several other PDS setups. In figure 6.3b, a comparison between PDS absorptance and UV/Vis absorptance is plotted, showing a clear improvement in sensitivity with a PDS measurement over UV/Vis. It should be noted that the UV/Vis measurement was done inside an integrating sphere. Doing a UV/Vis measurement while pressure is applied on the sample cannot be done in combination with an integrating sphere. Therefore, under pressure, the effect of reflection is neglected and the sensitivity will be even lower.

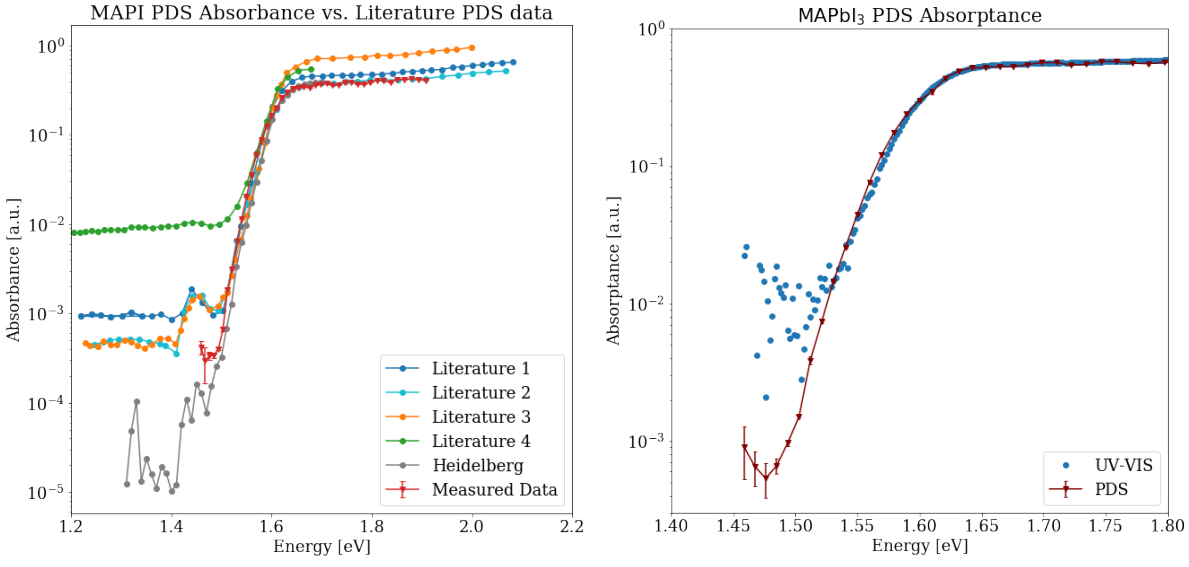

(a) (b)

Figure 6.3: PDS absorbance spectrum (this work in red) compared to spectra found in literature. Figure (a) is generated from a measurement with a lock-in time constant of 300 seconds. MAPI = $MAPbI_3$. Figure (b) compares a PDS measurement of $MAPbI_3$ directly with a measurement with UV/Vis spectroscopy, to show the improvent in sensitivity that PDS has over UV/Vis. Literature 1: [66] Literature 2: [94] Literature 3: [65], Literature 4: [95], Heidelberg: [56].

The setup that was recently build at the University of Heidelberg [56], still reaches lower absorbance measurements. The used time constant in figure a is 30 seconds, but 1000 seconds in the low absorption regions. In graph b, a shorter time constant is used (100 seconds), which results in less sensitivity.

It is remarkable that a small local peak around 1.45 eV (855 nm) appears in multiple literature datasets. Also in the PDS measurements of this work, the local peak at 855 nm showed up. It is considered to be an artefact of PDS when a xenon lamp is used. Xenon light has significantly lower intensity at the wavelength of this peak. Looking more closely at the intensity of the pump beam, it can be seen that the absorbance peak at 855 nm overlaps with a valley of pump intensity (figure 6.4a). Because the signal is corrected for the intensity (divided by intensity), the noise regime will be fluctuating as a result of the intensity correction. The standard deviation of the phase gives an indication of the uncertainty of the data, as can be seen in figure 6.4b that the data becomes more uncertain in the low absorption region.

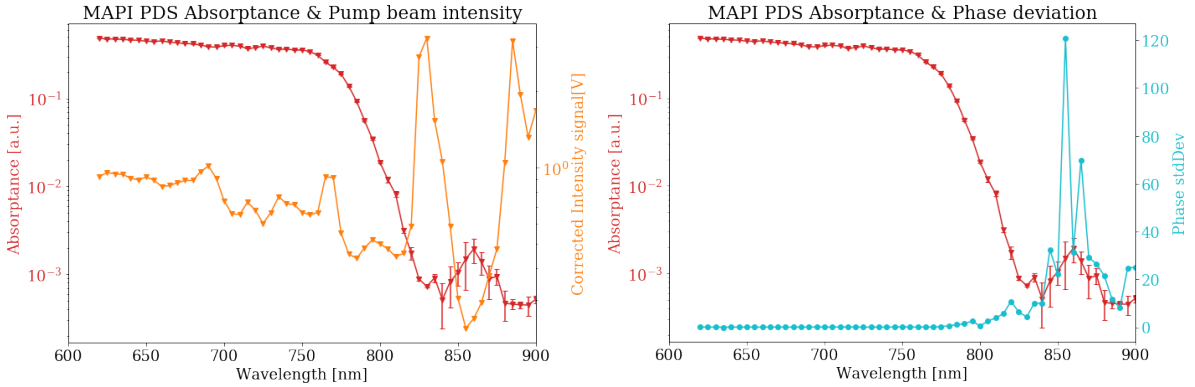

(a) (b)

Figure 6.4: Figure (a) shows the absorption and pump beam intensity in one graph. Because the PDS data is corrected for the intensity, there should not be a correlation between the two. When the noise floor is reached, the correlation is unavoidable. Figure (b) shows the standard deviation of the phase, as an indication of the uncertainty.

6.4. PLQY measurement & correction

Using the equation described in section 2.5, PDS data can be corrected for the PLQY effect. The PLQY was measured and assumed to be constant over the spectrum. However, the degradation of a perovskite sample may influence the PLQY. New samples generally have a higher PLQY than older samples, even when they are stored correctly. Looking at figure 6.5, we can see that a fresh sample of $MAPbI_3$ has an increase in absorbance above the bandgap with respect to a UV/Vis measured absorbance spectrum. This can be corrected when a high PLQY of 30% is assumed. It could not be completely confirmed if this high assumed PLQY was actually correct. To measure the PLQY, a sample had to be placed inside an integrating sphere. It is therefore taken out of the protected environment of a glovebox, and degradation will quickly affect the PLQY performance. The measurement showed a PLQY of lower than 1%. For PDS measurements, the sample was placed inside degassed FC-72 liquid in a pressure cell, free from oxygen and water. Degradation is therefore less of an issue, and the PLQY is probably higher than what was measured with the PLQY setup.

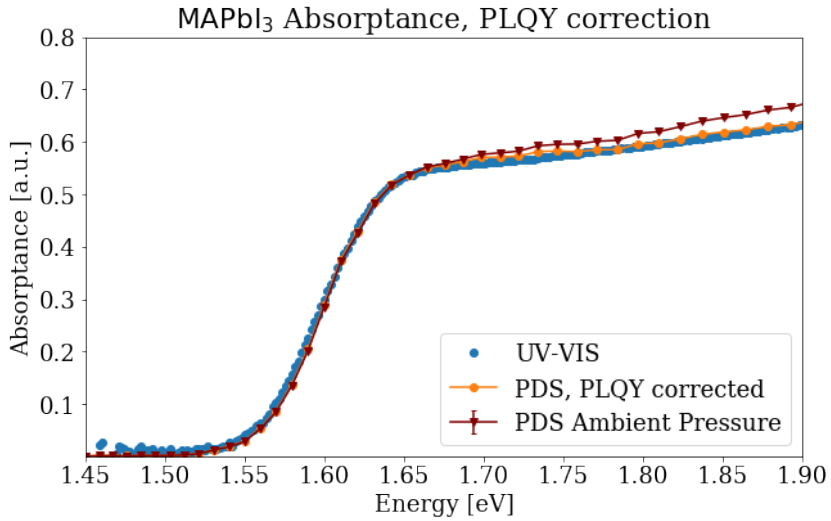

Figure 6.5: The absorbance spectra measured with UV/Vis (blue) and PDS (red). When a PLQY of 30% is assumed, the corrected PDS spectrum (orange) overlaps with the UV/Vis data.

6.5. Pressure dependent plots

PDS absorption spectra under pressure are unprecedented at the time this work was done. Comparison with literature data is therefore not possible. Figure 6.6a shows the spectra of a single $MAPbI_3$ sample, measured at pressures ranging from Ambient pressure to 375 MPa. The spectra are scaled to overlap with the UV/Vis spectrum above the bandgap. In figure 6.6b, a clear trend is visible. With pressure increasing to 300 MPa, the slopes shifts towards lower energy levels. This trend is reversed for the 375 MPa spectrum, that is at slightly higher energy levels than the 300 MPa slope. The trend is similar to what was published by Wang et al. [31],

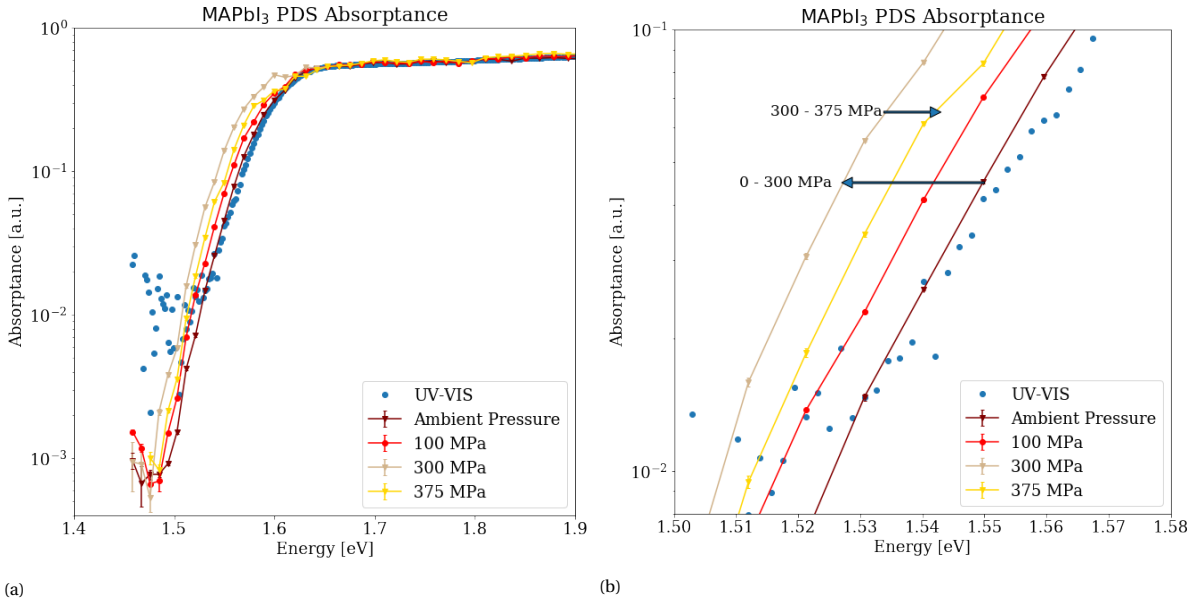

(a) (b)

Figure 6.6: Increasing pressures results in a shift of the absorption slope. (a) shows the overall spectrum, overlapping with the UV/Vis data above the bandgap. In (b) a redshift of roughly 30 meV is visible at an increase of 0-300 MPa, and a 10 meV blueshift between 300 and 375 MPa

where UV/Vis absorption and photoluminescence measurements (under pressure) were used to show a shift of the bandgap to lower energies for increasing pressures from 0 to 325 MPa. Even the reported shift after 325 MPa is similar to what was found in this work, although the PDS measurements show a less severe shift to higher energies between 300 and 375 MPa.

6.6. Tauc plots

The measured absorption spectra at various pressres are displayed in Tauc plots. Models for an indirect transition and a direct transition, as well as a model for the Urbach tail, are used to make a combined fit of the data. The data is only fitted in the regime that is below the bandgap and at the onset. Because the bandgap slightly moves when pressure changes, the energy boundary (upper limit) of the fit changes as well. The upper limits of the range is derived from absorbance data in Wang et al. [31]:

- 0 MPa: 1.65 eV
- 100 MPa: 1.63 eV
- 300 MPa: 1.615 eV
- 375 MPa: 1.68 eV

Figure 6.7 shows the three fitted models on one dataset, in this case the absorption spectrum of $MAPbI_3$ at ambient pressure. The blue shaded areas show the confidence intervals of the fits at 95%. The width of these confidence intervals are strongly influenced by the amount of data points used for the fit. The algorithm chooses the best value for the direct bandgap, where the direct transition model takes over from the indirect transition model. From this energy level, the indirect fit is set to a constant, as can be seen in the left figure where the indirect fit suddenly becomes constant (horizontal). Similarly, the absorption data of $MAPbI_3$ at 375 MPa is fitted with the three models. This is plotted in figure 6.8.

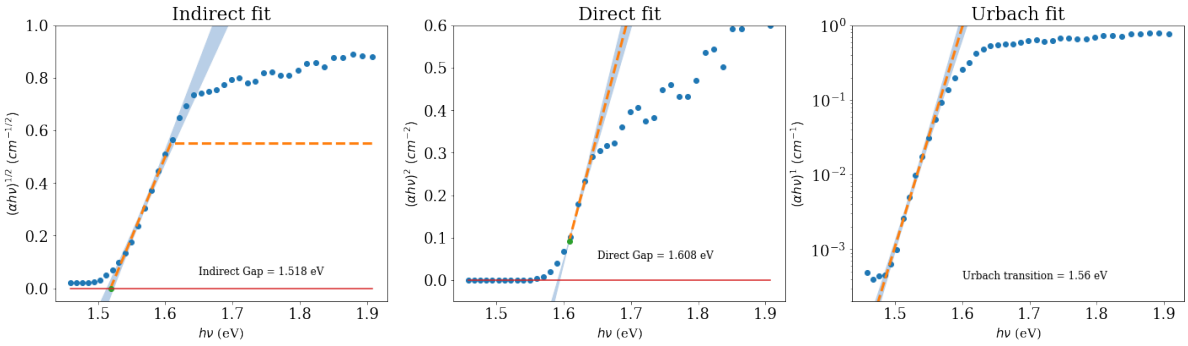

Figure 6.7: An absorption dataset of $MAPbI_3$ at ambient pressure that is fitted with and indirect, direct and Urbach tail model. The difference between the models can be seen at the y-axis, where r is either 1/2, 2 for direct and indirect respectively. The blue shaded region shows the confidence interval of the fits (95% confidence)

The fitted models of the direct bandgap, indirect bandgap and Urbach tail are shown in figure 6.9. These figures show a combination of the models, where the combined fit is a result of adding the indirect to the direct fit, as explained in section 4.8 according to the procedure as published by Kirchartz et al.[81]. The measured data points are shown in blue, including their statistical errors. The indirect transition model is indicated by the yellow dashed line. The green dashed line represents the direct transition model's contribution. This is added to the indirect model at a certain point where the direct bandgap is calculated to be. From that point, the indirect model is kept constant (as can be seen where the yellow dashed line becomes horizontal). The

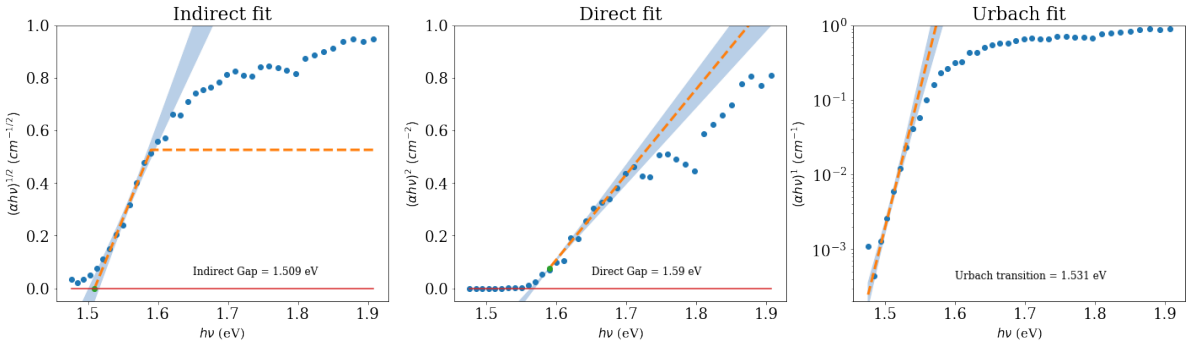

Figure 6.8: An absorption dataset of $MAPbI_3$ at 375 MPa that is fitted with and indirect, direct and Urbach tail model. The difference between the graphs can be seen at the y-axis, where r is either 1/2, 2 for direct and indirect respectively. The blue shaded region shows the confidence interval of the fits (95% confidence)

direct model is then added to the constant value of the indirect model to form the combined fit (red line). The fitted Urbach tail is shown as a purple dashed line and fits the tail that cannot be covered by the indirect fit.

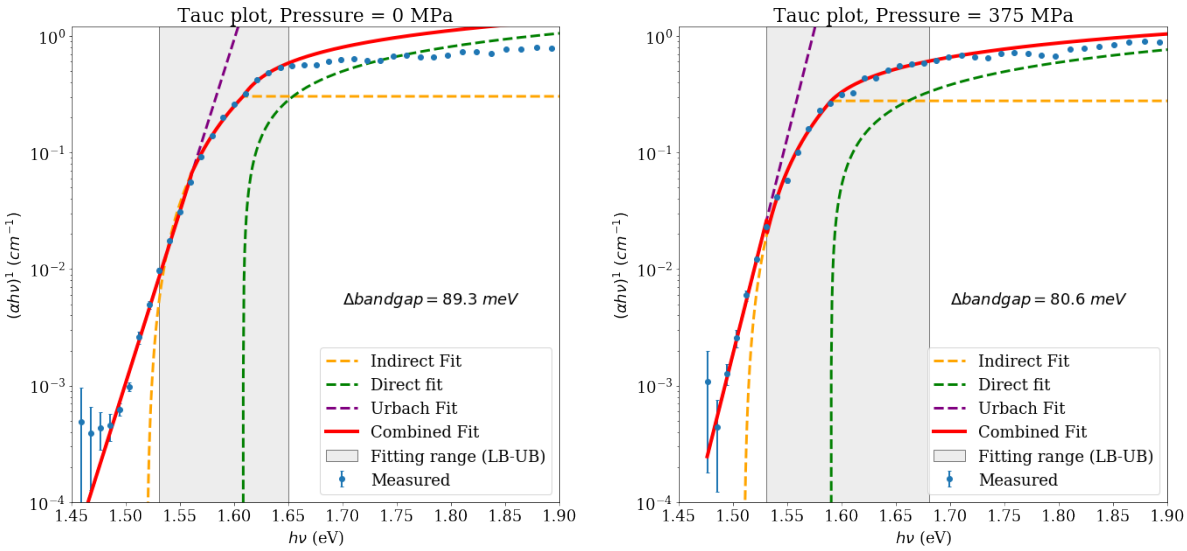

(a) 0 MPa, fitting range [1.53 1.65]

(b) 375 MPa, fitting range [1.53 1.68]

Figure 6.9: Tauc plots including fitted models, showing data extracted from ambient pressure (a) and from 375 MPa pressure (b). The red line shows the combination of direct, indirect and Urbach tail model. Δbandgap denotes the difference between the direct and indirect bandgap. The grey shaded area shows the range (from the Lower Bound (LB) to the Upper Bound (UB)) that is used for fitting the indirect and direct bandgap model. Below LB, the Urbach tail fit takes over.

From the fitted models in the Tauc plots, the energy of the direct and indirect models can be extracted, leading to an energy difference Δbandgap. These values are plotted in figure 6.10 for different pressures. The confidence intervals from the regression fit are plotted as error bars. The indirect bandgap is decreasing in energy when the pressure is increased from 0 to 300 MPa, but the trend stops after 300 MPa. This seems to be in accordance with the earlier reported trend in figure 6.6a, where the absorption spectrum shifts to lower energies from 0 to 300 MPa but returns to a higher energy at 375 MPa. The direct bandgap shows a similar trend, but there is no clear distinction between 375 MPa and lower pressures. As a result, the Δbandgap between the direct and indirect gaps is significantly lower at 375 MPa, indicating that the bandgaps have moved closer together.

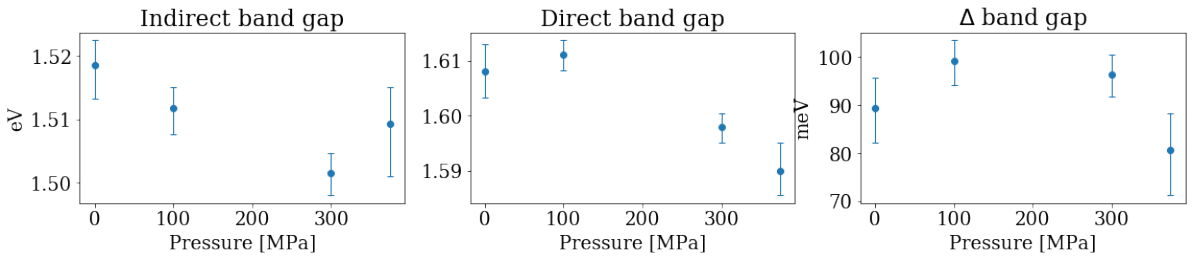

Figure 6.10: The energy levels of the bandgaps according to the different models. All three graphs are extracted from the combined fit. In the combined fit, both the indirect part and the direct part result in a bandgap when the regression is extrapolated to the x-axis crossing. The Δbandgap is the difference between the two model's energy bandgap. Error bars denote the 95% confidence interval

To determine if the absorption spectrum can be explained with only an indirect or direct bandgap in combination with an Urbach tail, the data has also been fitted independently. This means that it was tried to explain the absorption spectra with only a direct, or only an indirect transition model.The R^2 goodness-of-fit in figure 6.11 is shown as an indication of how well the different models perform. The Tauc plots have been fitted with three scenarios: (1) using a model representing an indirect transition, (2) using a model representing a direct fit and (3) using a model combining a direct and an indirect fit. The aim was to show the difference in goodness-of-fit for the three scenarios, which gives an indication of what scenario can explain the data best.

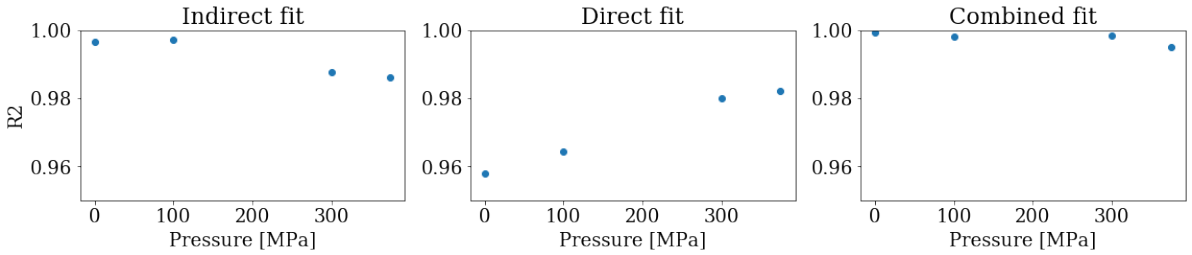

Figure 6.11: Contrary to figure 6.10, the indirect and direct fit here represent a non-combined model in the left and middle figure. The R^2 is shown to compare three scenarios: [1, left] only an indirect model is used for the fit, [2, middle] only a direct model or [3, right] a combined model. The indirect model suits better for the low pressure spectra, but the R^2 decreases for above 300 MPa spectra. The direct model however seems to improve with pressure for explaining the absorption spectra. The combined fit performs best in all cases but the R^2 does not take into account a penalty for the additional fitting parameters.

Interestingly, the indirect model shows a very good performance of fitting the spectrum at lower pressures, in contrast to the direct model. The combination of the indirect and direct model shows hardly any improvement with respect to the indirect model at lower pressures. At high pressures however, the indirect model has a lower R^2, whereas the direct model has an increased R^2, now fairly similar to the indirect model. This indicates that a combination of the two models should be used to explain the absorption spectrum.

6.7. Urbach Parameter

Besides the indirect and direct model, the Urbach tail was fitted to the data in order to explain the exponential tail in the far-below bandgap regime. The interesting characteristic of the Urbach tail is the Urbach energy E_0, or Urbach parameter, as described in section 2.2.6. The Urbach energy indicates the steepness of the Urbach tail, when the absorption is plotted on a logarithmic y-axis. A smaller Urbach parameter is the result of less disorder in the crystal lattice, leading to a steeper tail.

In figure 6.12(b), data published by Senanayak et al. [96] shows that the Urbach parameter for $MAPbI_3$ decreases when temperature is decreased. Due to a lack of datapoints, the fitted regression in figure 6.12 (a) has large confidence intervals. However, the Urbach energy at 375 MPa is significantly lower than at ambient pressure, indicating that there is a similar trend for increasing pressure as there is with decreasing temperature. An Urbach energy of $MAPbI_3$ at ambient pressure and temperature was earlier found to be 15 meV [66, 97].

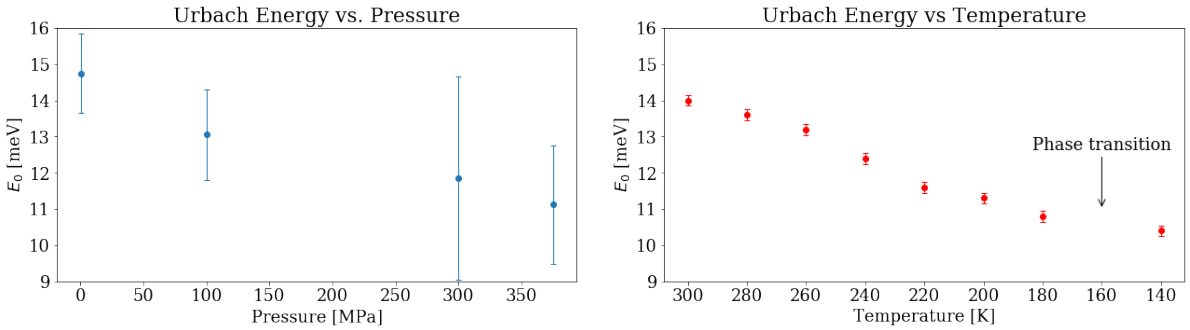

Figure 6.12: Comparison between the Urbach energy trend as a function of pressure in (a), with Urbach energy as a function of temperature. The latter was reported by Senanayak et al. [96]

7

Conclusion

This work describes the first Photothermal Deflection Spectroscopy (PDS) setup that can successfully measure absorption under various pressures up to 400 MPa. The sensitivity of the setup is comparable to other PDS setups described in literature, being able to measure 4 orders of magnitude smaller absorption with respect to above-bandgap absorption. This is a significant improvement relative to absorption measurements using UV/Vis transmission spectroscopy, which has a very limited sensitivity when samples are subject to hydrostatic pressure. Although the setup is sensitive to proper operation and alignment, it has proven to have a good reproducibility.

The measured absorption spectra under pressure show a clear trend. Although the shift is not easily quantified, The slope of the sub-bandgap absorption seems to move towards lower energy levels while the pressure is increased from 0 to 300 MPa. Between 300 MPa and 375 MPa, the trend stops. Contrary to the trend from 0 - 300 MPa, the absorption slope and the bandgap of $MAPbI_3$ at 375 MPa hydrostatic pressure is positioned at a slightly higher energy than the slope at 300 MPa.

When the absorption data is fitted, a different trend for the direct fitted model and the indirect fitted model can be distinguished. While the fits are build up as a combination of a direct and indirect fit, the indirect part shows a shift towards a lower energy level from 0 to 300 MPa, but stops between 300 and 375 MPa. This trend is less visible for the direct gap transition model, which does show a decrease above 300 MPa. As a result, the difference between the indirect and direct bandgap in the combined fits is significantly lower at 375 Mpa.

Based on earlier research, the bandgap was expected to show properties of an indirect transition below 325 MPa and behaviour of a direct transition above 325 MPa. Looking at the R^2 of the fits, it can be concluded that the absorption slope can be well explained with an indirect transition model. At low pressures, the indirect model seems more suitable than the direct model, while the combination of both hardly shows

an improved result. However, it cannot be confirmed that contribution of the indirect model disappears at 375 MPa. The indirect model does show a decreasing ability to fit the absorption slope at high pressure (> 300 MPa), while the direct model seems to play a more important role at these pressures. Especially above 300 MPa, a combination of both models seems to explain the absorption curve the best.

Based on this work, it is therefore concluded that the absorption behaviour of $MAPbI_3$ at pressures up to 300 MPa can best be explained by an indirect transition model, with little contribution from a direct transition model. The direct transition model can only explain a small part of the absorption slope at the onset of the curve, which results in a Δbandgap of 89 - 100 meV. Above 300 MPa, the contribution from a direct model is more important to explain the part below the onset of the absorption spectrum, while the difference between the bandgap levels of the models has decreased to roughly 80 meV.

8

Discussion and Reflection

In September 2019, I started at AMOLF in the Hybrid Solar Cells group. The purpose of the project was to design and build a PDS Setup that is able to perform measurements while keeping a sample under high hydrostatic pressure, performing absorption measurements on $MAPbI_3$ and analysing the data in order to contribute to the ongoing discussion on the bandgap of the semiconductor. I performed unprecedented measurements and found new evidence, enabling scientists to look at $MAPbI_3$ and other perovskites from a new perspective. In this chapter, I will discuss the scientific content of the thesis and its conclusions, and provide recommendations on further research to continue on what I found during this project. Also, I will evaluate my personal experiences on conducting academic research.

8.1. Discussion on the scientific content

The setup showed that is was able to perform absorption measurements with a comparable sensitivity to PDS setups found in academic literature. However, PDS can theoretically measure absorption down to a magnitude of 10^{-5}, which is still 1-2 orders of magnitude more sensitive than what was reached in this work. Also, a better spectral resolution than 5-7 nm also lies within the ability of PDS. Improving these parameters can still result in higher quality absorption data. The sensitivity of the data seemed to be enough for fitting the direct and indirect transition models, but the lack of a sufficient amount of datapoints did lead to larger confidence intervals and error bars. The value of the presented bandgap energies and corresponding Δbandgap lies in the trend that is visible when pressure changes, rather than the absolute energy levels.

Coming back to the research question of the project, the expected phase change, with corresponding transition from an indirect bandgap to a direct bandgap, could not be confirmed. However, the data shows a clear

indication of an indirect bandgap, obtaining good results by fitting the data with an indirect model. A direct transition cannot be fully rejected at ambient pressure, since adding a direct model to the total fit shows a slight improvement in explaining the model. At 375 MPa, the addition of the direct transition model to the fit has a greater value than at low pressure. It seems that a direct bandgap is present, but it does not completely replace the indirect bandgap.

The question arises how this can be related to the crystal structure of $MAPbI_3$. If the indirect bandgap is completely the result of a static Rashba effect, due to a non-centrosymmetric system at ambient pressure, we would expect to see this effect disappear once the orthorhombic centrosymmetric phase is present. An explanation could be that the indirect properties at higher pressure is the result of a dynamic Rashba effect, caused by electrostatic instabilities of the MA cation, locally breaking the inversion symmetry. A static Rashba effect could still be present in the tetragonal *I4cm* or *P4mm* phase, where the structural indirect properties overshadow the the dynamic Rashba effects.

Besides repeating the measurement and analysis on more $MAPbI_3$ samples, a good next step is to measure other samples as well. Metal halide perovskites with other elements, such as Br or Cl as halide, have similar crystal structures, but different space groups and inversion symmetries. For example, $MAPbBr_3$ is expected to be centrosymmetric in the tetragonal phase, but non-centrosymmetric in the orthogonal phase (although its space groups are still debated [35]). This is exactly the opposite as what the $MAPbI_3$ in this work was predicted to be. A static, bulk Rashba effect should therefore have an opposite behaviour. However, the effects of a dynamic Rashba effect, induced by MA cation rotations and instabilities, would still be similar for both materials ($MAPbI_3$ and $MAPbBr_3$). Replacing the MA^+ by other cations, such as Cs^+ (caesium) or FA^+ (formamidinium), may therefore show interesting differences in the shape of the absorption spectrum. If the indirect behaviour is associated with dynamic Rashba splitting, the effect could be strongly reduced when more stable cations are in place.

Another parameter that should be critically looked at is the reliability of the PDS setup. The technique is at steady state ambient conditions extremely sensitive to proper alignment and outside disturbances. Higher pressure even creates a more difficult environment. The liquid FC-72 where the samples were placed in showed a decrease of transparency when the pressure was increased, and therefore a sharp signal reduction. One of the most difficult things in operating the setup was keeping a constant pressure in the cell during the measurement. While a single measurement could take a full day (without the possibility to interrupt or pause), The pressure in the cell was impossible to keep the same level throughout the day. Especially when the pressure was set to 400 MPa, the leakage was sometimes as much as 5 MPa per 15 minutes. For that reason, the manual pump was used during a measurement to keep the pressure at the same level. Although this could be done without touching the optical table, it was still an unwanted outside interference that may have influenced the measurements.

Multiple issues limiting the setups performance can be dealt with by increasing the signal to noise ratio. A better S/N ratio can be used to increase the sensitivity, the spectral resolution (by exchanging intensity for slit width of the monochromator), or reduce the time constant on the lock-in amplifier, leading to shorter measurement times. The latter is preferable because there is a larger pressure drop with longer measurement

times. Another way to tackle the pressure leakage is by servicing the pressure cell, such as changing the rubber seals and tube connectors. Ideally, an active pressure generator could control the pressure inside the cell in order the keep the pressure constant over the complete time of a measurement.

There are two additions overlooked in this work that could readily improve the performance of the setup. Firstly, it should be investigated if adding a lens *inside* the pressure cell (submerged in the liquid) is possible, to improve the pump beam focusing. In this way, the last lens would be closer to the sample and is not limited by the numerical aperture of the pressure cell itself. The sample holder has an circular aperture of 9 mm, would could fit a Thorlabs lens with a focal distance of 12 mm. The resulting NA would be 0.375, which is 1.5 times higher than the NA of the focusing lens used in the current setup.

Secondly, the probe laser intensity is not checked, nor is it corrected for. As explained in section 3.1, the signal of the output of the quadrant sensor scales with the intensity that hits the sensor. A fluctuation in the intensity of the laser will therefore affect the amplitude of the signal. It is not checked if the laser intensity changes over time. Noisiness may not be the greatest issue, if it has a constant mean. The specifications of the laser unfortunately suggest that there is a possible drift of 0.1 dB over a 24 hour term. The graphical user interface of the included software shows the normalized laser position, corrected for this intensity. The analog output signal (X_{diff}) however, is *not* normalized. There is another analog output (SUM) that contains a value of the total intensity that hits the sensor. This should be used to normalize the signal, preferably before it enters the lock-in amplifier. Besides counteracting the intensity drift, the correction before the lock-in amplifier can lead to a cleaner, less noisy signal at the input.

8.2. Reflection on personal experiences

One year ago, before I contacted AMOLF to ask about available Master projects, I decided that I wanted to specialise myself more in the field of sustainable technologies. Although the connection between my study, Precision and Microsystems Engineering, and sustainable technology might seem obvious, it was not easy to find a graduation project that would both fit my interests and substantially match my master courses. I was happy to find out that with AMOLF, The Netherlands has a leading institute in the field of photovoltaic research.

The fact that I was able to contribute, to some extent, to the search for better solar cells was an important drive for me. Besides believing that my own work could make a difference in the field, it also helped that I was surrounded by others that have a similar ambition. I felt encouraged by coworkers in the group and at AMOLF to contribute to the science of perovskites. It didn't take long before I felt that I was part of an academic society, including the duties of a scientist. What contributed to this effect was the stimulation of sharing knowledge at AMOLF. Besides weekly meetings, paper presentation and project updates, we attended colloquiums from speakers within and outside of AMOLF twice a week, saw PhD defenses and went to conferences such as Physics@Veldhoven (until Covid-19 interfered with these gatherings).

During my time at AMOLF, I felt that I was able to truly become the owner of my project, which includes

making decisions and being accountable for them. While Bruno and Eline laid out the general scope of the project, I was given the freedom to plan my own work towards a goal, making my own designs and deciding what resources to use for this. When I started, my approach was to execute a set of predetermined tasks. Further down the project, I learned to see the steps as part of a greater goal, which allowed me to make decisions based on the priority of the tasks. It also forced me to make necessary tough decisions whenever a certain approach was not working.

Formulating milestones during the year helped to break up the project in smaller parts, and work towards more achievable goals. Especially because I started with an empty lab, it was useful to have in mind what I could reach until the end of a month or period. Every time a certain milestone was reached (e.g. having the probe laser deflect for the first time due to absorption, measuring absorption at a single wavelength, making an absorption graph of pentacene etc.), it gave me an extra drive to work towards the next goal. As with most projects, some parts did not go as planned, which left me stuck with a problem that I was not able to solve. Especially in January/February, I was able to see a deflection of the laser due to pump light being absorbed, but I couldn't get the lock-in amplifier to measure a signal when the pump light was set to a single wavelength. By trying over and over again to achieve a better focus of the pump beam, I didn't realise that the problem was actually within signal processing of the lock-in amplifier. Normally, I prefer to solve issues like this by myself, but here I learned that discussing it with others at AMOLF was much more time-efficient. Only by explaining my troubles to colleagues, I already realised that I was looking in the wrong direction.

Being stuck unexpectedly was obviously interfering with the planning. Although there was room for slack in the overall schedule, further in the project I had to admit that it was going to be tight to finish everything in time. It was probably the hardest part of the project where I was unsure if it would be possible to build the setup within the limited time, resources and my own qualifications. Although sometimes it can be a good result to prove that something is not possible, it is certainly not as satisfying as finishing the work according to plan. As a result, I would sometimes use too much of my time for things that were not crucial for the project. This led to a very tight schedule in the final months. Especially at the end, the extra gained knowledge on the matter opened up new insights and possible improvements, which would only extend the project further. It was hard to draw the line and leave unfinished work as recommendations for someone else to pickup.

A year at AMOLF has been a great addition to my journey as a student, both scientifically and personally. I feel proud to have made an unprecedented PDS setup that can truly contribute to the mysteries of perovskite solar cells, and I am happy to have gained so much extra knowledge on physics of photovoltaics. Just as important was academic environment at AMOLF. Being surrounded by scientists encouraged me to make the best out of my own work. Sharing troubles of my own research and helping each other out was always promoted. I can safely say that this thesis would not have been possible without the proactive and supporting culture at AMOLF. On the other hand, having a critical attitude towards other research was cheered as well. Attending colloquiums and presentations helped me to see that sharing a (constructive) opinion on someone's work can be progressive for the presenter, but it also improved my own ability to judge scientific publications.

Contentwise, I can only hope that my work will be a valuable addition in the ongoing search for better perovskites. At the start, I was overwhelmed by the promising stories and publications that predicted perovskite

solar cells to be part of the next generation of photovoltaics. Every year, new climate reports are published that show the growing urge to create a sustainable, non-carbon dependent energy supply. Consequently there is an increasing pressure to develop better solar cells that can effectively cover a great deal of our energy demand. I do believe that perovskite solar cells are going to be part of this future, although I am uncertain in what composition or shape it will be. Nonetheless, when in 10 years time perovskite solar cells are installed on my roof, I will feel at least a little proud.

A

Schedule and Timeline

A.1. Project schedule and milestones

Figure A.1 shows the timeline of the project, divided in different parts: It consists of a literature survey, development of the new setup, performing experiments and analyzing results, comparing the results with literature and writing a thesis on the project. The complete project will have a duration of roughly 10 months. During the project, several milestones have been planned that will indicate the progress that has been made.

Milestone 1: Literature study:
A complete literature study has been performed which resulted in a clear description of the present knowledge of the subject, but above all, it shows what is currently unknown. In my case, the literature study shows the discussion on the band gap structure of metal halide perovskites and the research that has been performed so far. A research question is proposed and a methodology explained that should lead to new knowledge on the nature of the electronic band gap of metal halide perovskites. The results of the study are described in the literature report [15].

Milestone 2: Show deflection:
The working principle of the setup is confirmed by showing deflection of the laser probe beam when a sample is excited by pump beam monochromatic light. The sample does not have to be $MAPbI_3$ yet. The deflection of the probe beam should either be visible with the naked eye, or on the sensor in such a way that the spot travels over the full width of the sensor area.

Milestone 3: Test system and set-up:
At this milestone, the experimental set up should be able to work so it can perform measurements. It consists of the following working components:

- A light source that emits monochromatic light
- Mirrors and lenses that focus the light on the sample
- Samples can be placed inside a pressure cell
- A photodetector measures the intensity after a beam splitter has split the pump beam
- A laser (probe) beam is directed perpendicular to the light beam, parallel to the sample surface
- The deflection of the laser beam is measured by a position sensor
- The recorded data of the position sensor and photodetector can be stored on a pc, including the wavelength, intensity and time stamps.

The following criteria should be confirmed:

- The pressure in the pressure cell can reach 400 MPa (steady state)
- Relative light intensity changes on the light source result in the same relative change in the measured data (linear relation)
- The intensity can be measured and the response is proportional to the beam intensity. The absolute intensity does not need to be calculated
- The lock-in amplifier is able to read the measurement at a frequency of at least 20 Hz. Modulating the light source results in a measured deflection of the laser with the same frequency and is picked up by the lock-in amplifier.
- The lock-in amplifier provides a stable (locked) signal for absorption that has a magnitude of 10^{-4} smaller than the above band gap absorption of $MAPbI_3$

Milestone 4: Results complete:
Enough data has been collected to show different absorption spectra under various pressures, or similar ones of the spectra do not change under pressure.

- The absorption spectrum of $MAPbI_3$ has been measured for the following wavelength range: 650nm - 900nm
- $MAPbI_3$ samples have been measured under pressures up till 400 MPa, with more than one measurement at different pressures above 325 MPa, and more than one measurement at 0 MPa.

Milestone 5: Finish report:
The project is fully described in a Master thesis report that has adequate academic quality. It should at least consist of a literature part that has led to the start of the research project, a full description of the development of the setup, an explanation of the experimental procedures in such a way that it can be easily reproduced and an analysis of the results, which should lead to a conclusion on the research. The project will be critically reflected on in the discussion part.

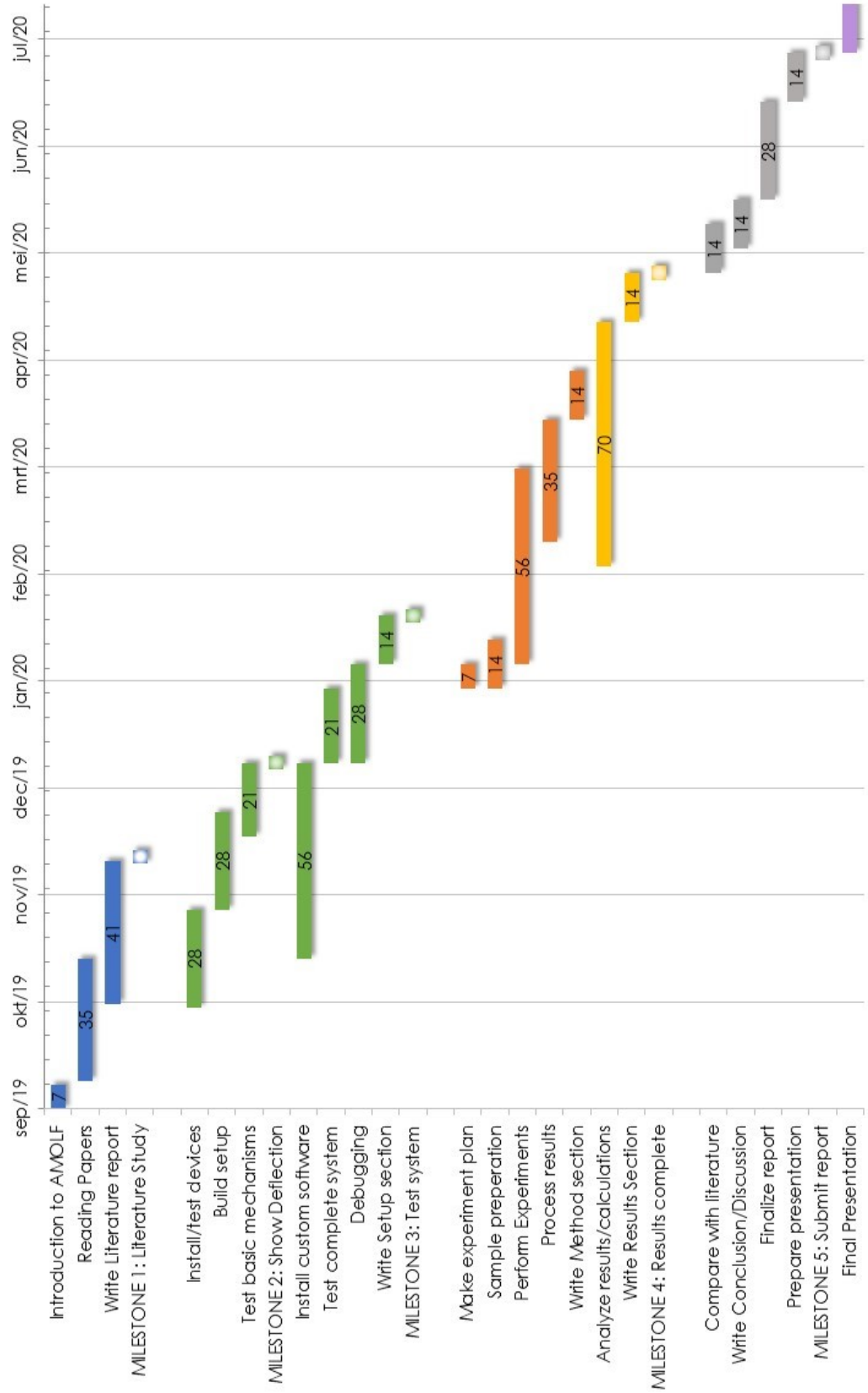

Figure A.1: The timetable of the complete project

B

Extra images

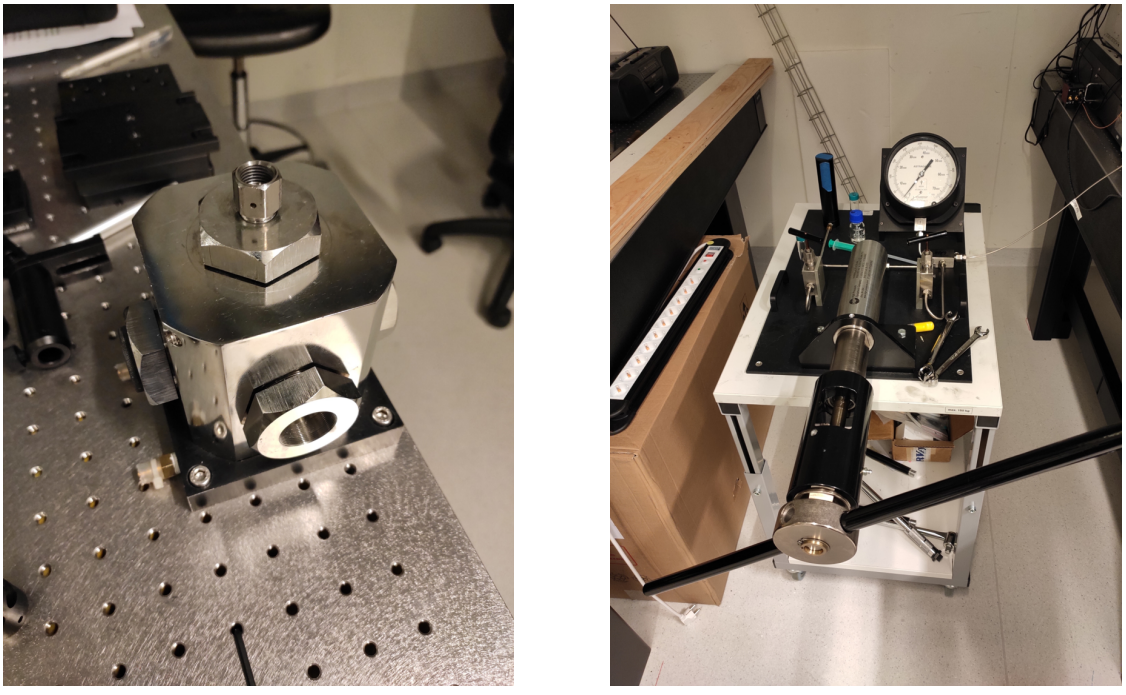

(a) (b)

Figure B.1: The pressure cell in figure (a) and the manual pump to generate pressure in figure (b)

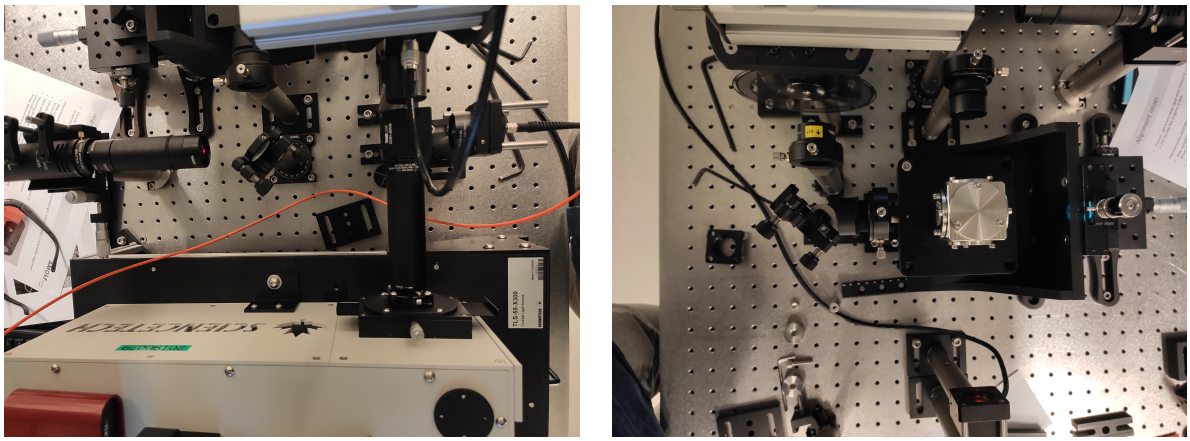

(a) (b)

Figure B.2: Close ups of the setup, showing the pump beam path on the left side in figure (a), which continues in figure (b). On the right side in figure (a), the probe laser can be seen

(a) (b)

Figure B.3: The filters were burned because of a too high pump beam intensity over a long time

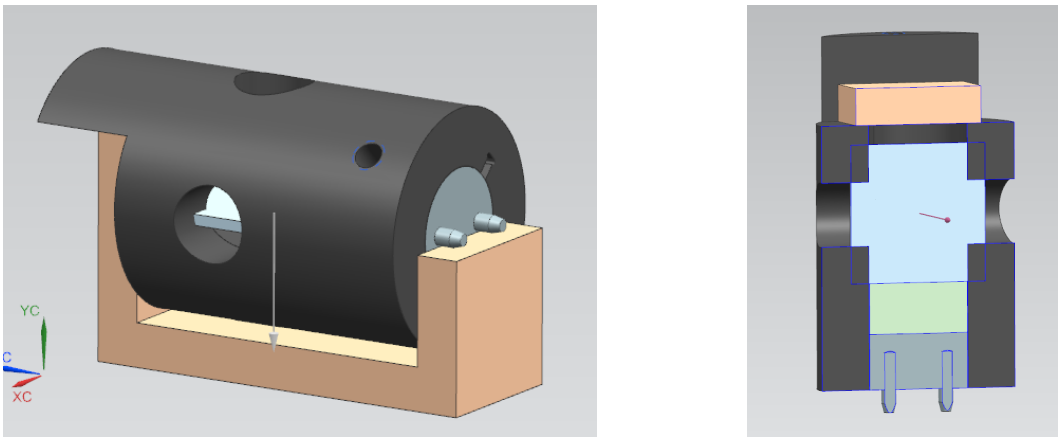

(a) (b)

Figure B.4: Sample holder in the alignment tool in figure (a). Intersection of the sample holder, with a sample inside, in figure (b)

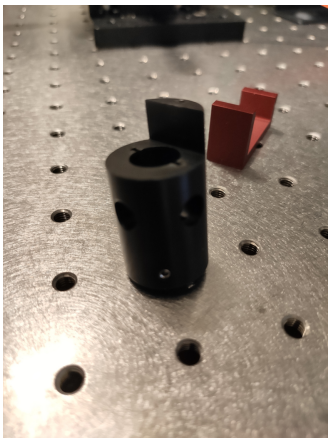

(a)

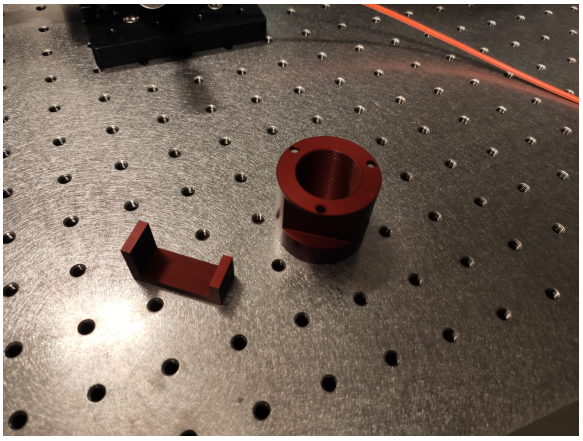

(b)

Figure B.5: Sample holder (a) and mock-up cell adapter (b). Both images also show the alignment tool for the sample holder

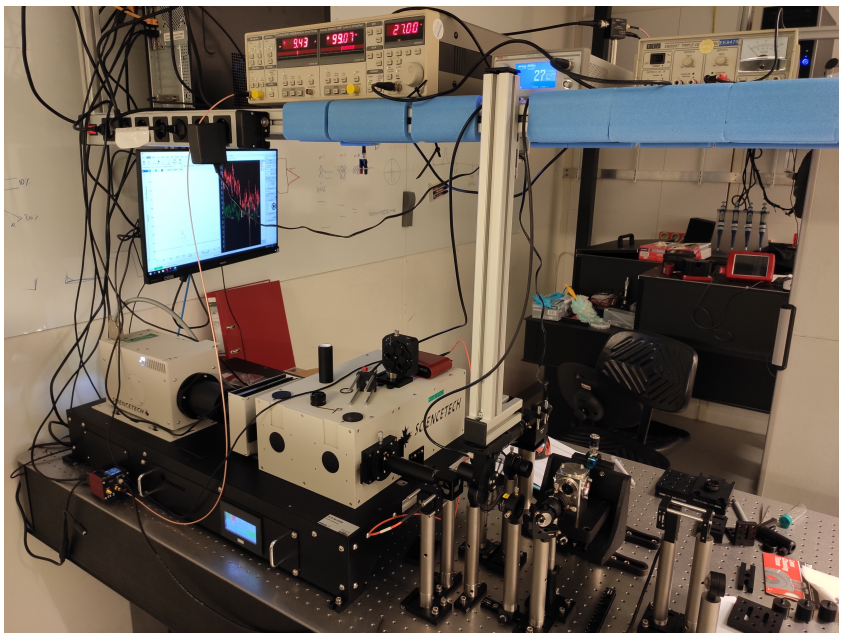

Figure B.6: Overview of the complete setup, including signal processing devices on the top shelf and the chopper wheel hanging from the top shelf. The mock-up cell is installed instead of the pressure cell.

C

Python Code

Jupyter Notebook was used for the Python code. The parameters of the probe beam were calculated as shown in the first script (section C.1), the second script shows the procedure to visualise the data measured with the PDS setup (C.2 and the third script shows the Tauc plotting and fitting of the absorption spectrum (C.3). Jupyter Notebook directly shows and plots the results, which gives a nice structured view of the different parts of the code.

C.1. Probe Beam Parameters

This script, starting on the next page, uses the properties of the liquid FC-72 and $MAPbI_3$ to calculate the thermal penetration depth and, consequently the probe beam parameters that are desired.

In [1]:

```
import pandas as pd
import numpy as np
import matplotlib.pyplot as plt
import math
```

In [2]:

```
## Parameters

l_p= 633 # wavelength of probe [nm]
f = 20 # Frequency of chopper [Hz]
f_probe = 75 # probe lens focal length [mm]
d_probe = 3 # probe beam diameter on lens [mm]

# FC72
n_f = 1.28 # refractive index FC72 [-]
k_f = 0.057 # Thermal conductivity FC72 [W/mK]
Cp_f = 1030 # Specific heat FC72 [J/kgK]
rho_f = 1.68e3 # Density FC72 [kg/m^3]
dndt_f = 4e-4 # dn/dT FC72 [K^-1]

# Silicon
n_si = 3.49 # refractive index silicon [-]
k_si = 148 # Thermal conductivity silicon [W/mK]
Cp_si = 713 # Specific heat silicon [J/kgK]
rho_si = 2.329e3 # Density silicon [kg/m^3]
dndt_si = 1.5e-4 # dn/dT silicon [K^-1]

# Perovskite (MAPbI3, tetragonal, room temp.)
n_pv = 3.49 # refractive index MAPI [-]
k_pv = 0.28 # Thermal conductivity MAPI [W/mK]
Cp_pv = 306 # Specific heat MAPI [J/kgK]
rho_pv = 4.159e3 # Density MAPI [kg/m^3]
dndt_pv = -0.93e-4 # dn/dT MAPI [K^-1]
```

In [3]:

```
# Calculate Thermal Diffusion Length (=penetration depth) of FC72
D_f =  k_f/(rho_f*Cp_f) # Thermal Diffusivity
mu_f = math.sqrt(D_f/(np.pi*f)) # thermal diffusion length
print('Thermal diffusivity of FC72 =', round(D_f*1e6, 2), 'mm\u00b2/s')
print('Thermal diffusion length in FC72 =', round(mu_f*1e6, 2), '\u03BCm')
```

```
Thermal diffusivity of FC72 = 0.03 mm²/s
Thermal diffusion length in FC72 = 22.9 µm
```

In [4]:

```
# Calculate Thermal Diffusion Length (=penetration depth) of silicon
D_si =  k_si/(rho_si*Cp_si) # Thermal Diffusivity
mu_si = math.sqrt(D_si/(np.pi*f)) # thermal diffusion length
print('Thermal diffusivity of silicon =', round(D_si*1e6, 2), 'mm\u00b2/s')
print('Thermal diffusion length in silicon =', round(mu_si*1e6, 2), '\u03BCm')
```

```
Thermal diffusivity of silicon = 89.13 mm²/s
Thermal diffusion length in silicon = 1191.0 µm
```

In [5]:

```
# Calculate Thermal Diffusion Length (=penetration depth) of MAPbI3
D_pv =  k_pv/(rho_pv*Cp_pv) # Thermal Diffusivity
mu_pv= math.sqrt(D_pv/(np.pi*f)) # thermal diffusion length
print('Thermal diffusivity of perovskite =', round(D_pv*1e6, 2), 'mm\u00b2/s')
print('Thermal diffusion length in perovskite =', round(mu_pv*1e6, 2), '\u03BCm')
```

```
Thermal diffusivity of perovskite = 0.22 mm²/s
Thermal diffusion length in perovskite = 59.17 μm
```

In [6]:

```
## Probe Beam, diameter = 3mm

# Rayleigh length/Depth of Field
DOF = (8*l_p/np.pi)*(f_probe/d_probe)**2

# Waist diameter of probe beam at focus point
w0_probe = (4*l_p/np.pi)*(f_probe/d_probe)

print('DOF =', round(DOF*1e-6, 2), 'mm')
print('w0 = ', round(w0_probe*1e-3, 2), '\u03BCm')
```

```
DOF = 1.01 mm
w0 =  20.15 μm
```

In [7]:

```
# For a fixed Rayleigh length (sample width) and probe lens
DOF_sample =10e6 # sample width of 10mm (=10e6 nm)
f_d = math.sqrt(DOF_sample*np.pi/(8*l_p)) # f/d, lens focal length divided by the beam
 diameter at lens

w0_sample = (4*l_p/np.pi)*(f_d)
d_probefixed = f_probe/f_d
print('probe waist diameter = ', round(w0_sample*1e-3, 2), '\u03BCm')
print('probe diameter before lens = ', round(d_probefixed, 2), 'mm (when lens focal len
gth is', f_probe, 'mm)')
```

```
probe waist diameter =  63.48 μm
probe diameter before lens =  0.95 mm (when lens focal length is 75 mm)
```

In [8]:

```
# For a fixed probe beam waist and lens focal length
w0_sample =  35e3 # beam waist of 35 micrometer, which is twice the penetration depth
f_d = w0_sample*np.pi/(4*l_p) # f/d, lens focal length divided by the beam diameter at
 lens
DOF = (8*l_p/np.pi)*(f_d)**2 # This will be the sample width that is necessary

d_probefixed = f_probe/f_d
print('probe DOF = ', round(DOF*1e-6, 2), 'mm')
print('probe diameter before lens = ', round(d_probefixed, 2), 'mm (when lens focal len
gth is', f_probe, 'mm)')
```

```
probe DOF =  3.04 mm
probe diameter before lens =  1.73 mm (when lens focal length is 75 mm)
```

C.2. PDS data visualisation

The Python code starting on the next page analyses the raw data that is obtained with the PDS setup. Besides the PDS data, it uses the intensity reference measurements, the UV/Vis measurement and a dataset of the responsivity of the photodetector (provided by the Thorlabs website), to correct the PDS data. The output is an absorptance spectrum of the measured sample. In this example, a measurement of $MAPbBr_3$ is used. This material is not part of this thesis project, but might be interesting for further research on the topic. It should be noted that the alignment of this specific PDS measurement was not optimised. As a result, the sensitivity does not exceed the UV/Vis spectroscopy measurement.

In [1]:

```
# Load some useful libraries
import pandas as pd
import numpy as np
import matplotlib.pyplot as plt
import seaborn as sns
import scipy
import sklearn
import statsmodels.api

# Reset all styles to the default:
plt.rcParams.update(plt.rcParamsDefault)
# Then make graphs inline:
%matplotlib inline

# Useful function for Jupyter to display text in bold:
def displaybd(text):
    display(Markdown("**" + text + "**"))

# Constants
h = 4.135667516e-15# Planck's constant [eV*s]
c = 299792458 # speed of light [m/s]

font = {'family': 'serif',
        'weight': 'normal',
        'size': 18,
        }
plt.rc('font', **font)
```

In [2]:

```
# Load the measured data
df_data = pd.read_csv("Sample Data/20200730_MAPbBr_Ambient_Loreta.csv")
df_data.columns = ['Index', 'Wavelength', 'Repeat', 'X', 'Y', 'R', 'Theta', 'Intensity'
, 'LampPower']

# Load reference intensity data (from measurement before/after, sensor located at beam
 splitter position)
df_intref_bs = pd.read_csv("Photodiode/Reference Data/20200730_MAPbBr_Ambient_Loreta.cs
v")
df_intref_bs.columns = ['Index', 'Wavelength', 'Repeat', 'X', 'Y', 'R', 'Theta', 'Inten
sity', 'LampPower']
df_intref_bs.drop(columns=['Index', 'Repeat', 'X', 'Y', 'R', 'Theta', 'LampPower'], inp
lace=True)
df_intref_bs.set_index('Wavelength', inplace=True)

# Load reference intensity data (from measurement before/after, sensor located at sampl
e position)
df_intref_sample = pd.read_csv("Photodiode/Reference Data/20200730_Inensity_reference.c
sv")
df_intref_sample.columns = ['Index', 'Wavelength', 'Repeat', 'X', 'Y', 'R', 'Theta', 'I
ntensity', 'LampPower']
df_intref_sample.drop(columns=['Index', 'Repeat', 'X', 'Y', 'R', 'Theta', 'LampPower'],
inplace=True)
df_intref_sample.set_index('Wavelength', inplace=True)

# Responsivity of photodiode
df_resp = pd.read_csv("Photodiode/FDS1010_responsivity.csv")
df_resp.columns = ['Wavelength', 'Responsivity']
df_resp.set_index('Wavelength', inplace=True)

# Load UVVIS data
df_UV = pd.read_csv("UVVIS/UVVIS_mapbbr.csv")
df_UV.columns = ['Wavelength', 'Absorbance']
```

In [3]:

```
# Take the mean of the intensity data per Wavelength
df_intref_sample.head()
df_intsample = df_intref_sample.groupby(['Wavelength'])[['Intensity']].mean()
df_intbs = df_intref_bs.groupby(['Wavelength'])[['Intensity']].mean()

df_intref = df_intbs['Intensity'].div(df_intsample['Intensity'],axis='index').to_frame(
'I_factor')
```

In [4]:

```
# Combine the intensity reference measurement and the responsivity into one correction
 factor
Int_factor = df_intref['I_factor'].mul(df_resp['Responsivity'],axis='index').to_frame(
'Intensity factor')
Int_factor.dropna(inplace=True)
```

In [5]:

```
# Look at the data at a single wavelength to determine how much time it needs to stabil
ize
test_wl = 540 # test wavelength

df_test=df_data[df_data.Wavelength == test_wl]

fig, ax1 = plt.subplots(figsize=(9,5))
ax1.set_title(r'Signal over time at $\lambda =$' + str(test_wl) + ' nm')

color = 'tab:blue'
Delay = 1 # in seconds, as chosen when measurement was started (100ms = 0.1, 1000ms =
 1)
x=df_test['Repeat']*Delay
y=df_test['R']
ax1.plot(x, y, '-', color=color)
ax1.set_xlabel('time [s]')
ax1.set_ylabel('Absolute Signal [mV]', color=color)
ax1.tick_params(axis='y', labelcolor=color)

# Take the last x% of the data when the signal is stable
x_stable = 0.7
Rep = (df_data.Repeat.iloc[-1]+1)*x_stable

ax1.axvline(x=Rep, ymin=0, ymax=1, ls='--', color='black')
ax1.annotate('stable signal \nused for analysis',
             xy=(Rep, (np.max(y)+np.min(y))/2), xycoords='data',
             xytext=(Rep*1.1, (np.max(y)+np.min(y))/2), textcoords='data',
             arrowprops=dict(arrowstyle="<-"),
             horizontalalignment='left', verticalalignment='center', size=14)

# fig.tight_layout()  # otherwise the right y-label is slightly clipped
plt.show()
```

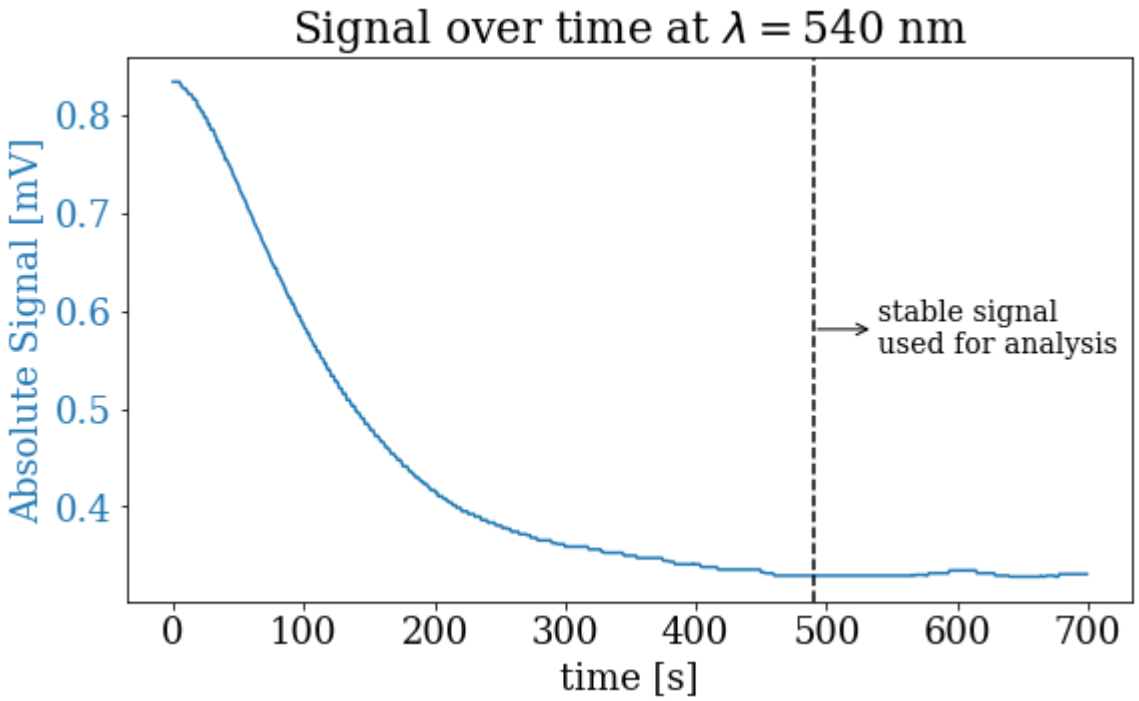

In [6]:

```
# Correct the measured intensity signal with the intensity factor
meanInt = df_data.groupby(['Wavelength'])[['Intensity']].mean()
CorrInt = meanInt['Intensity'].div(Int_factor['Intensity factor'],axis='index').to_fram
e('Corrected Intensity')
CorrInt.dropna(inplace=True)

# Throw away the data in the non-stable region
Rep = (df_data.Repeat.iloc[-1]+1)*x_stable
df=df_data[df_data.Repeat > Rep]
df.reset_index(drop=True, inplace=True)
```

In [7]:

```
# Take the mean of the data in the stable region, correct it for the intensity
meanR = df.groupby(['Wavelength'])[['R']].mean()
CorrR = meanR['R'].div(CorrInt['Corrected Intensity']).to_frame('Corrected R')
stdR = df.groupby(['Wavelength'])[['R']].std()
stdCorrR = stdR['R'].div(CorrInt['Corrected Intensity']).to_frame('stdDev Corrected R')
stdPhase = df.groupby(['Wavelength'])[['Theta']].std()

df2 = pd.concat([meanR,stdR,meanInt,CorrR,stdCorrR,stdPhase],axis=1)
df2.columns = ['R', 'std R', 'Corrected I', 'Corrected R', 'std CorrR', 'stdPhase']
df2.reset_index(inplace=True)
```

In [8]:

```
# Insert a column with eV instead of Wavelength
ev = h*c*1e9/df2['Wavelength']
df2['eV'] = ev
df2 = df2.reindex(columns=['Wavelength','eV','R', 'std R', 'Corrected I','Corrected R',
'std CorrR','stdPhase'])

df2.head() # .head shows the first 5 lines of the dataframe
```

Out[8]:

	Wavelength	eV	R	std R	Corrected I	Corrected R	std CorrR	stdPhase
0	450	2.755204	0.171890	0.002055	0.067469	0.098031	0.001172	0.643654
1	455	2.724927	0.479016	0.001060	0.179876	0.092638	0.000205	0.218014
2	460	2.695309	0.585173	0.002569	0.230628	0.089296	0.000392	0.122985
3	465	2.666327	0.719382	0.003453	0.280367	0.089924	0.000432	0.237389
4	470	2.637962	0.901734	0.000477	0.370981	0.090116	0.000048	0.076676

In [9]:

```
# Take a look at the raw measured absorption data
fig, ax1 = plt.subplots(figsize=(9,5))

color = 'tab:red'
ax1.errorbar(df2['Wavelength'], df2['R'], yerr=df2['std R'], fmt='v-', color=color, cap
size=3)
ax1.set_xlabel('Wavelength [nm]')
ax1.set_ylabel('R (Magnitude) [a.u.]', color=color)
ax1.tick_params(axis='y', labelcolor=color)
plt.yscale("log")

plt.xlim(400, 650)
# fig.tight_layout()  # otherwise the right y-label is slightly clipped
plt.show()
```

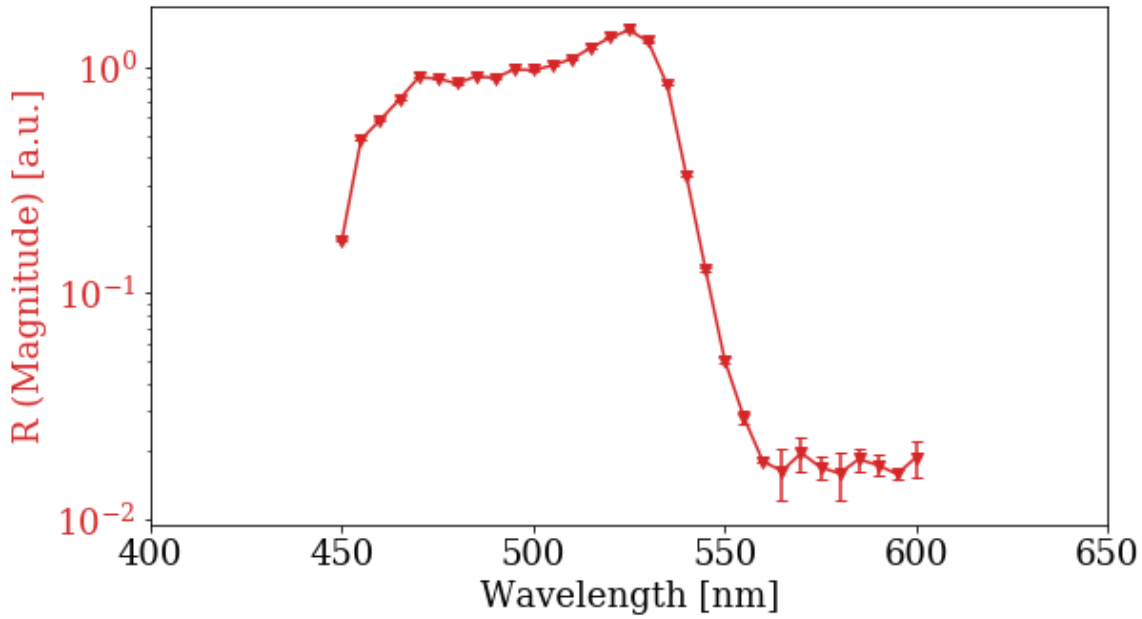

In [10]:

```
# Take a look at the unscaled absorptance and the phase deviation
fig, ax1 = plt.subplots()

color = 'tab:red'
ax1.errorbar(df2['Wavelength'], df2['Corrected R'], yerr=df2['std CorrR'], fmt='v-', co
lor=color, capsize=3)
ax1.set_xlabel('Wavelength [nm]')
ax1.set_ylabel('Absorptance [a.u.]', color=color)
ax1.tick_params(axis='y', labelcolor=color)
plt.yscale("log")

ax2 = ax1.twinx()  # instantiate a second axes that shares the same x-axis

color = 'tab:cyan'
ax2.set_ylabel('Phase stdDev', color=color)  # we already handled the x-label with ax1
ax2.tick_params(axis='y', labelcolor=color)
ax2.plot(df2['Wavelength'], df2['stdPhase'], 'o-', color=color)
# plt.ylim(-5, 85)

plt.xlim(400, 650)
# fig.tight_layout()  # otherwise the right y-label is slightly clipped
plt.show()
```

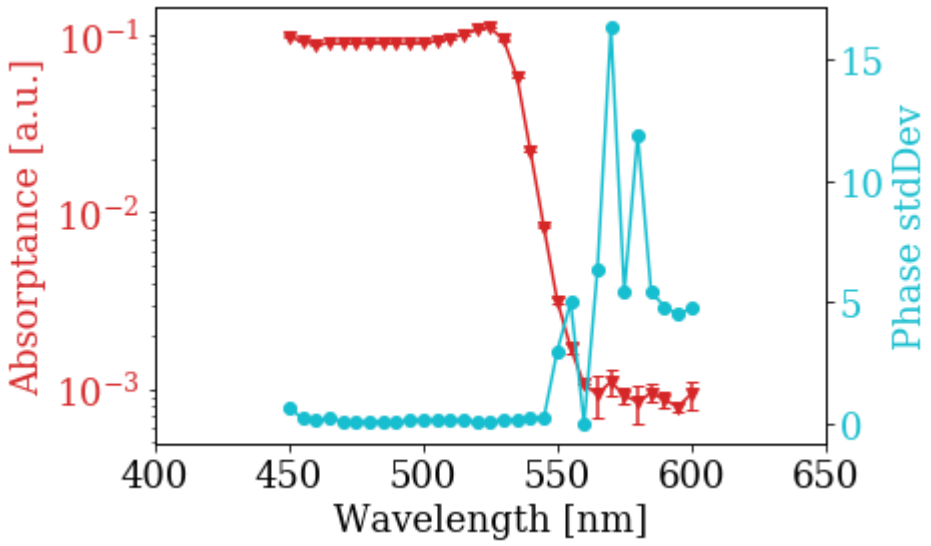

In [11]:

```
fig, ax1 = plt.subplots(figsize=(9,5))
ax1.set_title('MAPI PDS Absorptance & Pump beam intensity')

color = 'tab:red'

x=df2['Wavelength']
ax1.set_yscale("log")
ax1.plot(x, df2['Corrected R'], 'v-', color=color)
ax1.set_xlabel('Wavelength [nm]')
ax1.set_ylabel('Absorption [a.u.]', color=color)

color = 'maroon'
ax1.errorbar(df2['Wavelength'], df2['R'], yerr=df2['std R'], fmt='v-', color=color, cap
size=3)
ax1.set_xlabel('Wavelength [nm]')
ax1.set_ylabel('R(Magnitude) [a.u.]', color=color)
ax1.tick_params(axis='y', labelcolor=color)

ax2 = ax1.twinx()  # instantiate a second axes that shares the same x-axis

color = 'tab:orange'
x=df2['Wavelength']
y=df2['Corrected I']
ax2.plot(x, y, 'v-', color=color)

ax2.set_xlabel('Wavelength [nm]')
ax2.set_ylabel('Corrected Intensity signal[V]', color=color)
ax2.tick_params(axis='y', labelcolor=color)
ax2.set_yscale("log")

plt.xlim(400, 650)
# fig.tight_layout()  # otherwise the right y-label is slightly clipped
plt.show()
```

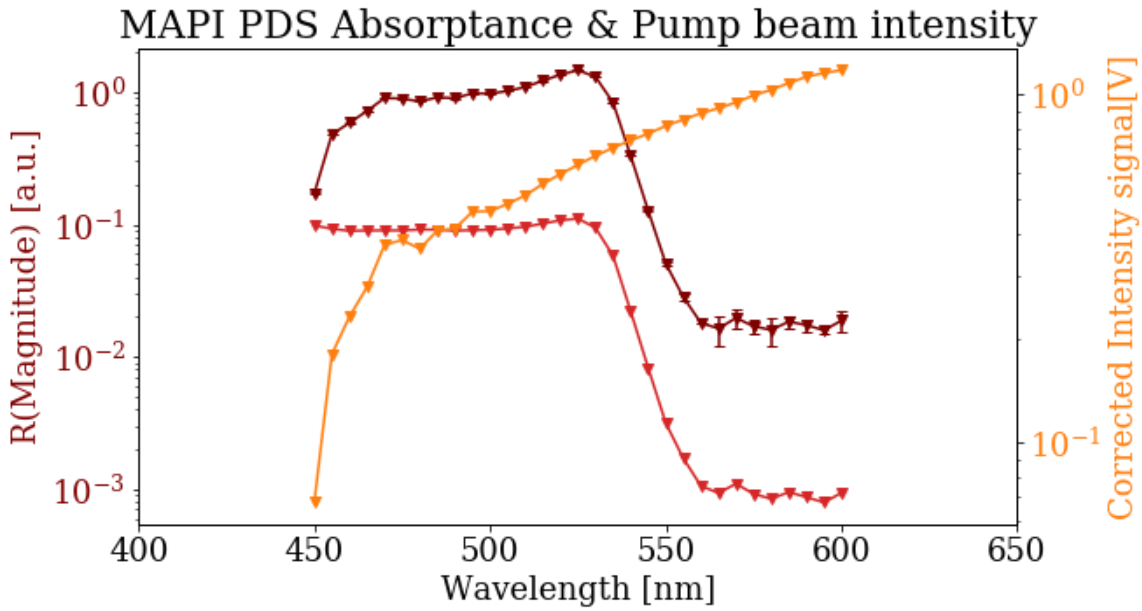

In [12]:

```
# UV/VIS data. Insert a column with eV instead of Wavelength
ev = h*c*1e9/df_UV['Wavelength']
df_UV['eV'] = ev
df_UV = df_UV.reindex(columns=['Wavelength','eV','Absorbance'])

fig, ax1 = plt.subplots(figsize=(9,5))
ax1.set_title(r'UV/VIS Absorbance and Absorptance')

color = 'tab:blue'
ax2 = ax1.twinx()  # instantiate a second axes that shares the same x-axis
ax2.plot(df_UV['Wavelength'], 1-10**(-df_UV['Absorbance']), 'o-', color=color, label='UV-VIS (Fa/Absorptance)')
ax2.set_ylabel('Absorptance [a.u.]', color=color)
ax2.tick_params(axis='y', labelcolor=color)
ax2.set_ylim(0,0.9)

ax1.plot(df_UV['Wavelength'], df_UV['Absorbance'], 'o-', color='red', label='UV-VIS (A/Absorbance)')
ax1.set_xlabel('Wavelength [nm]')
ax1.set_ylabel('Absorbance [a.u.]', color='red')
ax1.tick_params(axis='y', labelcolor='red')
ax1.set_ylim(0,0.9)

fig.legend(loc="lower left", bbox_to_anchor=(0,0), bbox_transform=ax1.transAxes, prop={'size': 13})
# plt.yscale("log")
plt.xlim(350, 650)

plt.show()
```

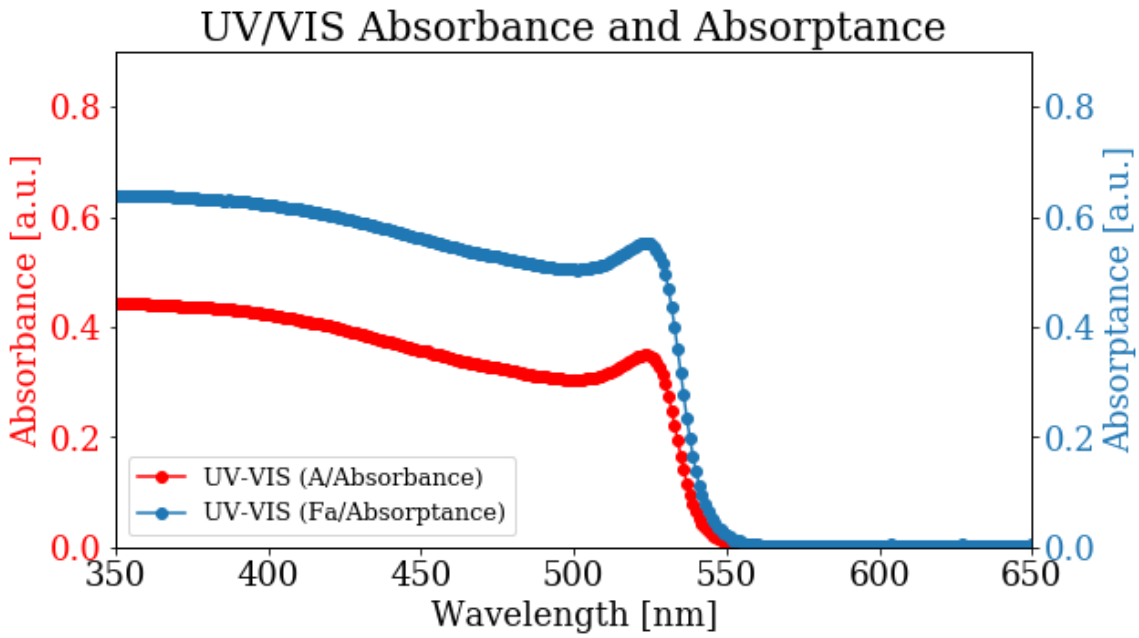

In [13]:

```
# Wavelength used for scaling (index = 1)
Wave_sc = 530 # nm

# UVVIS absorptance used for scaling
dfUV_sc = 1-10**(-df_UV.loc[df_UV['Wavelength'] == Wave_sc, 'Absorbance'].values.astype
(float))

# Scaling factor
df2_sc = df2.loc[df2['Wavelength'] == Wave_sc, 'Corrected R'].values.astype(float)/dfUV
_sc

# After scaling, absorptance of PDS is obtained
df2['absorptance']=df2['Corrected R']/df2_sc
df2['error_Fa']=df2['std CorrR']/df2_sc

df2.head()
```

Out[13]:

	Wavelength	eV	R	std R	Corrected I	Corrected R	std CorrR	stdPhase	abs
0	450	2.755204	0.171890	0.002055	0.067469	0.098031	0.001172	0.643654	
1	455	2.724927	0.479016	0.001060	0.179876	0.092638	0.000205	0.218014	
2	460	2.695309	0.585173	0.002569	0.230628	0.089296	0.000392	0.122985	
3	465	2.666327	0.719382	0.003453	0.280367	0.089924	0.000432	0.237389	
4	470	2.637962	0.901734	0.000477	0.370981	0.090116	0.000048	0.076676	

In [14]:

```
# Create dataset showing PDS effect of radiative recombination

x_nm = df2['Wavelength']
h = 4.135667516e-15# Planck's constant [eV*s]
c = 299792458 # speed of light [m/s]
x_ev = h*c*1e9/x_nm

PLQE = 0.01 # PLQE/PLQY measured
Ebg = 1.61 # PL wavelength/energy, or bandgap

PDS_Abs = df2['Corrected R']/((x_ev-Ebg*PLQE)/x_ev) # Divide PDS data with factor

df_PDS = pd.DataFrame({'Wavelength': x_nm, 'eV': x_ev, 'Absorption': PDS_Abs})

PDS_sc = df_PDS.loc[df_PDS['Wavelength'] == Wave_sc, 'Absorption'].values.astype(float)
/dfUV_sc

df_PDS.head()
```

Out[14]:

	Wavelength	eV	Absorption
0	450	2.755204	0.098608
1	455	2.724927	0.093189
2	460	2.695309	0.089832
3	465	2.666327	0.090470
4	470	2.637962	0.090669

In [15]:

```
fig, ax1 = plt.subplots(figsize=(10,6))

color = 'tab:red'

ax1.errorbar(df2['eV'], df2['Corrected R']/df2_sc, yerr=df2['std CorrR']/df2_sc, fmt='v
-', color='maroon', capsize=2, label='PDS Absorptance')

ax1.set_xlabel('Energy [eV]')
ax1.set_ylabel('Absorptance [a.u.]')
# ax1.tick_params(axis='y', labelcolor=color)
plt.yscale("log")

# ax2 = ax1.twinx()  # instantiate a second axes that shares the same x-axis

# UVVIS Plot
color = 'tab:blue'
ax1.plot(df_UV['eV'], 1-10**(-df_UV['Absorbance']), 'o', color=color, label='UV-VIS')

# PDS Plot, corrected for PLQY
color = 'tab:orange'
ax1.plot(df_PDS['eV'], df_PDS['Absorption']/PDS_sc, 'o-', color=color, label='PDS, PLQY
corrected')

ax1.legend(loc='lower right')
plt.xlim(2, 2.6)
plt.ylim(1e-3, 0.8)
# fig.tight_layout()  # otherwise the right y-label is slightly clipped
plt.show()
```

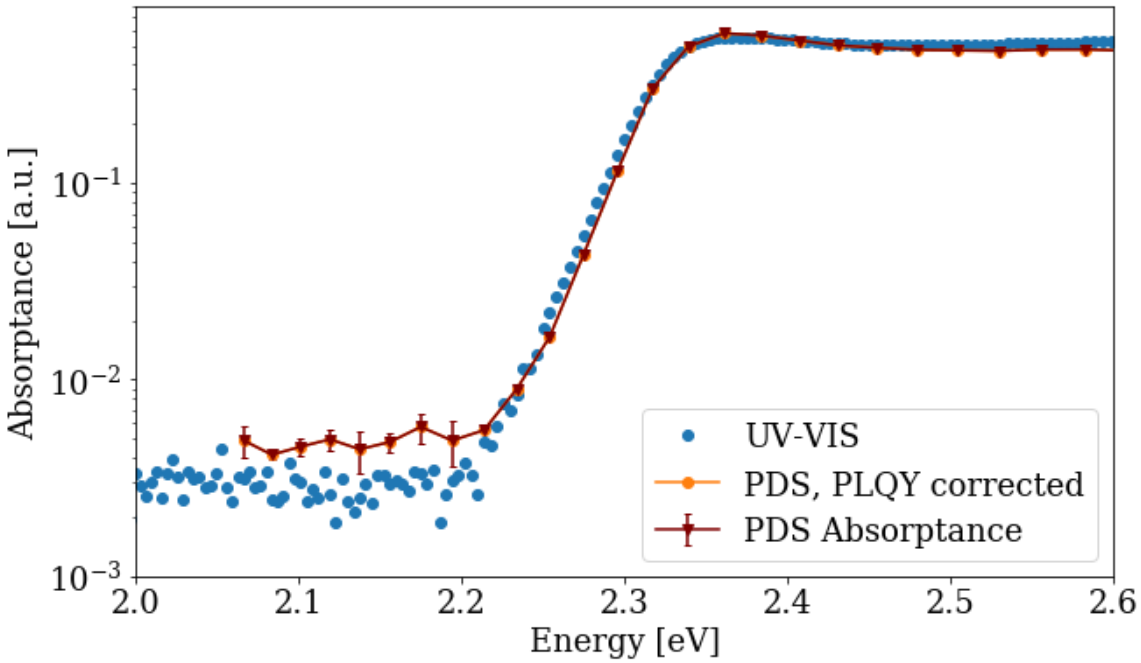

C.3. Tauc plotting and fitting

The next pages show the code that is used for fitting Tauc plots of the absorption data. The absorptance is first converted to absorbance data, to make it suitable for Tauc plots. The Statsmodels package uses ordinary least squares for the fitting of the data. This example uses the PDS data of $MAPbI_3$, measured at ambient pressure.

Tauc plots and fitting

In [153]:
```
# Convert the absorptance data to absorbance
df2['absorbance']=-np.log10(1-df2['absorptance'])
spectrum = df2[['Wavelength', 'absorbance', 'error_Fa']].to_numpy()
# print(spectrum)

spectrum2 = df2[['eV', 'absorbance', 'error_Fa']].to_numpy()
# print(spectrum2)
```

In [154]:
```
# Function returning excitation energy
def GetHv(x):
    return (h*c)/(x*1e-9)

# Function returning Tauc plot y-axis (n=1/2 for direct allowed transitions, n=2 for indirect allo
wed transitions)
def GetAlpha(hv,f,n):
    return (hv*f)**(1/n)

tauc_spec = np.zeros((len(spectrum),3))
tauc_spec[:,0] = GetHv(spectrum[:,0])
tauc_spec[:,1] = GetAlpha(GetHv(spectrum[:,0]), spectrum[:,1], 1)
tauc_spec[:,2] = GetAlpha(GetHv(spectrum[:,0]), spectrum[:,2], 1)
```

In [157]:
```
# Functions to combine models, used later in the fitting procedure
def totalfit(direct, indirect, directgap):
    direct2 = np.zeros((len(direct),2))
    indirect2 = np.zeros((len(indirect),2))

    direct2[:,0] = direct[:,0]
    indirect2[:,0] = indirect[:,0]
    direct2[:,1] = direct[:,1]**(1/2)
    indirect2[:,1] = indirect[:,1]**(2)
    indirect2 = indirect2[indirect2[:,0] <= directgap]
    direct2[direct2 < np.max(indirect2[:,1])] = np.max(indirect2[:,1])
#     direct_fit2[:,1] = np.amax(direct_fit2[:,1], indirect_fit[,1] )

    total = np.concatenate((direct2, indirect2), axis=0)

    return total

def totalfit3(direct, indirect, directgap):
    direct2 = np.zeros((len(direct),2))
    indirect2 = np.zeros((len(indirect),2))

    direct2[:,0] = direct[:,0]
    indirect2[:,0] = indirect[:,0]
    direct2[:,1] = direct[:,1]**(1/2)
    indirect2[:,1] = indirect[:,1]**(2)

    total = np.zeros((len(direct),2))
    total[:,0] = direct[:,0]
    total[:,1] = direct2[:,1] + indirect2[:,1]

    return total

def urbachmerge(total, urbachline, transition):
    urbachline2 = np.zeros((len(urbachline),2))

    urbachline2[:,0] = urbachline[:,0]
    urbachline2[:,1] = np.exp(urbachline[:,1])
    urbachline2 = urbachline2[urbachline2[:,0] <= transition]
    total = total[total[:,0] > transition]

#     total[total < np.max(urbachline2[:,1])] = np.max(urbachline2[:,1])
    # direct_fit2[:,1] = np.amax(direct_fit2[:,1], indirect_fit[,1] )

    merged = np.concatenate((total, urbachline2), axis=0)

    return merged

total_fit = totalfit(direct_fit, indirect_fit, direct_gap)
total_fit = urbachmerge(total_fit, urbach_fit, 1.53)
```

In [161]:
```
# Function to calculate the R2 of a combined fit
def R2_calc(fit_data, real_data, cut, p):

    fit_df = pd.DataFrame(index=fit_data[:,0], data={'data':fit_data[:,1]**(p)} )
    data_df = pd.DataFrame(index=real_data[:,0], data={'data':real_data[:,1]} )

    join_df= fit_df.join(data_df, lsuffix='_fit', rsuffix='_measured').dropna()

    # cut-off value (eV) untill where the R2 will be calculated, because (far) above bandgap is no
t part of the fits
    cutoff = cut
    join_df= join_df[join_df.index < cutoff]

    R2 = r2_score(join_df[['data_measured']], join_df[['data_fit']])
    return R2
```

Fitting: Linear regression at slope

In [180]:
```
def taucfit2(spectrum, log):
    # Calculate Tauc plots
    tauc_direct = np.zeros((len(spectrum),2))
    tauc_direct[:,0] = spectrum[:,0]
    tauc_direct[:,1] = spectrum[:,1]**2

    tauc_indirect = np.zeros((len(spectrum),2))
    tauc_indirect[:,0] = spectrum[:,0]
    tauc_indirect[:,1] = spectrum[:,1]**(1/2)

    tauc_urbach = np.zeros((len(spectrum),2))
    tauc_urbach[:,0] = spectrum[:,0]
    tauc_urbach[:,1] = np.log(spectrum[:,1])

    R2_final = 0
    for k in range(90):
        # determine domain that is to be fitted
        E_begin = 1.53 # Lower Bound
        E_end = 1.65 # Upper Bound
        E_direct = 1.55 + k/1000 #direct bandgap, transition point between indirect and direct fit

        ## Calculate the indirect part ##

        fit_indirect = tauc_indirect[tauc_indirect[:,0] >= E_begin]
        fit_indirect = fit_indirect[fit_indirect[:,0] <= E_direct]

        Xi = sm.add_constant(fit_indirect[:,0]) #.reshape((-1, 1))
        yi = fit_indirect[:,1]

        regr_i = sm.OLS(yi,Xi) #linear_model.LinearRegression()
        model_i = regr_i.fit() #(Xi,yi)

        new_xi = np.concatenate([np.linspace(tauc_indirect[i,0],tauc_indirect[i+1,0], num=15, endp
oint=False)
                         for i in range(len(tauc_indirect)-1)])

        pred_i = model_i.get_prediction(sm.add_constant(new_xi))
        model_i_ci = np.concatenate([new_xi[:, None], pred_i.conf_int()[:, :]], axis=1)
        yi_fit = pred_i.predicted_mean
        fit_i = np.concatenate([new_xi[:, None], yi_fit[:, None]], axis=1)

        # calculate indirect bandgap
        gap_i = -model_i.params[0]/model_i.params[1] # when y=ax+b, x(y=0)=-b/a
        ymax_i = model_i.predict([1,E_direct])

        fit_i[:,1][fit_i[:,0] > E_direct] = ymax_i

        # drop negative values, add bandgap datapoint
        if log != 1:
            fit_i = fit_i[fit_i[:,1] > 0]
            fit_i = np.append(fit_i, [[gap_i, 0]], axis=0)

        ## Repeat for the direct part ##

        fit_direct = tauc_direct[tauc_direct[:,0] >= E_direct]
        fit_direct = fit_direct[fit_direct[:,0] <= E_end]

        Xd = fit_direct[:,0].reshape((-1, 1))- E_direct
        yd = fit_direct[:,1] - ymax_i**4

        regr_d = sm.OLS(yd,Xd)
        model_d = regr_d.fit()

        new_xd = np.concatenate([np.linspace(tauc_direct[i,0],tauc_direct[i+1,0], num=15, endpoint
=False)
                         for i in range(len(tauc_direct)-1)])

        pred_d = model_d.get_prediction(new_xd - E_direct)
        model_d_ci = np.concatenate([new_xd[:, None], pred_d.conf_int()[:, :]+ ymax_i**4], axis=1)
        yd_fit = model_d.predict(new_xd - E_direct) + ymax_i**4
        fit_d = np.concatenate([new_xd[:,None], yd_fit[:,None]], axis=1)

        # calculate direct bandgap
        gap_d = E_direct

        # drop negative values, add bandgap datapoint
```

```
        if log != 1:
            fit_d = fit_d[fit_d[:,1] >= (ymax_i**4)]
            fit_d = np.append(fit_d, [[gap_d, (ymax_i**4)]], axis=0)


        ## Combine direct and indirect fit into 1 total fit ##
        fit_t = totalfit(fit_d, fit_i, gap_d)

        ## Calculate R^2 to see if the total fit improved ##
        R2_total = R2_calc(fit_t, spectrum, E_end, 1)

        # output final values when R2 score is at its highest
        if R2_total > R2_final:
            R2_final = R2_total
            fit_df = fit_d
            gap_df = gap_d
            fit_if = fit_i
            gap_if = gap_i
            ymax_if = ymax_i
            fit_tf = fit_t
            model_if = model_i
            model_df = model_d
            model_i_cif = model_i_ci
            model_d_cif = model_d_ci

    ## Urbach fit ##
    R2_final2 = 0
    for l in range(70):
        urbach_transition = 1.51+l*0.001

        # Calculate the Urbach part
        fit_urbach = tauc_urbach[tauc_urbach[:,0] >= 1.48]
        fit_urbach = fit_urbach[fit_urbach[:,0] <= urbach_transition]

        Xu = sm.add_constant(fit_urbach[:,0])
        yu = fit_urbach[:,1]

        regr_u = sm.OLS(yu,Xu)
        model_u = regr_u.fit()

        pred_u = model_u.get_prediction(sm.add_constant(tauc_urbach[:,0]))
        model_u_ci = np.vstack([tauc_urbach[:,0], pred_u.conf_int()[:, :].T])

        yu_fit = pred_u.predicted_mean
        fit_u = np.concatenate((tauc_urbach[:,0].reshape((-1, 1)), yu_fit.reshape((-1, 1))), axis=
1)

        fit_t2 = urbachmerge(fit_tf, fit_u, urbach_transition)
        R2_total2 = R2_calc(fit_t2, spectrum, E_end, 1)
        if R2_total2 > R2_final2:
            R2_final2 = R2_total2
            fit_tf2 = fit_t2
            fit_uf = fit_u
            tran_f = urbach_transition
            model_u_cif = model_u_ci
            model_uf = model_u


    return model_d_cif, model_df, fit_df, tauc_direct, gap_df, model_i_cif, model_if, fit_if, tauc
_indirect, gap_if, R2_final, ymax_if, fit_tf2, model_u_cif, fit_uf, tauc_urbach, tran_f, model_uf,
R2_final2, E_begin, E_end
```

In [181]:

```
# execute function that fits the models
direct_ci, direct_model, direct_fit, direct_spectrum, direct_gapc,\
indirect_ci, indirect_model, indirect_fit, indirect_spectrum, indirect_gapc,\
R2_tot, max_indirect, total_cfit,\
urbach_ci, urbach_fit, urbach_spectrum, urbach_transitionc, urbach_model,\
R2_combined, LB, UB = taucfit2(tauc_spec, 0)
# indirect_spectrum
```

In [183]:
```
# Plot Tauc plots with the different models (seperately direct indirect urbach)

fig = plt.figure(figsize=(24,6))
ax1 = fig.add_subplot(131)

r=2
ax1.set_title('Indirect fit')
ax1.set_xlabel(r'$ h \nu$ (eV)', fontsize=15)
ax1.set_ylabel(r'$( \alpha h \nu )^{'+ str(Fraction(1/r)) +'}$ $(cm^{-'+ str(Fraction(1/r)) +'})$'
, fontsize=15)
ax1.text(1.65,0.05, 'Indirect Gap = '+str(indirect_gapc)[:5]+' eV', fontsize=12)

ax1.plot(indirect_spectrum[:,0], indirect_spectrum[:,1],'o',
         indirect_fit[:,0], indirect_fit[:,1], '--',
         indirect_gapc, 0, 'o', linewidth=3)
ax1.fill_between( indirect_ci[:,0], indirect_ci[:,1], indirect_ci[:,2], color="#b9cfe7", edgecolor
="")
ax1.plot(indirect_spectrum[:,0], np.zeros(len(indirect_spectrum)), '-')

# ax1.set_xlim(1.4, 1.9)
ax1.set_ylim(-0.05, 1)

ax2 = fig.add_subplot(132)

r=1/2
ax2.set_title('Direct fit')
ax2.set_xlabel(r'$ h \nu$ (eV)', fontsize=15)
ax2.set_ylabel(r'$( \alpha h \nu )^{'+ str(Fraction(1/r)) +'}$ $(cm^{-'+ str(Fraction(1/r)) +'})$'
, fontsize=15)
ax2.text(1.65,0.05, 'Direct Gap = '+str(direct_gapc)[:5]+' eV', fontsize=12)

ax2.plot(direct_spectrum[:,0], direct_spectrum[:,1],'o',
         direct_fit[:,0], direct_fit[:,1], '--',
         direct_gapc, max_indirect**4, 'o',
         linewidth=3)
# ax2.plot(direct_spectrum[:,0], direct_filtered,'-')
ax2.fill_between( direct_ci[:,0], direct_ci[:,1], direct_ci[:,2], color="#b9cfe7", edgecolor="")
ax2.plot(direct_spectrum[:,0], np.zeros(len(direct_spectrum)), '-')

# ax2.set_xlim(1.4, 1.9)
ax2.set_ylim(-0.05, 1)

ax3 = fig.add_subplot(133)

r=1
ax3.set_title('Urbach fit')
ax3.set_xlabel(r'$ h \nu$ (eV)', fontsize=15)
ax3.set_ylabel(r'$( \alpha h \nu )^{'+ str(Fraction(1/r)) +'}$ $(cm^{-'+ str(Fraction(1/r)) +'})$'
, fontsize=15)
ax3.text(1.6,0.0004, 'Urbach transition = '+str(urbach_transitionc)[:5]+' eV', fontsize=12)

ax3.plot(urbach_spectrum[:,0], np.exp(urbach_spectrum[:,1]),'o',
         urbach_fit[:,0], np.exp(urbach_fit[:,1]), '--',
#          urbach_gap, 0, 'o',
         linewidth=3)
ax3.fill_between( urbach_ci[0,:], np.exp(urbach_ci[1,:]), np.exp(urbach_ci[2,:]), color="#b9cfe7",
edgecolor="")

# ax3.plot(urbach_spectrum[:,0], 10**urbach_filtered,'-')
# ax3.plot(urbach_spectrum[:,0], np.zeros(len(urbach_spectrum)), '-')

# ax3.set_xlim(1.4, 1.9)
ax3.set_ylim(2e-4, 1)
plt.yscale("log")

plt.show()
```

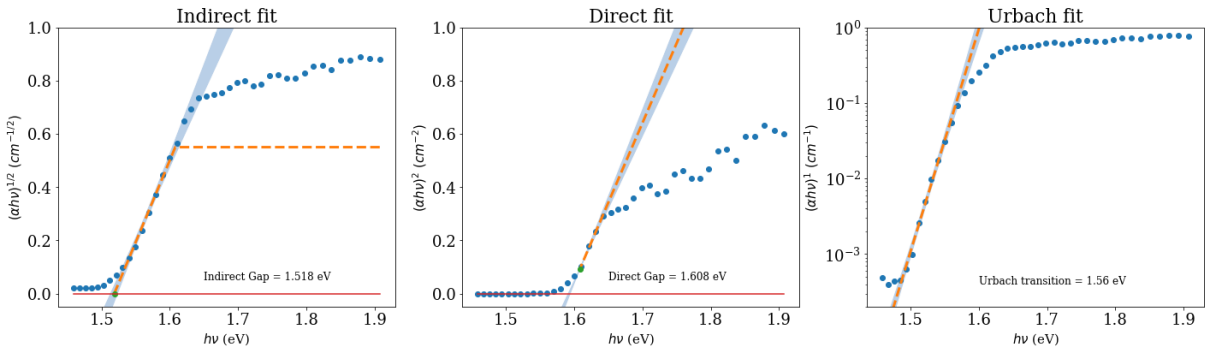
Indirect fit
Indirect Gap = 1.518 eV
$(\alpha h\nu)^{1/2}$ $(cm^{-1/2})$
$h\nu$ (eV)
Direct fit
Direct Gap = 1.608 eV
$(\alpha h\nu)^{2}$ (cm^{-2})
$h\nu$ (eV)
Urbach fit
Urbach transition = 1.56 eV
$(\alpha h\nu)^{1}$ (cm^{-1})
$h\nu$ (eV)

In [184]:
```
fig, ax1 = plt.subplots(figsize=(10,10))

r=1
ax1.set_title('Tauc plot, Pressure = ' + str(Pressure) + ' MPa')
ax1.set_xlabel(r'$ h \nu$ (eV)')
ax1.set_ylabel(r'$( \alpha h \nu )^{'+ str(Fraction(1/r)) +'}$ $(cm^{-'+ str(Fraction(1/r)) +'})$'
)
ax1.text(1.7,0.005, r'$ \Delta bandgap = '+str((direct_gapc-indirect_gapc)*1000)[:4]+'$ $meV$')

ax1.errorbar(tauc_spec[:,0], tauc_spec[:,1], yerr=tauc_spec[:,2], fmt='o', capsize=2, label='Measu
red', linewidth=2)
ax1.plot(indirect_fit[:,0], indirect_fit[:,1]**2, '--', label='Indirect Fit', color='orange', line
width=3)
# ax1.plot(indirect_spectrum[:,0], np.zeros(len(indirect_spectrum)), '-', linewidth=3)
# ax1.plot(indirect_gap, 0, 'o', label='Indirect Gap', linewidth=3)
# ax1.plot(indirect_spectrum[:,0], indirect_filtered**2,'-', label='Filtered', linewidth=3)

ax1.plot(direct_fit[:,0], direct_fit[:,1]**(1/2)-max_indirect**2,'--', label='Direct fit', color=
'green', linewidth=3)

ax1.plot(urbach_fit[:,0], np.exp(urbach_fit[:,1]), '--', label='Urbach Fit', color='purple', linew
idth=3)

ax1.plot(total_cfit[:,0], total_cfit[:,1],'-', label='Combined Fit', color='red', linewidth=4)

ax1.axvspan(LB, UB, ec ='k', fc='gainsboro', alpha = 0.5, label='Fitting range (LB-UB)')


ax1.legend(loc='lower right')
ax1.set_xlim(1.45, 1.9)

ax1.set_ylim(1e-4, 1.2)
plt.yscale("log")
plt.show()
```

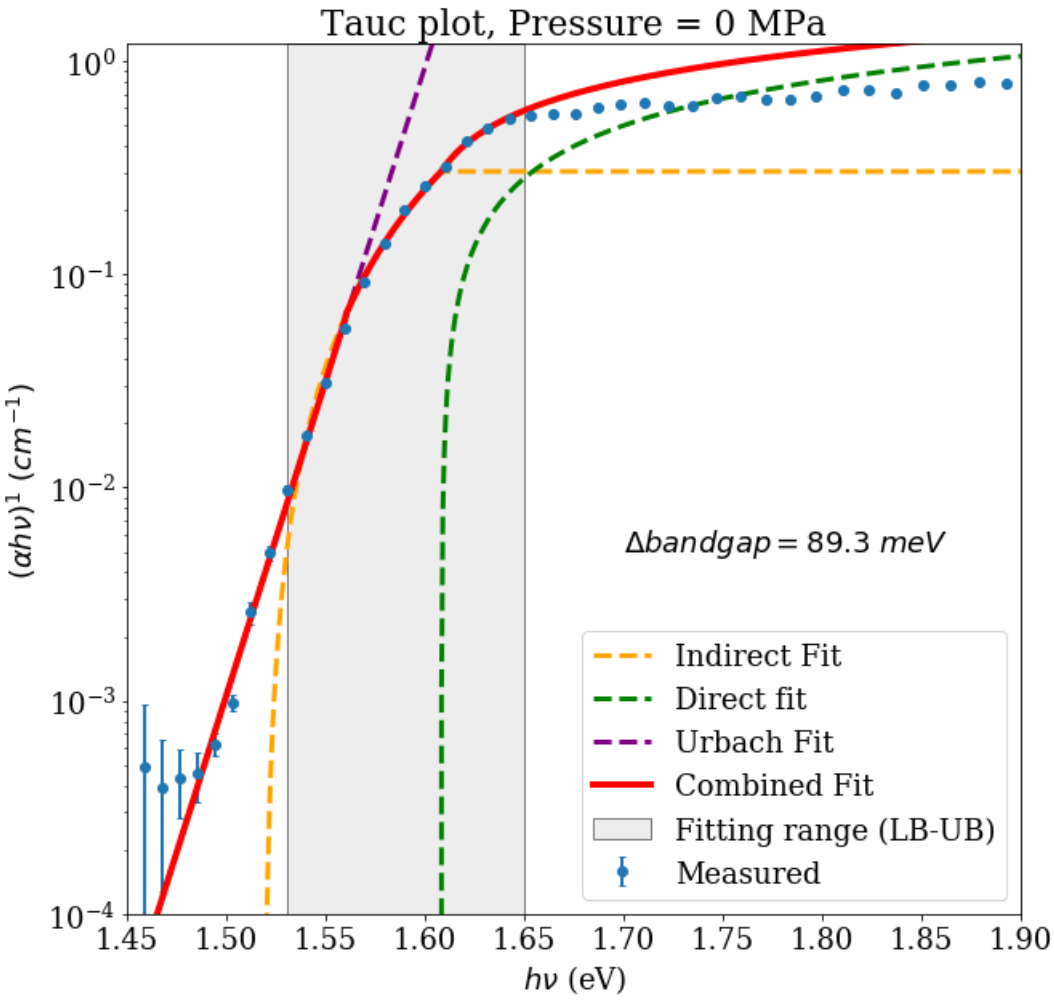

Bibliography

[1] World Energy Outlook 2019. Technical report, IEA, Paris, 2019. URL https://www.iea.org/reports/world-energy-outlook-2019.

[2] Global Status Report - Renewables 2019. Technical report, REN21, 2019.

[3] Clemens Rikken, Michiel Wijnbergh Fotografie, Dolph Cantrijn, Peter Hilz, Laurens van Putten, van de Veen, Flip Franssen, and Wim Klerkx. Klimaat en Energieverkenning 2019. page 242.

[4] Douglas Ray. Lazard's Levelized Cost of Energy Analysis—Version 13.0. page 20, 2019.

[5] Levelized Cost and Levelized Avoided Cost of New Generation Resources. Technical report, U.S. Energy Information Administration, February 2020.

[6] Ran Fu, David Feldman, and Robert Margolis. U.S. Solar Photovoltaic System Cost Benchmark: Q1 2018. *Renewable Energy*, page 63, 2018.

[7] NREL. Chart of Best Research-Cell Efficiencies Provided by NREL, 2019. URL https://www.nrel.gov/pv/assets/pdfs/best-research-cell-efficiencies.20191106.pdf.

[8] Vikram Aggarwal. The 20 Most Efficient Solar Panels of 2020, October 2019. URL https://news.energysage.com/what-are-the-most-efficient-solar-panels-on-the-market/.

[9] William Shockley and Hans J. Queisser. Detailed Balance Limit of Efficiency of *p-n* Junction Solar Cells. *Journal of Applied Physics*, 32(3):510–519, March 1961. ISSN 0021-8979, 1089-7550. doi: 10.1063/1.1736034. URL http://aip.scitation.org/doi/10.1063/1.1736034.

[10] A. De Vos. Detailed balance limit of the efficiency of tandem solar cells. *Journal of Physics D: Applied Physics*, 13(5):839–846, May 1980. doi: 10.1088/0022-3727/13/5/018. URL https://doi.org/10.1088%2F0022-3727%2F13%2F5%2F018.

[11] I. M. Peters, S. Sofia, J. Mailoa, and T. Buonassisi. Techno-economic analysis of tandem photovoltaic systems. *RSC Advances*, 6(71):66911–66923, 2016. ISSN 2046-2069. doi: 10.1039/C6RA07553C. URL http://xlink.rsc.org/?DOI=C6RA07553C.

[12] Martin A. Green, Ewan D. Dunlop, Jochen Hohl-Ebinger, Masahiro Yoshita, Nikos Kopidakis, and Anita W.Y. Ho-Baillie. Solar cell efficiency tables (Version 55). *Progress in Photovoltaics: Research and Applications*, 28(1):3–15, January 2020. ISSN 1062-7995, 1099-159X. doi: 10.1002/pip.3228. URL https://onlinelibrary.wiley.com/doi/abs/10.1002/pip.3228.

[13] Stephen Battersby. News Feature: The solar cell of the future. *Proceedings of the National Academy of Sciences*, 116(1):7–10, January 2019. ISSN 0027-8424, 1091-6490. doi: 10.1073/pnas.1820406116. URL http://www.pnas.org/lookup/doi/10.1073/pnas.1820406116.

[14] Yaoguang Rong, Yue Hu, Anyi Mei, Hairen Tan, Makhsud I. Saidaminov, Sang Il Seok, Michael D. McGehee, Edward H. Sargent, and Hongwei Han. Challenges for commercializing perovskite solar cells. *Science*, 361(6408):eaat8235, September 2018. ISSN 0036-8075, 1095-9203. doi: 10.1126/science.aat8235. URL http://www.sciencemag.org/lookup/doi/10.1126/science.aat8235.

[15] M M Ackermans. *A direct or Indirect band gap?* Literature Study, Delft University of Technology, Amsterdam, December 2020.

[16] Tianran Chen, Wei-Liang Chen, Benjamin J. Foley, Jooseop Lee, Jacob P. C. Ruff, J. Y. Peter Ko, Craig M. Brown, Leland W. Harriger, Depei Zhang, Changwon Park, Mina Yoon, Yu-Ming Chang, Joshua J. Choi, and Seung-Hun Lee. Origin of long lifetime of band-edge charge carriers in organic–inorganic lead iodide perovskites. *Proceedings of the National Academy of Sciences*, 114(29):7519–7524, July 2017. ISSN 0027-8424, 1091-6490. doi: 10.1073/pnas.1704421114. URL http://www.pnas.org/lookup/doi/10.1073/pnas.1704421114.

[17] Julian A. Steele, Pascal Puech, Bartomeu Monserrat, Bo Wu, Ruo Xi Yang, Thomas Kirchartz, Haifeng Yuan, Guillaume Fleury, David Giovanni, Eduard Fron, Masoumeh Keshavarz, Elke Debroye, Guofu Zhou, Tze Chien Sum, Aron Walsh, Johan Hofkens, and Maarten B. J. Roeffaers. Role of Electron–Phonon Coupling in the Thermal Evolution of Bulk Rashba-Like Spin-Split Lead Halide Perovskites Exhibiting Dual-Band Photoluminescence. *ACS Energy Letters*, 4(9):2205–2212, September 2019. ISSN 2380-8195, 2380-8195. doi: 10.1021/acsenergylett.9b01427. URL http://pubs.acs.org/doi/10.1021/acsenergylett.9b01427.

[18] Aurélien M. A. Leguy, Pooya Azarhoosh, M. Isabel Alonso, Mariano Campoy-Quiles, Oliver J. Weber, Jizhong Yao, Daniel Bryant, Mark T. Weller, Jenny Nelson, Aron Walsh, Mark van Schilfgaarde, and Piers R. F. Barnes. Experimental and theoretical optical properties of methylammonium lead halide perovskites. *Nanoscale*, 8(12):6317–6327, 2016. ISSN 2040-3364, 2040-3372. doi: 10.1039/C5NR05435D. URL http://xlink.rsc.org/?DOI=C5NR05435D.

[19] W. B. Jackson, N. M. Amer, A. C. Boccara, and D. Fournier. Photothermal deflection spectroscopy and detection. *Applied Optics*, 20(8):1333, April 1981. ISSN 0003-6935, 1539-4522. doi: 10.1364/AO.20.001333. URL https://www.osapublishing.org/abstract.cfm?URI=ao-20-8-1333.

[20] Bruno Burger. Photovoltaics Report. Technical report, Fraunhofer ISE, March 2019. URL https://www.ise.fraunhofer.de/content/dam/ise/de/documents/publications/studies/Photovoltaics-Report.pdf.

[21] Michele Saba, Francesco Quochi, Andrea Mura, and Giovanni Bongiovanni. Excited State Properties of Hybrid Perovskites. *Accounts of Chemical Research*, 49(1):166–173, January 2016. ISSN 0001-4842, 1520-4898. doi: 10.1021/acs.accounts.5b00445. URL https://pubs.acs.org/doi/10.1021/acs.accounts.5b00445.

[22] Stefano Razza, Sergio Castro-Hermosa, Aldo Di Carlo, and Thomas M. Brown. Research Update: Large-area deposition, coating, printing, and processing techniques for the upscaling of perovskite solar cell technology. *APL Materials*, 4(9):091508, September 2016. ISSN 2166-532X. doi: 10.1063/1.4962478. URL http://aip.scitation.org/doi/10.1063/1.4962478.

[23] Rui Wang, Muhammad Mujahid, Yu Duan, Zhao-Kui Wang, Jingjing Xue, and Yang Yang. A Review of Perovskites Solar Cell Stability. *Advanced Functional Materials*, page 1808843, February 2019. ISSN 1616301X. doi: 10.1002/adfm.201808843. URL http://doi.wiley.com/10.1002/adfm.201808843.

[24] Y. H. Chang and Chul Hong Park. First-principles study of the structural and the electronic properties of the lead-halide-based inorganic-organic perovskites (CH 3NH 3)PbX 3 and CsPbX 3 (X = Cl, Br, I). 44: 889–893, March 2004.

[25] Marina R. Filip and Feliciano Giustino. The geometric blueprint of perovskites. *Proceedings of the National Academy of Sciences*, 115(21):5397–5402, May 2018. ISSN 0027-8424, 1091-6490. doi: 10.1073/pnas.1719179115. URL http://www.pnas.org/lookup/doi/10.1073/pnas.1719179115.

[26] Moritz H Futscher. *Quantifying the efficiency and stability potential of perovskite-based devices*. PhD thesis, 2020. ISBN: 9789492323330 OCLC: 1146013122.

[27] Zhen Li, Talysa R. Klein, Dong Hoe Kim, Mengjin Yang, Joseph J. Berry, Maikel F. A. M. van Hest, and Kai Zhu. Scalable fabrication of perovskite solar cells. *Nature Reviews Materials*, 3(4):18017, April 2018. ISSN 2058-8437. doi: 10.1038/natrevmats.2018.17. URL http://www.nature.com/articles/natrevmats201817.

[28] Valerio D'Innocenzo, Giulia Grancini, Marcelo J. P. Alcocer, Ajay Ram Srimath Kandada, Samuel D. Stranks, Michael M. Lee, Guglielmo Lanzani, Henry J. Snaith, and Annamaria Petrozza. Excitons versus free charges in organo-lead tri-halide perovskites. *Nature Communications*, 5(1):3586, May 2014. ISSN 2041-1723. doi: 10.1038/ncomms4586. URL http://www.nature.com/articles/ncomms4586.

[29] Silvia Collavini, Sebastian F. Völker, and Juan Luis Delgado. Understanding the Outstanding Power Conversion Efficiency of Perovskite-Based Solar Cells. *Angewandte Chemie International Edition*, 54(34): 9757–9759, August 2015. ISSN 14337851. doi: 10.1002/anie.201505321. URL http://doi.wiley.com/10.1002/anie.201505321.

[30] P. S. Whitfield, N. Herron, W. E. Guise, K. Page, Y. Q. Cheng, I. Milas, and M. K. Crawford. Structures, Phase Transitions and Tricritical Behavior of the Hybrid Perovskite Methyl Ammonium Lead Iodide. *Scientific Reports*, 6(1):35685, December 2016. ISSN 2045-2322. doi: 10.1038/srep35685. URL http://www.nature.com/articles/srep35685.

[31] Tianyi Wang, Benjamin Daiber, Jarvist M. Frost, Sander A. Mann, Erik C. Garnett, Aron Walsh, and Bruno Ehrler. Indirect to direct bandgap transition in methylammonium lead halide perovskite. *Energy & Environmental Science*, 10(2):509–515, 2017. ISSN 1754-5692, 1754-5706. doi: 10.1039/C6EE03474H. URL http://xlink.rsc.org/?DOI=C6EE03474H.

[32] M. Songvilay, M. Bari, Z.-G. Ye, Guangyong Xu, P. M. Gehring, W. D. Ratcliff, K. Schmalzl, F. Bourdarot, B. Roessli, and C. Stock. Lifetime-shortened acoustic phonons and static order at the Brillouin zone boundary in the organic-inorganic perovskite CH 3 NH 3 PbCl 3. *Physical Review Materials*, 2(12):123601, December 2018. ISSN 2475-9953. doi: 10.1103/PhysRevMaterials.2.123601. URL https://link.aps.org/doi/10.1103/PhysRevMaterials.2.123601.

[33] A. Poglitsch and D. Weber. Dynamic disorder in methylammoniumtrihalogenoplumbates (II) observed by millimeter-wave spectroscopy. *The Journal of Chemical Physics*, 87(11):6373–6378, December 1987. ISSN 0021-9606, 1089-7690. doi: 10.1063/1.453467. URL http://aip.scitation.org/doi/10.1063/1.453467.

[34] Zhang-Ran Gao, Xiao-Fan Sun, Yu-Ying Wu, Yi-Zhang Wu, Hong-Ling Cai, and X. S. Wu. Ferroelectricity of the Orthorhombic and Tetragonal MAPbBr $_3$ Single Crystal. *The Journal of Physical Chemistry Letters*, 10(10):2522–2527, May 2019. ISSN 1948-7185. doi: 10.1021/acs.jpclett.9b00776. URL https://pubs.acs.org/doi/10.1021/acs.jpclett.9b00776.

[35] Rabi Khanal, Nicholas Ayers, Soumik Banerjee, and Samrat Choudhury. Atomic structure and electronic properties of lead and tin based hybrid halide perovskite surface for photovoltaic applications. *AIP Advances*, 9(8):085123, August 2019. ISSN 2158-3226. doi: 10.1063/1.5111569. URL http://aip.scitation.org/doi/10.1063/1.5111569.

[36] Federico Brivio, Jarvist M. Frost, Jonathan M. Skelton, Adam J. Jackson, Oliver J. Weber, Mark T. Weller, Alejandro R. Goñi, Aurélien M. A. Leguy, Piers R. F. Barnes, and Aron Walsh. Lattice dynamics and vibrational spectra of the orthorhombic, tetragonal, and cubic phases of methylammonium lead iodide. *Physical Review B*, 92(14):144308, October 2015. ISSN 1098-0121, 1550-235X. doi: 10.1103/PhysRevB.92.144308. URL https://link.aps.org/doi/10.1103/PhysRevB.92.144308.

[37] Khuong P. Ong, Shunnian Wu, Tien Hoa Nguyen, David J. Singh, Zhen Fan, Michael B. Sullivan, and Cuong Dang. Multi Band Gap Electronic Structure in CH3NH3PbI3. *Scientific Reports*, 9(1):2144, December 2019. ISSN 2045-2322. doi: 10.1038/s41598-018-38023-2. URL http://www.nature.com/articles/s41598-018-38023-2.

[38] Yue-Yu Zhang, Shiyou Chen, Peng Xu, Hongjun Xiang, Xin-Gao Gong, Aron Walsh, and Su-Huai Wei. Intrinsic Instability of the Hybrid Halide Perovskite Semiconductor CH $_3$ NH $_3$ PbI $_3$ *. *Chinese Physics Letters*, 35(3):036104, March 2018. ISSN 0256-307X, 1741-3540. doi: 10.1088/0256-307X/35/3/036104. URL https://iopscience.iop.org/article/10.1088/0256-307X/35/3/036104.

[39] Paul Allen Tipler and Ralph A. Llewellyn. *Modern physics*. W.H. Freeman, New York, NY, 5th ed edition, 2008. ISBN 978-0-7167-7550-8.

[40] Spin-orbit splitting of semiconductor band structures, 2020. URL https://docs.quantumatk.com/index.html.

[41] Peter Y. Yu and Manuel Cardona. *Fundamentals of semiconductors: physics and materials properties*. Graduate texts in physics. Springer, Berlin ; New York, 4th ed edition, 2010. ISBN 978-3-642-00709-5.

[42] M S Dresselhaus. SOLID STATE PHYSICS PART II. page 198, 2001.

[43] Marius Grundmann. *The physics of semiconductors: an introduction including devices and nanophysics*. Springer, Berlin ; New York, 2006. ISBN 978-3-540-25370-9. OCLC: ocm70201027.

[44] Deying Luo, Rui Su, Wei Zhang, Qihuang Gong, and Rui Zhu. Minimizing non-radiative recombination losses in perovskite solar cells. *Nature Reviews Materials*, 5(1):44–60, January 2020. ISSN 2058-8437. doi: 10.1038/s41578-019-0151-y. URL http://www.nature.com/articles/s41578-019-0151-y.

[45] Seth Hubbard. Recombination. In *Photovoltaic Solar Energy*, pages 39–46. John Wiley & Sons, Ltd, 2017. ISBN 978-1-118-92749-6. doi: 10.1002/9781118927496.ch5. URL https://onlinelibrary.wiley.com/doi/abs/10.1002/9781118927496.ch5. Section: 2.4 _eprint: https://onlinelibrary.wiley.com/doi/pdf/10.1002/9781118927496.ch5.

[46] G. Dresselhaus. Spin-Orbit Coupling Effects in Zinc Blende Structures. *Physical Review*, 100(2):580–586, October 1955. ISSN 0031-899X. doi: 10.1103/PhysRev.100.580. URL https://link.aps.org/doi/10.1103/PhysRev.100.580.

[47] Frank Herman, Charles D. Kuglin, Kermit F. Cuff, and Richard L. Kortum. Relativistic Corrections to the Band Structure of Tetrahedrally Bonded Semiconductors. *Physical Review Letters*, 11(12):541–545, December 1963. ISSN 0031-9007. doi: 10.1103/PhysRevLett.11.541. URL https://link.aps.org/doi/10.1103/PhysRevLett.11.541.

[48] K. V. Shanavas, Z. S. Popović, and S. Satpathy. Theoretical model for Rashba spin-orbit interaction in d electrons. *Physical Review B*, 90(16):165108, October 2014. ISSN 1098-0121, 1550-235X. doi: 10.1103/PhysRevB.90.165108. URL https://link.aps.org/doi/10.1103/PhysRevB.90.165108.

[49] E I Rashba and V I Sheka. Symmetry of Energy Bands in Crystals of Wurtzite Type II. Symmetry of Bands with Spin-Orbit Interaction Included. *Soviet physics, Solid state*, 1:368–380, 1959.

[50] Yaxin Zhai, Sangita Baniya, Chuang Zhang, Junwen Li, Paul Haney, Chuan-Xiang Sheng, Eitan Ehrenfreund, and Zeev Valy Vardeny. Giant Rashba splitting in 2D organic-inorganic halide perovskites measured by transient spectroscopies. *Science Advances*, 3(7):e1700704, July 2017. ISSN 2375-2548. doi: 10.1126/sciadv.1700704. URL http://advances.sciencemag.org/lookup/doi/10.1126/sciadv.1700704.

[51] Zhi-Gang Yu. The Rashba effect and indirect electron–hole recombination in hybrid organic–inorganic perovskites. *Physical Chemistry Chemical Physics*, 19(23):14907–14912, 2017. ISSN 1463-9076, 1463-9084. doi: 10.1039/C7CP02568H. URL http://xlink.rsc.org/?DOI=C7CP02568H.

[52] Edoardo Mosconi, Thibaud Etienne, and Filippo De Angelis. Rashba Band Splitting in Organohalide Lead Perovskites: Bulk and Surface Effects. *The Journal of Physical Chemistry Letters*, 8(10):2247–2252, May 2017. ISSN 1948-7185. doi: 10.1021/acs.jpclett.7b00328. URL https://pubs.acs.org/doi/10.1021/acs.jpclett.7b00328.

[53] Thibaud Etienne, Edoardo Mosconi, and Filippo De Angelis. Dynamical Origin of the Rashba Effect in Organohalide Lead Perovskites: A Key to Suppressed Carrier Recombination in Perovskite Solar Cells?

The Journal of Physical Chemistry Letters, 7(9):1638–1645, May 2016. ISSN 1948-7185. doi: 10.1021/acs.jpclett.6b00564. URL https://pubs.acs.org/doi/10.1021/acs.jpclett.6b00564.

[54] A C Boccara, D Fournier, Warren Jackson, and Nabil M Amer. A SENSITIVE PHOTOTHERMAL DEFLECTION TECHNIQUE FOR MEASURING ABSORPTION IN OPTICALLY THIN MEDIA. page 16.

[55] André Loges, Sabrina Herberger, Daniel Werner, and Thomas Wetzel. Thermal characterization of Li-ion cell electrodes by photothermal deflection spectroscopy. *Journal of Power Sources*, 325:104–115, September 2016. ISSN 0378-7753. doi: 10.1016/j.jpowsour.2016.05.082. URL http://www.sciencedirect.com/science/article/pii/S0378775316306358.

[56] David Becker-Koch. Exploring sub-bandgap states in organic and hybrid photovoltaic materials using photothermal deflection spectroscopy. Master's thesis, University of Heidelberg, 2016.

[57] J. Tauc. Optical properties and electronic structure of amorphous Ge and Si. *Materials Research Bulletin*, 3(1):37–46, January 1968. ISSN 00255408. doi: 10.1016/0025-5408(68)90023-8. URL https://linkinghub.elsevier.com/retrieve/pii/0025540868900238.

[58] Fan Zheng, Liang Z. Tan, Shi Liu, and Andrew M. Rappe. Rashba Spin–Orbit Coupling Enhanced Carrier Lifetime in CH $_3$ NH $_3$ PbI $_3$. *Nano Letters*, 15(12):7794–7800, December 2015. ISSN 1530-6984, 1530-6992. doi: 10.1021/acs.nanolett.5b01854. URL https://pubs.acs.org/doi/10.1021/acs.nanolett.5b01854.

[59] Eline M. Hutter, María C. Gélvez-Rueda, Anna Osherov, Vladimir Bulović, Ferdinand C. Grozema, Samuel D. Stranks, and Tom J. Savenije. Direct–indirect character of the bandgap in methylammonium lead iodide perovskite. *Nature Materials*, 16(1):115–120, January 2017. ISSN 1476-1122, 1476-4660. doi: 10.1038/nmat4765. URL http://www.nature.com/articles/nmat4765.

[60] Johannes M. Richter, Kai Chen, Aditya Sadhanala, Justinas Butkus, Jasmine P. H. Rivett, Richard H. Friend, Bartomeu Monserrat, Justin M. Hodgkiss, and Felix Deschler. Direct Bandgap Behavior in Rashba-Type Metal Halide Perovskites. *Advanced Materials*, 30(52):1803379, December 2018. ISSN 09359648. doi: 10.1002/adma.201803379. URL http://doi.wiley.com/10.1002/adma.201803379.

[61] Kevin Forsberg and Harold Mooz. The Relationship of System Engineering to the Project Cycle. *INCOSE International Symposium*, 1(1):57–65, October 1991. ISSN 23345837. doi: 10.1002/j.2334-5837.1991.tb01484.x. URL http://doi.wiley.com/10.1002/j.2334-5837.1991.tb01484.x.

[62] Kevin Forsberg and Harold Mooz. System Engineering for Faster, Cheaper, Better. page 11, 1998.

[63] Alex J Barker, Aditya Sadhanala, Felix Deschler, Marina Gandini, Phoebe M Pearce, Edoardo Mosconi, Andrew J Pearson, Yue Wu, Ram Srimath Kandada, Tomas Leitjens, Filippo De Angelis, Siân E Dutton, and Richard H Friend. Defect-Assisted Photoinduced Halide Segregation in Mixed-Halide Perovskite Thin Films. page 23.

[64] Michael C. Brennan, Anthony Ruth, Prashant V. Kamat, and Masaru Kuno. Photoinduced Anion Segregation in Mixed Halide Perovskites. *Trends in Chemistry*, 2(4):282–301, April 2020. ISSN

25895974. doi: 10.1016/j.trechm.2020.01.010. URL https://linkinghub.elsevier.com/retrieve/pii/S2589597420300356.

[65] Xiangyue Meng, Junshuai Zhou, Jie Hou, Xia Tao, Sin Hang Cheung, Shu Kong So, and Shihe Yang. Versatility of Carbon Enables All Carbon Based Perovskite Solar Cells to Achieve High Efficiency and High Stability. *Advanced Materials*, 30(21):1706975, May 2018. ISSN 09359648. doi: 10.1002/adma.201706975. URL http://doi.wiley.com/10.1002/adma.201706975.

[66] Stefaan De Wolf, Jakub Holovsky, Soo-Jin Moon, Philipp Löper, Bjoern Niesen, Martin Ledinsky, Franz-Josef Haug, Jun-Ho Yum, and Christophe Ballif. Organometallic Halide Perovskites: Sharp Optical Absorption Edge and Its Relation to Photovoltaic Performance. *The Journal of Physical Chemistry Letters*, 5(6):1035–1039, March 2014. ISSN 1948-7185. doi: 10.1021/jz500279b. URL https://pubs.acs.org/doi/10.1021/jz500279b.

[67] Lock-In Amplifier Basics, April 2020. URL https://www.thinksrs.com/downloads/pdfs/applicationnotes/Lock-In%20Basics.pdf.

[68] Photodiode Saturation and Noise Floor, . URL https://www.thorlabs.com/images/TabImages/Photodetector_Lab.pdf.

[69] Photodiodes, . URL https://www.thorlabs.com/newgrouppage9.cfm?objectgroup_id=285.

[70] Jeffrey L. Braun, Chester J. Szwejkowski, Ashutosh Giri, and Patrick E. Hopkins. On the Steady-State Temperature Rise During Laser Heating of Multilayer Thin Films in Optical Pump–Probe Techniques. *Journal of Heat Transfer*, 140(5):052801, May 2018. ISSN 0022-1481, 1528-8943. doi: 10.1115/1.4038713. URL https://asmedigitalcollection.asme.org/heattransfer/article/doi/10.1115/1.4038713/383895/On-the-SteadyState-Temperature-Rise-During-Laser.

[71] Jeffrey L. Braun and Patrick E. Hopkins. Upper limit to the thermal penetration depth during modulated heating of multilayer thin films with pulsed and continuous wave lasers: A numerical study. *Journal of Applied Physics*, 121(17):175107, May 2017. ISSN 0021-8979, 1089-7550. doi: 10.1063/1.4982915. URL http://aip.scitation.org/doi/10.1063/1.4982915.

[72] Kristien Meykens. *Study by means of photothermal deflection methods of the opto-electronic properties of CVD diamond in relation to the defect population.* PhD thesis.

[73] E. Legal Lasalle, F. Lepoutre, and J. P. Roger. Probe beam size effects in photothermal deflection experiments. *Journal of Applied Physics*, 64(1):1–5, July 1988. ISSN 0021-8979, 1089-7550. doi: 10.1063/1.341463. URL http://aip.scitation.org/doi/10.1063/1.341463.

[74] James Randall Foley. *Model-Based Estimation of the Anisotropic Thermal Properties of Materials from Photothermal Deflection Spectroscopy Data Using Bayesian Inference.* PhD thesis, Cornell University, August 2007.

[75] A.E. Siegman. *Lasers.* University Science Books, Mill Valley, California, 1986.

[76] High-Pressure Cell System, . URL http://www.iss.com/fluorescence/components/hpcell_system.html.

[77] Naoyuki Shiokawa, Yuki Mizuno, Harumasa Tsuchiya, and Eiji Tokunaga. Sagnac interferometer for photothermal deflection spectroscopy. *Optics Letters*, 37(13):2655, July 2012. ISSN 0146-9592, 1539-4794. doi: 10.1364/OL.37.002655. URL https://www.osapublishing.org/abstract.cfm?URI=ol-37-13-2655.

[78] Eline M Hutter, Loreta A Muscarella, Francesca Wittmann, Jan Versluis, Lucie McGovern, Huib J Bakker, Young-Won Woo, Young-Kwang Jung, Aron Walsh, and Bruno Ehrler. Thermodynamic Stabilization of Mixed-Halide Perovskites Against Phase Segregation. page 18.

[79] Gregg A. Swayze. Effects of spectrometer band pass, sampling, and signal-to-noise ratio on spectral identification using the Tetracorder algorithm. *Journal of Geophysical Research*, 108(E9):5105, 2003. ISSN 0148-0227. doi: 10.1029/2002JE001975. URL http://doi.wiley.com/10.1029/2002JE001975.

[80] Stuart Thomson, Maria Tesa, and Anna Gakamsky. Temperature-Dependent Absolute Photoluminescence Quantum Yield Measurements of a Halide Perovskite. page 4.

[81] Thomas Kirchartz and Uwe Rau. Decreasing Radiative Recombination Coefficients via an Indirect Band Gap in Lead Halide Perovskites. *The Journal of Physical Chemistry Letters*, 8(6):1265–1271, March 2017. ISSN 1948-7185. doi: 10.1021/acs.jpclett.7b00236. URL https://pubs.acs.org/doi/10.1021/acs.jpclett.7b00236.

[82] Akihiro Kojima, Kenjiro Teshima, Yasuo Shirai, and Tsutomu Miyasaka. Organometal Halide Perovskites as Visible-Light Sensitizers for Photovoltaic Cells. *Journal of the American Chemical Society*, 131(17):6050–6051, May 2009. ISSN 0002-7863, 1520-5126. doi: 10.1021/ja809598r. URL https://pubs.acs.org/doi/10.1021/ja809598r.

[83] Jeong-Hyeok Im, In-Hyuk Jang, Norman Pellet, Michael Grätzel, and Nam-Gyu Park. Growth of CH3NH3PbI3 cuboids with controlled size for high-efficiency perovskite solar cells. *Nature Nanotechnology*, 9(11):927–932, November 2014. ISSN 1748-3387, 1748-3395. doi: 10.1038/nnano.2014.181. URL http://www.nature.com/articles/nnano.2014.181.

[84] Yupeng Zhang, Jingying Liu, Ziyu Wang, Yunzhou Xue, Qingdong Ou, Lakshminarayana Polavarapu, Jialu Zheng, Xiang Qi, and Qiaoliang Bao. Synthesis, properties, and optical applications of low-dimensional perovskites. *Chemical Communications*, 52(94):13637–13655, 2016. ISSN 1359-7345, 1364-548X. doi: 10.1039/C6CC06425F. URL http://xlink.rsc.org/?DOI=C6CC06425F.

[85] Qingdong Ou, Xiaozhi Bao, Yinan Zhang, Huaiyu Shao, Guichuan Xing, Xiangping Li, Liyang Shao, and Qiaoliang Bao. Band structure engineering in metal halide perovskite nanostructures for optoelectronic applications. *Nano Materials Science*, 1(4):268–287, December 2019. ISSN 25899651. doi: 10.1016/j.nanoms.2019.10.004. URL https://linkinghub.elsevier.com/retrieve/pii/S2589965119300698.

[86] Valerio Sarritzu, Nicola Sestu, Daniela Marongiu, Xueqing Chang, Qingqian Wang, Sofia Masi, Silvia Colella, Aurora Rizzo, Agnieszka Gocalinska, Emanuele Pelucchi, Maria Laura Mercuri, Francesco Quochi, Michele Saba, Andrea Mura, and Giovanni Bongiovanni. Direct or Indirect Bandgap in Hybrid Lead Halide Perovskites? *Advanced Optical Materials*, 6(10):1701254, May 2018. ISSN 21951071. doi: 10.1002/adom.201701254. URL http://doi.wiley.com/10.1002/adom.201701254.

[87] Kyle Frohna, Tejas Deshpande, John Harter, Wei Peng, Bradford A. Barker, Jeffrey B. Neaton, Steven G. Louie, Osman M. Bakr, David Hsieh, and Marco Bernardi. Inversion symmetry and bulk Rashba effect in methylammonium lead iodide perovskite single crystals. *Nature Communications*, 9(1):1829, December 2018. ISSN 2041-1723. doi: 10.1038/s41467-018-04212-w. URL http://www.nature.com/articles/s41467-018-04212-w.

[88] Pooya Azarhoosh, Jarvist M. Frost, Scott McKechnie, Aron Walsh, and Mark van Schilfgaarde. Relativistic origin of slow electron-hole recombination in hybrid halide perovskite solar cells. *APL Materials*, 4(9): 091501, September 2016. ISSN 2166-532X. doi: 10.1063/1.4955028. URL http://arxiv.org/abs/1604.04500. arXiv: 1604.04500.

[89] Eline M. Hutter and Tom J. Savenije. Thermally Activated Second-Order Recombination Hints toward Indirect Recombination in Fully Inorganic CsPbI $_3$ Perovskites. *ACS Energy Letters*, 3(9):2068–2069, September 2018. ISSN 2380-8195, 2380-8195. doi: 10.1021/acsenergylett.8b01106. URL http://pubs.acs.org/doi/10.1021/acsenergylett.8b01106.

[90] Yevgeny Rakita, Omri Bar-Elli, Elena Meirzadeh, Hadar Kaslasi, Yagel Peleg, Gary Hodes, Igor Lubomirsky, Dan Oron, David Ehre, and David Cahen. Tetragonal CH $_3$ NH $_3$ PbI $_3$ is ferroelectric. *Proceedings of the National Academy of Sciences*, 114(28):E5504–E5512, July 2017. ISSN 0027-8424, 1091-6490. doi: 10.1073/pnas.1702429114. URL http://www.pnas.org/lookup/doi/10.1073/pnas.1702429114.

[91] Thomas Dittrich, Celline Awino, Pongthep Prajongtat, Bernd Rech, and Martha Ch. Lux-Steiner. Temperature Dependence of the Band Gap of CH $_3$ NH $_3$ PbI $_3$ Stabilized with PMMA: A Modulated Surface Photovoltage Study. *The Journal of Physical Chemistry C*, 119(42):23968–23972, October 2015. ISSN 1932-7447, 1932-7455. doi: 10.1021/acs.jpcc.5b07132. URL https://pubs.acs.org/doi/10.1021/acs.jpcc.5b07132.

[92] Hsiao-Wen Chen, Desman Perdamaian Gulo, Yu-Chiang Chao, and Hsiang-Lin Liu. Characterizing temperature-dependent optical properties of (MA0.13FA0.87) PbI3 single crystals using spectroscopic ellipsometry. *Scientific Reports*, 9(1):18253, December 2019. ISSN 2045-2322. doi: 10.1038/s41598-019-54636-7. URL http://www.nature.com/articles/s41598-019-54636-7.

[93] D. Yang, L. Zhang, S. Y. Yang, and B. S. Zou. Influence of the Dielectric PMMA Layer on the Detectivity of Pentacene-Based Photodetector With Field-Effect Transistor Configuration in Visible Region. *IEEE Photonics Journal*, 5(6):6801709–6801709, December 2013. ISSN 1943-0655. doi: 10.1109/JPHOT.2013.2293616. URL http://ieeexplore.ieee.org/document/6678553/.

[94] Yuanhang Cheng, Ho-Wa Li, Jian Qing, Qing-Dan Yang, Zhiqiang Guan, Chen Liu, Sin Hang Cheung, Shu Kong So, Chun-Sing Lee, and Sai-Wing Tsang. The detrimental effect of excess mobile ions in planar CH $_3$ NH $_3$ PbI $_3$ perovskite solar cells. *Journal of Materials Chemistry A*, 4(33):12748–12755, 2016. ISSN 2050-7488, 2050-7496. doi: 10.1039/C6TA05053K. URL http://xlink.rsc.org/?DOI=C6TA05053K.

[95] Jenner H. L. Ngai, Johnny K. W. Ho, Rocky K. H. Chan, S. H. Cheung, Louis M. Leung, and S. K. So. Growth, characterization, and thin film transistor application of CH $_3$ NH $_3$ PbI $_3$ perovskite on polymeric gate dielectric layers. *RSC Adv.*, 7(78):49353–49360, 2017. ISSN 2046-2069. doi: 10.1039/C7RA08699G. URL http://xlink.rsc.org/?DOI=C7RA08699G.

[96] Satyaprasad P. Senanayak, Bingyan Yang, Tudor H. Thomas, Nadja Giesbrecht, Wenchao Huang, Eliot Gann, Bhaskaran Nair, Karl Goedel, Suchi Guha, Xavier Moya, Christopher R. McNeill, Pablo Docampo, Aditya Sadhanala, Richard H. Friend, and Henning Sirringhaus. Understanding charge transport in lead iodide perovskite thin-film field-effect transistors. *Science Advances*, 3(1):e1601935, January 2017. ISSN 2375-2548. doi: 10.1126/sciadv.1601935. URL https://advances.sciencemag.org/lookup/doi/10.1126/sciadv.1601935.

[97] Martin Ledinsky, Tereza Schönfeldová, Jakub Holovský, Erkan Aydin, Zdeňka Hájková, Lucie Landová, Neda Neyková, Antonín Fejfar, and Stefaan De Wolf. Temperature Dependence of the Urbach Energy in Lead Iodide Perovskites. *The Journal of Physical Chemistry Letters*, 10(6):1368–1373, March 2019. ISSN 1948-7185. doi: 10.1021/acs.jpclett.9b00138. URL https://pubs.acs.org/doi/10.1021/acs.jpclett.9b00138.

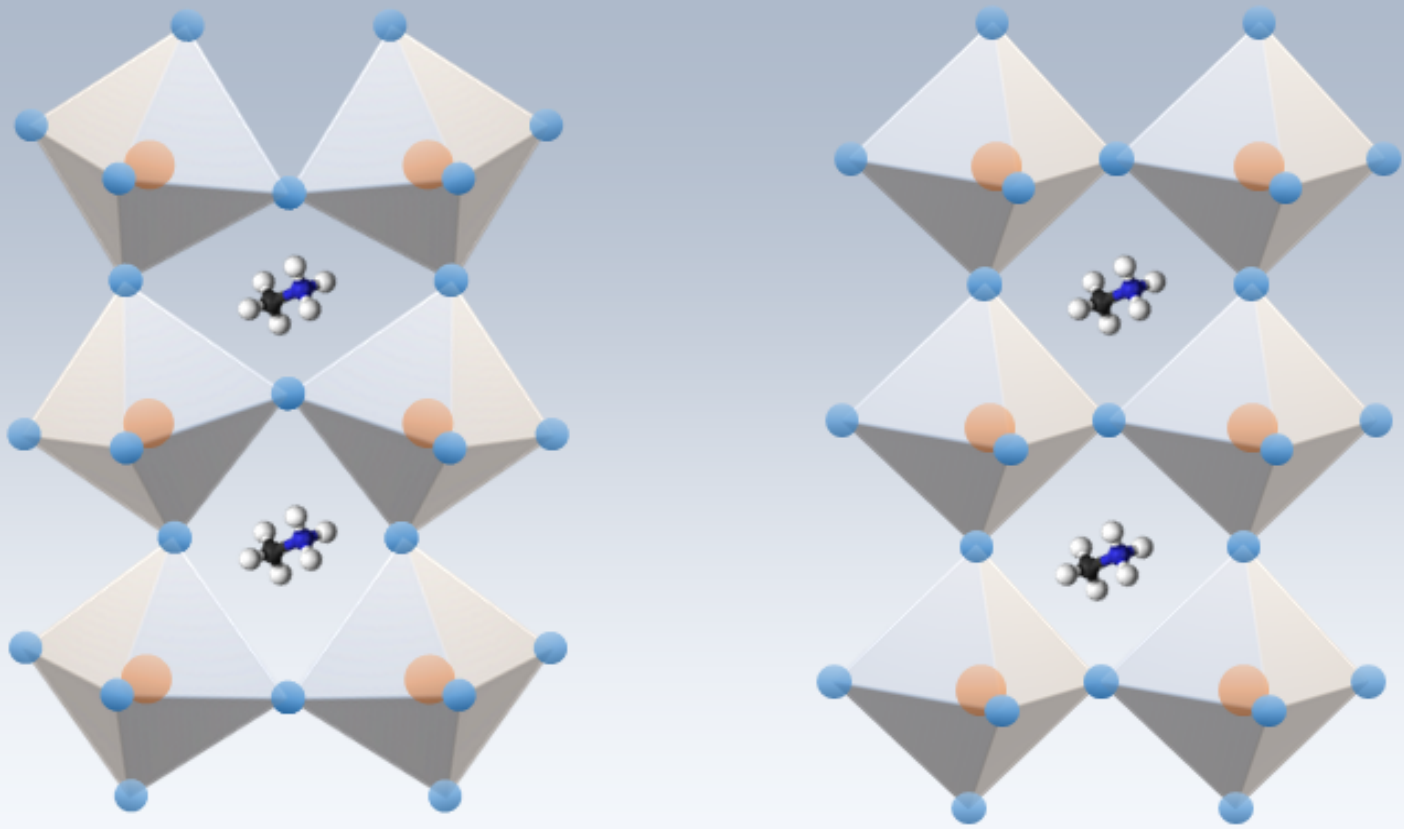

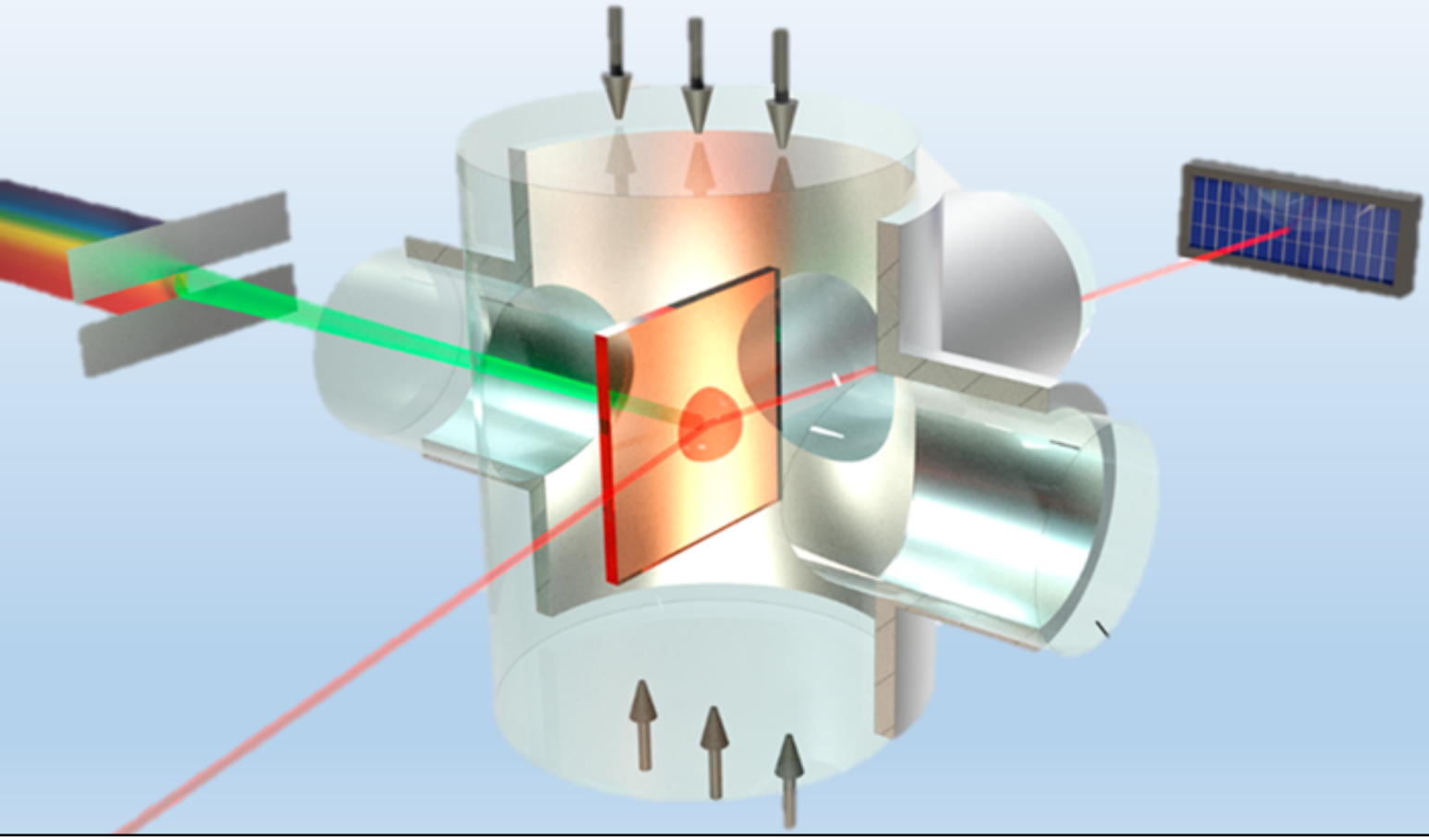

TU Delft Delft University of Technology

Challenge the future